



ELSEVIER

Physics Reports 374 (2003) 91–164

PHYSICS REPORTS

www.elsevier.com/locate/physrep

The electron-impact double ionization of atoms: an insight into the four-body Coulomb scattering dynamics

J. Berakdar^{a,*}, A. Lahmam-Bennani^b, C. Dal Cappello^c

^a*Max-Planck-Institut für Mikrostrukturphysik, Weinberg 2, D-06120 Halle, Germany*

^b*Laboratoire des Collisions Atomiques et Moléculaires (UMR 8625), Bât. 351, Université de Paris-Sud XI, F-91405 Orsay Cedex, France*

^c*Institut de Physique, Université de Metz 1 Bd Arago, Technopôle 2000, 57078 Metz, France*

Received 1 May 2002

editor: J. Eichler

Abstract

Over the past two decades impressive progress has been made in the theoretical and the experimental study of the multiple excitation and of the complete fragmentation of four-body Coulomb systems. The double ionization of atoms by charged particle impact is employed routinely to prepare and to explore the Coulomb four-body excited states (the two ionized electrons and the scattered charged projectile moving in the field of the residual ion). The spectrum of this four-body system can be determined experimentally by resolving simultaneously the momentum vectors of all particles. Such a multi-coincidence measurement entails however low counting rates which makes the experimental realization a challenging task. This work gives a brief overview on recent achievements in multi-detection techniques and outlines the various methods to carry out the double ionization experiments induced by electron impact. The advantages and the limits of the various experimental approaches are pointed out. On the theoretical side, serious difficulties are encountered which are prototypical for the theoretical treatment of many-body correlated systems: (A) With increasing number of interacting particles (and hence of degrees of freedom) a direct numerical evaluation of the four-body Green's function, which encompasses the entire spectrum of the system, becomes a challenge. (B) Due to the non-integrable character of interacting many particle systems, an analytical approach can only be approximate. In this report we discuss in details the various methods that have been put forward to deal with the four-body problem, including: perturbative many-body treatments (first and second order theories) and non-perturbative methods as well as pure numerical approaches. Due to the complicated structure of the four-particle continuum spectrum we present and discuss simple qualitative arguments to explain the main features (peaks and dips) that are observed in the experiments. The limitations of these simple methods are illustrated by contrasting the

* Corresponding author. Tel.: +49-345-5582666; fax: +49-345-5511223.
E-mail address: jber@mpi-halle.de (J. Berakdar).

predictions with full numerical calculations and with experimental data. Future directions and possible applications are also discussed.

© 2002 Elsevier Science B.V. All rights reserved.

PACS: 34.80.–i

Contents

1. Introduction	93
2. Theoretical concepts	94
2.1. Formal development	94
2.1.1. Scattering theory for multi-particle excitations	95
2.1.2. Transition probabilities and cross sections	98
2.2. Multiple scattering expansion	98
2.2.1. Double ionization pathways	100
2.3. Double ionization in the perturbative regime	104
2.3.1. Scaling properties of the cross sections	105
3. Computational schemes	106
3.1. The many-body wave function approach to double ionization	107
3.1.1. Normalization of the N -body wave functions	113
3.2. First-order perturbation treatments	114
3.2.1. The three-body Coulomb wave approach: The 3C method	114
3.2.2. The convergent close coupling approach: The CCC method	114
3.3. Beyond the perturbative regime	115
3.3.1. The second Born approximation (2BA)	115
3.3.2. The four-body Coulomb wave function: The 6C approach	116
3.3.3. Dynamical screening and effective charges: The C4FS method	116
3.3.4. The many-body Green function theory: The GF method	117
4. Experimental techniques	120
4.1. Notations	120
4.2. Overview on measured double ionization cross sections	121
4.3. Genesis of the (e,3e) experiments	122
4.4. Experimental techniques	124
4.5. General description of experimental arrangements	124
4.6. Comparison of merits and performances	127
4.7. Procedure of off-line data analysis	129
4.8. Background coincidences subtraction and percentage statistical error	129
4.9. Effective coincidence energy resolution	131
4.10. Absolute scale determination	131
5. Comparative analysis of the experimental and the numerical results: Helium	132
5.1. Fully resolved cross sections for the electron-impact double ionization	132
5.1.1. Selection rules for the (e,3e) in the perturbative regime	132
5.1.2. Numerical and experimental results	133
5.1.3. Beyond the first-Born approximation	140
6. Double ionization of many-electron atoms	142
6.1. The double ionization of noble gases	142
6.1.1. Krypton measurements	145
6.1.2. Neon measurements	146
6.1.3. Argon measurements	146

6.2. The double ionization of magnesium	148
7. Integral cross sections	149
7.1. Energy partitioning	149
7.2. Angular correlations in integral cross sections	150
7.3. Angular correlation studies on He	151
7.4. Asymmetry parameters for (e,3-1e) reactions	154
7.5. Double ionization at low energies	159
8. Conclusions and future directions	160
Acknowledgements	160
References	161

1. Introduction

In recent years significant advances have been achieved in controlling and investigating multiple, highly excited states of four-body Coulomb systems. These states are generated in most cases upon the double ionization of atoms following the impact of electrons [1–20], photons [21] or other charged-particles [22–33]. The experimental and the theoretical efforts are focused on the study of the correlated dynamics of the two ionized electrons and the scattered projectile as they propagate in the field of the residual ion. For this purpose one measures the double ionization rate while resolving simultaneously the vector momenta of all particles in the continuum. Thus, a multi-coincidence detection has to be utilized which implies low counting rates (as compared to the single particle detection) and makes an experimental realization a challenging task. This obstacle has however been tackled by several research groups in Europe and in the US by developing and employing a new generation and variation of multi-detection techniques. It is one of the aims of this review to reflect on recent technical achievements in this research area and to discuss and contrast the various available techniques.

On the theoretical side, one has to deal adequately with certain fundamental difficulties akin to many-body physics in order to provide a satisfactory description of the four-body excited spectrum: (A) Since the number of integrals of motion is less than the number of degrees of freedom an analytical solution of the N -body problem ($N > 2$) is generally not possible. On the other hand a direct numerical approach becomes increasingly challenging for larger N . (B) In contrast to condensed, many-body systems (e.g. simple metals or large metal clusters) where, due to screening, the inter-particle interaction can be treated perturbatively or can be incorporated as a renormalization of the single-particle properties, in highly excited few-body Coulomb systems ($N = 4$) the interactions are generally strong and a quasi-particle picture is not viable. A perturbative approach has as well to be carefully examined, as the convergence properties of the perturbation series for Coulomb potentials are not fully established. These facets of the theory for excited four-body systems make the treatment of particle-impact double-ionization reactions not only a challenging but also an appealing candidate to develop and test the range of validity of various few-body theories.

This report gives a detailed account of the main theoretical methods that are currently employed for the description of the Coulomb four-body continuum systems. In particular, we discuss in details first-order perturbative treatments that are used in the literature (e.g. as done in Refs. [34–43]) and present methods that operate in a non-perturbative way. Furthermore, we outline higher-order perturbation theories as well as approaches that attempt at solving the problem or parts of it full numerically [36,44–47].

In view of the aforementioned difficulties associated with the four-body problem and as well due to the large parameter space to be investigated it is useful to consider at first the general structure of the four-body spectrum and to identify qualitatively the possible mechanisms of excitations that are compatible with the energy and the momentum conservation laws. This is achieved by a multiple-scattering expansion of the four-body scattering operator. Each term of this expansion is associated with a physical scattering mechanism. For the lowest order terms a pictorial representation is given and it is pointed out where these terms may have prominent contributions. For the three-particle Coulomb scattering problem this approach has been successfully exploited [48–57], however for the present case of four particles it has not been fully utilized [58,44,59,52,45,47,35,60].

This article does not provide a comprehensive coverage of all of the theoretical and the experimental studies on double ionization of atomic targets. For a coherent and a concise presentation of the topic we focus on recent investigations that highlight the continuum four-body aspects of the particle-impact double ionization.

We begin this review by introducing the general theoretical foundations of the treatment of highly excited four-body systems and derive the formula relevant for the calculations of the particle-impact double ionization cross section. Since the majority of the experiments have been done in a situation where the incoming and the scattered projectile are fast (with respect to the Bohr velocity of the bound electrons) one may expect a perturbation treatment of the projectile–target interaction to be useful. Therefore, we devote a section to the aspects of such a treatment and show that the cross sections within this frame work satisfy certain scaling laws with respect to the charge and mass of the projectile. Therefore, within this scheme it suffices to treat the case of electron-impact double ionization. Double ionization with other projectiles is then recovered from the electron-projectile case via scaling. In a further section we review the main calculational schemes that are presently employed for the description of the fully resolved cross sections for double ionization. After an introduction of the experimental strategies and the techniques we compare the theoretical predictions with the experiments and discuss the possible scenarios for the scattering dynamics that are supported by the measurements. Furthermore, we discuss less differential cross sections and point out their potential in unravelling the scattering dynamics. The article is concluded by a brief summary and an outlook.

2. Theoretical concepts

2.1. Formal development

This section gives a brief overview on the formal theoretical foundation of the process of the double ionization upon charged-particle impact. The formulation is valid for an arbitrary mass and charge state of the projectile. In a subsequent section we specialize the treatment to the electron-impact case. As shown below, in a first-order perturbation theory with regard to the projectile-target interaction, the double ionization process by an arbitrary projectile can be mapped onto the case of the electron impact double ionization. For clarity the presentation avoids detailed discussions of the underlying mathematics, the interested reader is referred to standard quantum scattering textbooks, e.g. [61]. In particular, we do not elaborate on some of the peculiar features of scattering from Coulomb-type potentials. Unless otherwise stated, atomic units are used throughout.

2.1.1. Scattering theory for multi-particle excitations

Let us consider the particle-impact double ionization of an isolated many-electron atom that resides initially (long before the collision takes place) in the ground state $|\varphi_a\rangle$ with an energy ϵ_a . We refer to the two electrons emitted into the double continuum as the active electrons.

Upon an external perturbation by a mono-energetic charged particle beam (incident with momentum \mathbf{k}_0 relative to the center of mass of the target) the two active electrons are elevated into the double continuum and recede from the ionic core with momenta \mathbf{k}_1 and \mathbf{k}_2 . The projectile emerges in the final state with a momentum \mathbf{k}_p . The residual ion is left in the state $|\varphi_c\rangle$ (with a binding energy ϵ_c). Experimentally, it has been possible to monitor the double ionization process for well-defined values of all quantities ϵ_a , \mathbf{k}_0 and ϵ_c , \mathbf{k}_p , \mathbf{k}_1 and \mathbf{k}_2 . The momentum and the energy conservation laws impose the constraints

$$\mathbf{k}_0 = \mathbf{k}_p + \mathbf{k}_1 + \mathbf{k}_2 + \mathbf{k}_{\text{ion}} , \tag{2.1}$$

$$E_i = E_0 + \epsilon_a = E_p + E_1 + E_2 + E_{\text{ion}} + \epsilon_c = E_f . \tag{2.2}$$

Here \mathbf{k}_{ion} refers to the momentum of the ion and the ion kinetic (translational) energy is denoted by E_{ion} . The total initial and final state energies of the (projectile-target) system are respectively, E_i and E_f . The projectile energy in the initial (final) channel is E_0 (E_p). The kinetic energies of the two emitted electrons are labeled by E_1 and E_2 .

The Hamilton operators in the *asymptotic* initial and the final channels, i.e. long before and long after the collision,¹ are, respectively, given by

$$H_i = h_a + h_p \tag{2.3}$$

$$H_f = h_c + h_{\text{ex}} . \tag{2.4}$$

The operators h_a and h_c are the Hamiltonians of the undisturbed atom in the initial state and that of the residual ion, i.e.

$$h_a|\varphi_a\rangle = \epsilon_a|\varphi_a\rangle , \tag{2.5}$$

$$h_c|\varphi_c\rangle = \epsilon_c|\varphi_c\rangle . \tag{2.6}$$

The motion of the impinging projectile is dictated by the Hamiltonian h_p , while h_{ex} is the Hamiltonian of the final-state continuum fragments in the asymptotic region where all scattered particles are well separated.

Since we assumed that non-interacting asymptotic states are uniquely determined, the final (V_f) and initial-state (V_i) transition potential operators are then given by

$$V_f = H - H_f = V_{pe_1} + V_{pe_2} + V_{e_1e_2} + V_{e_1c} + V_{e_2c} + V_{pc} , \tag{2.7}$$

$$V_i = H - H_i = V_{pe_1} + V_{pe_2} + V_{pc} , \tag{2.8}$$

where the total Hamiltonian of the system is denoted by H and $V_{pe_{1/2}}$ is the two-particle Coulomb interactions between the projectile and the *active* electrons, V_{pc} is the interaction potential between the

¹ We assume that all scattering potentials vanish for infinitely large separations of the involved particles.

projectile and the final-state ionic core, and $V_{e_1/2c}$ is the scattering potential of the ionized electrons from the ionic core. Moreover, $V_{e_1e_2}$ is the Coulomb interaction between the active electrons.

The Hamiltonians H_i and H_f describe the same projectile–atom system, however with different boundary conditions (a neutral ground state atom and an undistorted projectile in case of H_i and three charged continuum particles in the field of a doubly charged ion in case of H_f). Therefore the relation applies

$$h_a = h_c + V_{e_1c} + V_{e_2c} + V_{e_1e_2} . \quad (2.9)$$

Long before (after) the ionization event, the projectile–target system is described by the state-vector $|\mathbf{k}_0, \varphi_a\rangle$ ($|\mathbf{k}_p, \mathbf{k}_1, \mathbf{k}_2, \varphi_c\rangle$), where $H_i|\mathbf{k}_0, \varphi_a\rangle = E_i|\mathbf{k}_0, \varphi_a\rangle$ and $H_f|\mathbf{k}_p, \mathbf{k}_1, \mathbf{k}_2, \varphi_c\rangle = E_f|\mathbf{k}_p, \mathbf{k}_1, \mathbf{k}_2, \varphi_c\rangle$. The probability amplitude for the transition of the system from the state $|\mathbf{k}_0, \varphi_a\rangle$ into the state $|\mathbf{k}_p, \mathbf{k}_1, \mathbf{k}_2, \varphi_c\rangle$ is given by the scattering matrix element $S_{fi}(\mathbf{k}_p, \mathbf{k}_1, \mathbf{k}_2, \varphi_c; \mathbf{k}_0, \varphi_a)$ where

$$S_{fi}(\mathbf{k}_p, \mathbf{k}_1, \mathbf{k}_2, \varphi_c; \mathbf{k}_0, \varphi_a) = \langle \mathbf{k}_0, \varphi_a | S | \mathbf{k}_p, \mathbf{k}_1, \mathbf{k}_2, \varphi_c \rangle = \langle \Psi^- | \Psi^+ \rangle . \quad (2.10)$$

The experimentally relevant (on-shell) part of these S matrix elements satisfies the constraints (2.1) and (2.2). The state vectors $|\Psi^\pm\rangle$ of the interacting projectile–target system are mapped onto the asymptotic (detector) states by means of the Møller wave operators Ω_f^-, Ω_i^+ , i.e.

$$|\Psi^-\rangle = \Omega_f^- |\mathbf{k}_p, \mathbf{k}_1, \mathbf{k}_2, \varphi_c\rangle , \quad (2.11)$$

$$|\Psi^+\rangle = \Omega_i^+ |\mathbf{k}_0, \varphi_a\rangle , \quad (2.12)$$

where

$$\Omega_f^- = \mathbf{1} + G^- V_f , \quad (2.13)$$

$$\Omega_i^+ = \mathbf{1} + G^+ V_i . \quad (2.14)$$

The fully correlated many-body Green operator G^\pm is the resolvent of H with appropriate boundary conditions. From Eqs. (2.7) and (2.8) we deduce the integral equations

$$G^- = G_f^- + G_f^- V_f G^- \quad (2.15)$$

$$G^+ = G_i^+ + G_i^+ V_i G^+ , \quad (2.16)$$

where G_f^- and G_i^+ are the resolvents of H_f and H_i (Eqs. (2.4) and (2.3)), with appropriate boundary conditions. In general the Green operators satisfy the relations $(G_f^\pm)^\dagger = G_f^\mp$ and similarly $(G_i^\pm)^\dagger = G_i^\mp$.

According to our definition the Hamiltonians h_a and h_p in Eq. (2.3) as well as h_c and h_{ex} in Eq. (2.4) are decoupled. Therefore, the relations apply

$$G_f^- = g_c^- g_{ex}^- =: G_c^- , \quad (2.17)$$

$$G_i^+ = g_a^+ g_p^+ =: G_a^+ . \quad (2.18)$$

The Green operators of the atom and the residual ionic core are denoted by g_a^+ and g_c^- , respectively. g_p^+ and g_{ex}^- are the resolvents of h_p and h_{ex} .

Furthermore, a relation between g_a^+ and g_c^+ can be established by means of Eq. (2.9)

$$g_a^+ = g_c^+ + g_c^+(V_{e_1c} + V_{e_2c} + V_{e_1e_2})g_a^+ . \quad (2.19)$$

From Eqs. (2.10)–(2.12) we can write $S_{fi} = \langle \mathbf{k}_p, \mathbf{k}_{e_1}, \mathbf{k}_{e_2}, \varphi_c | \Omega_f^{-\dagger} \Omega_i^+ | \mathbf{k}_0, \varphi_a \rangle$. Therefore, the complete dynamics is described by the product of the two wave operators. This product is traditionally called the scattering ‘S’ operator.

The conventional expression for the S matrix elements is recovered by considering the identity

$$\begin{aligned} & [\langle \Psi^+(E_i) | \Psi^-(E_f) \rangle - \langle \Psi^+(E_i) | \Psi^+(E_f) \rangle]^* \\ &= [\langle \Psi^+(E_i) | (\Omega_f^- - \Omega_f^+) | \mathbf{k}_p, \mathbf{k}_1, \mathbf{k}_2, \varphi_c \rangle]^* \end{aligned} \quad (2.20)$$

$$= \{ \langle \Psi^+(E_i) | [G^-(E_f) - G^+(E_f)] V_f | \mathbf{k}_p, \mathbf{k}_1, \mathbf{k}_2, \varphi_c \rangle \}^* . \quad (2.21)$$

From this equation it follows that the S matrix elements can be written as

$$S_{fi} = \delta_{f,i} + \langle \mathbf{k}_p, \mathbf{k}_1, \mathbf{k}_2, \varphi_c | V_f [G^+(E_f) - G^-(E_f)] | \Psi^+(E_i) \rangle \quad (2.22)$$

$$= \delta_{f,i} - i2\pi\delta(E_f - E_i) \langle \mathbf{k}_p, \mathbf{k}_1, \mathbf{k}_2, \varphi_c | V_f | \Psi^+ \rangle . \quad (2.23)$$

Here we introduced $\delta_{f,i} := \langle \Psi^+(E_i) | \Psi^+(E_f) \rangle$, where i and f stand for a set of collective quantum numbers that characterize the states $\langle \Psi^+ |$. Eq. (2.23) is readily deduced upon noting that

$$\begin{aligned} [G^+(E_f) - G^-(E_f)] | \Psi^+(E_i) \rangle &= \left[\frac{1}{E_f - E_i + i\eta} - \frac{1}{E_f - E_i - i\eta} \right] | \Psi^+(E_i) \rangle \\ &= \frac{-2i\eta}{(E_f - E_i)^2 + \eta^2} | \Psi^+(E_i) \rangle \end{aligned} \quad (2.24)$$

$$= -i2\pi\delta(E_f - E_i) | \Psi^+(E_i) \rangle . \quad (2.25)$$

In this relation η is a small positive real number. Eq. (2.25) follows from the representation of the Dirac function as $\delta(x) = \lim_{\eta \rightarrow 0^+} \eta / (x^2 + \eta^2)$.

Upon performing similar steps one derives the equivalent expression

$$S_{fi} = \delta_{f,i} - i2\pi\delta(E_f - E_i) \langle \Psi^- | V_i | \mathbf{k}_0, \varphi_a \rangle . \quad (2.26)$$

From Eqs. (2.25) and (2.26) it is clear that the dynamics of the scattered flux is governed by the (*transition*) matrix elements

$$T_{fi} := \langle \Psi^- | V_i | \mathbf{k}_0, \varphi_a \rangle = \langle \mathbf{k}_p, \mathbf{k}_1, \mathbf{k}_2, \varphi_c | (\Omega_f^-)^\dagger V_i | \mathbf{k}_0, \varphi_a \rangle , \quad (2.27)$$

$$= \langle \mathbf{k}_p, \mathbf{k}_1, \mathbf{k}_2, \varphi_c | V_f \Omega_i^+ | \mathbf{k}_0, \varphi_a \rangle =: T_{if} . \quad (2.28)$$

This equation can be expressed in terms of the Green’s function by employing the relation (2.14) for Ω_i^+ which yields

$$T_{if} = \langle \mathbf{k}_p, \mathbf{k}_1, \mathbf{k}_2, \varphi_c | V_f | \mathbf{k}_0, \varphi_a \rangle + \langle \mathbf{k}_p, \mathbf{k}_1, \mathbf{k}_2, \varphi_c | V_f G^+ V_i | \mathbf{k}_0, \varphi_a \rangle . \quad (2.29)$$

Similar relation is deduced from Eq. (2.27). Since in general the relation $G^\pm V = G_0^\pm T^\pm$ applies, Eq. (2.29) defines a Lippmann–Schwinger equation for the transition matrix elements.

2.1.2. Transition probabilities and cross sections

The S matrix elements S_{fi} are a measure for the transition probability amplitude. Thus, the probability P_{fi} for the double ionization event is then $|S_{fi}|^2$. Now if we go over into the time domain by utilizing the relation $2\pi\delta(E_f - E_i) = \int dt \exp[i(E_f - E_i)t]$ and evaluating $P_{fi} = S_{fi}S_{fi}^*$, we arrive after some elementary manipulations at the transition rate, i.e. transition probability per unit time:

$$\frac{dP_{fi}}{dt} = 2\delta_{fi} \operatorname{Im} T_{fi} + 2\pi\delta(E_f - E_i)|T_{fi}|^2, \quad (2.30)$$

$$= 2\pi\delta(E_f - E_i)|T_{fi}|^2. \quad (2.31)$$

Relation (2.31) is valid for inelastic processes, i.e. for our case, where $\delta_{fi} = 0$.

Usually what is measured and calculated in a scattering process is the transition rate from a well-prepared initial state to an infinitesimal group of final states that is characterized by a certain density of states. In our case this density of state in momentum space is given by $d^3\mathbf{k}_1 d^3\mathbf{k}_2 d^3\mathbf{k}_p$. It is furthermore customary to normalize this transition rate to the asymptotic probability flux density j_p of the incoming projectile and to call it the multiple differential cross section $\sigma(\mathbf{k}_p, \mathbf{k}_1, \mathbf{k}_2; \mathbf{k}_0, \varphi_a)$. In a mathematical language this means

$$\sigma(\mathbf{k}_p, \mathbf{k}_1, \mathbf{k}_2; \mathbf{k}_0, \varphi_a) := \frac{dP_{fi}}{dt} \frac{1}{j_p} d^3\mathbf{k}_1 d^3\mathbf{k}_2 d^3\mathbf{k}_p \quad (2.32)$$

$$= (2\pi)^4 \frac{1}{v_0} |T_{fi}|^2 \delta(E_f - E_i) d^3\mathbf{k}_1 d^3\mathbf{k}_2 d^3\mathbf{k}_p. \quad (2.33)$$

Here v_0 labels the velocity of the incoming projectile relative to the center of mass of the target. In Eq. (2.33) we assumed that the measurement resolves the vector momenta of the two electrons and the scattered projectile. As clear from Eq. (2.1), one can equally detect instead of one of the ejected electrons the momentum of the recoiling ion, as done in the so-called COLTRIMS techniques (cold target recoil ion momentum spectroscopy) [18–20,23–27,33]. Alternatively one can represent the vector momenta \mathbf{k}_j , $j=1, 2, p$ in Eq. (2.25) in spherical coordinates, i.e. by the magnitude k_j , the polar angle θ_j , and an azimuthal angle φ_j with respect to some chosen axis. Assuming a parabolic dispersion for the continuum particles one can relate the wave vectors k_j to the energies E_j and write Eq. (2.25) in the form

$$\sigma(E_1, E_2, \Omega_1, \Omega_2, \Omega_p) = (2\pi)^4 \mu_{pt}^2 \frac{k_1 k_2 k_p}{k_0} |T_{fi}|^2 dE_1 dE_2 d^2\Omega_1 d^2\Omega_2 d^2\Omega_p. \quad (2.34)$$

In deriving this relation we neglected terms of the order of the inverse mass of the nucleus and introduced the projectile–target reduced mass as $(\mu_{pt} = m_p m_t)/(m_p + m_t)$. The solid angles Ω_j are spanned by the polar and azimuthal angles θ_j and φ_j , $j = 1, 2, p$.

2.2. Multiple scattering expansion

As shown above [cf. Eqs. (2.10)–(2.12)] the prime quantity that encapsulates the collision dynamics is the scattering operator which can be written in the form

$$\begin{aligned} \Omega_f^{-\dagger} \Omega_i^+ &= (\mathbf{1} + V_f G^{-\dagger})(\mathbf{1} + G^+ V_i) \\ &= \mathbf{1} + G^+ V_i + V_f G^{-\dagger} + V_f G_f^{-\dagger} G^+ V_i. \end{aligned} \quad (2.35)$$

To disentangle the various double-ionization pathways it is useful to express Eq. (2.35) as a multiple scattering series. This expansion is derived by iterating the integral Lippmann-Schwinger equations of the Green operators (2.15) and (2.16). For clarity we consider here the lowest order terms only and write Eq. (2.35) in the form

$$\Omega_f^{-\dagger} \Omega_i^+ = \mathbf{1} + A + B + C . \quad (2.36)$$

Here A , B and C denote the leading order terms in a multiple scattering series expansion

$$\begin{aligned} A = & G_a^+ V_{pe_1} + G_a^+ V_{pe_2} + G_a^+ V_{pc} + G_a^+ V_{pe_1} G_a^+ V_{pe_2} + G_a^+ V_{pe_1} G_a^+ V_{pc} \\ & + G_a^+ V_{pe_2} G_a^+ V_{pe_1} + G_a^+ V_{pe_2} G_a^+ V_{pc} + G_a^+ V_{pc} G_a^+ V_{pe_1} + G_a^+ V_{pc} G_a^+ V_{pe_2} \\ & + G_a^+ V_{pe_2} G_a^+ V_{pe_1} G_a^+ V_{pc} + G_a^+ V_{pe_2} G_a^+ V_{pc} G_a^+ V_{pe_1} \\ & + G_a^+ V_{pc} G_a^+ V_{pe_1} G_a^+ V_{pe_2} + G_a^+ V_{pc} G_a^+ V_{pe_2} G_a^+ V_{pe_1} + \dots , \end{aligned} \quad (2.37)$$

$$B = \sum_{j=1}^7 B_j , \quad (2.38)$$

$$\begin{aligned} B_1 = & V_{pe_1} G_c^+ + V_{pe_2} G_c^+ + V_{e_1c} G_c^+ + V_{pc} G_c^+ + V_{e_1e_2} G_c^+ + V_{e_2c} G_c^+ \\ & + V_{pe_1} G_c^+ V_{pe_1} G_c^+ + V_{pe_2} G_c^+ V_{pe_2} G_c^+ + V_{e_1e_2} G_c^+ V_{e_1e_2} G_c^+ + \dots , \end{aligned} \quad (2.39)$$

$$\begin{aligned} B_2 = & V_{pe_1} G_c^+ V_{pc} G_c^+ + V_{pe_1} G_c^+ V_{e_1c} G_c^+ + V_{pe_1} G_c^+ V_{pe_2} G_c^+ \\ & + V_{pe_1} G_c^+ V_{e_1e_2} G_c^+ + V_{pe_1} G_c^+ V_{e_2c} G_c^+ , \end{aligned} \quad (2.40)$$

$$\begin{aligned} B_3 = & V_{pc} G_c^+ V_{pe_1} G_c^+ + V_{pc} G_c^+ V_{e_1c} G_c^+ + V_{pc} G_c^+ V_{pe_2} G_c^+ \\ & + V_{pc} G_c^+ V_{e_1e_2} G_c^+ + V_{pc} G_c^+ V_{e_2c} G_c^+ , \end{aligned} \quad (2.41)$$

$$\begin{aligned} B_4 = & V_{e_1c} G_c^+ V_{pe_1} G_c^+ + V_{e_1c} G_c^+ V_{pc} G_c^+ + V_{e_1c} G_c^+ V_{pe_2} G_c^+ \\ & + V_{e_1c} G_c^+ V_{e_1e_2} G_c^+ + V_{e_1c} G_c^+ V_{e_2c} G_c^+ , \end{aligned} \quad (2.42)$$

$$\begin{aligned} B_5 = & V_{pe_2} G_c^+ V_{pe_1} G_c^+ + V_{pe_2} G_c^+ V_{pc} G_c^+ \\ & + V_{pe_2} G_c^+ V_{e_1c} G_c^+ + V_{pe_2} G_c^+ V_{e_1e_2} G_c^+ + V_{pe_2} G_c^+ V_{e_2c} G_c^+ , \end{aligned} \quad (2.43)$$

$$\begin{aligned} B_6 = & V_{e_1e_2} G_c^+ V_{pe_1} G_c^+ + V_{e_1e_2} G_c^+ V_{pc} G_c^+ + V_{e_1e_2} G_c^+ V_{e_1c} G_c^+ \\ & + V_{e_1e_2} G_c^+ V_{pe_2} G_c^+ + V_{e_1e_2} G_c^+ V_{e_2c} G_c^+ , \end{aligned} \quad (2.44)$$

$$\begin{aligned} B_7 = & V_{e_2c} G_c^+ V_{pe_1} G_c^+ + V_{e_2c} G_c^+ V_{pc} G_c^+ + V_{e_2c} G_c^+ V_{e_1c} G_c^+ \\ & + V_{e_2c} G_c^+ V_{pe_2} G_c^+ + V_{e_2c} G_c^+ V_{e_1e_2} G_c^+ , \end{aligned} \quad (2.45)$$

$$\begin{aligned} C = & V_{pe_1} G_c^+ G_a^+ V_{pe_1} + V_{pe_1} G_c^+ G_a^+ V_{pe_2} + V_{pe_1} G_c^+ G_a^+ V_{pc} \\ & + V_{pe_2} G_c^+ G_a^+ V_{pe_1} + V_{pe_2} G_c^+ G_a^+ V_{pe_2} + V_{pe_2} G_c^+ G_a^+ V_{pc} \end{aligned}$$

$$\begin{aligned}
& + V_{pc} G_c^+ G_a^+ V_{pe_1} + V_{pc} G_c^+ G_a^+ V_{pe_2} + V_{pc} G_c^+ G_a^+ V_{pc} \\
& + V_{e_1 e_2} G_c^+ G_a^+ V_{pe_1} + V_{e_1 e_2} G_c^+ G_a^+ V_{pe_2} + V_{e_1 e_2} G_c^+ G_a^+ V_{pc} \\
& + V_{e_1 c} G_c^+ G_a^+ V_{pe_1} + V_{e_1 c} G_c^+ G_a^+ V_{pe_2} + V_{e_1 c} G_c^+ G_a^+ V_{pc} \\
& + V_{e_2 c} G_c^+ G_a^+ V_{pe_1} + V_{e_2 c} G_c^+ G_a^+ V_{pe_2} + V_{e_2 c} G_c^+ G_a^+ V_{pc} + \dots .
\end{aligned} \tag{2.46}$$

Higher order terms are obtained by a further iteration of the components of Eqs. (2.37) and (2.46). It is clear from the number of (the lowest order) terms in Eqs. (2.37) and (2.46) that an exact numerical evaluation of the S matrix elements for particle-impact double ionization is extremely difficult. In fact, up to now only few of these terms can be calculated and will be discussed in details in subsequent sections. The expansions (2.37) and (2.46) are nevertheless quite useful for two reasons: (I) For certain experimental arrangements it may well be that some of the terms are predominant. A heuristic way to decide as to which terms are most important is to compare the strength of the two-body interactions Z_{ij}/v_{ij} associated with the various two-body Coulomb potentials. Here Z_{ij} is the product of the charges of particle i and j and v_{ij} is their relative velocity. For example if the projectile is very fast and its charge is not very big one can neglect in G^\pm (Eq. (2.35)) the interaction of the projectile with the target which yields the well-known first-Born approximation. This situation will be discussed at length in the subsequent sections. (II) The multiple scattering expansion (2.37)–(2.46) can serve to understand the underlying physics in that each of the terms can be associated with a certain sequence of binary collisions. In other words all possible (leading order) double ionization pathways are readily extracted by means of Eqs. (2.37)–(2.46).

2.2.1. Double ionization pathways

In the experiment the cross section (2.33) is measured. This quantity, which is defined in a nine-dimensional momentum space spanned by $\mathbf{k}_{1/2}$ and \mathbf{k}_p , is calculated as the coherent sum of all the transition amplitudes associated with the terms (2.37)–(2.46) which may lead to interference phenomena. However, in some regions of the momentum space (that can be selectively probed by the experiment by tuning $\mathbf{k}_{1/2}$ and \mathbf{k}_p appropriately) the matrix elements of some terms in Eq. (2.37)–(2.46) may become particularly dominant. In this section we single out these terms and determine qualitatively the regions in the nine-dimensional momentum space where the mechanisms mediated by the respective terms become operational.

It should be stressed however that the determination procedure used below assumes high impact and high excess energies, i.e. $E_0 \gg \epsilon_a$, $(E_p + E_1 + E_2) \gg \epsilon_c$ so that the momentum components present in the initial bound state become irrelevant. Here, only some selected terms in the expansion Eqs. (2.37)–(2.46) are analyzed. For a more extensive analysis of this kind we refer the reader to Ref. [37].

The terms in the multiple-scattering expansion Eqs. (2.37)–(2.46) can be viewed as follows:

1. The unity operator in Eq. (2.36) corresponds to the non scattered part and is irrelevant here.
2. The first (or second) term in Eq. (2.37) describes an electron–projectile encounter in the field of the atom (Fig. 2.1(a)). The second electron (not interacting directly with the projectile) is emitted by means of scattering from the ionic core and the first electron. This scattering is encompassed in G_a (cf. Eq. (2.19)), i.e. in the undisturbed target system. The kinematical conditions for this process are: $\mathbf{k}_1 \approx \mathbf{k}_0 - \mathbf{k}_p$ and $\mathbf{k}_{\text{ion}} \approx -\mathbf{k}_2$. The assumption underlying this picture is $E_1 \approx E_0 - \epsilon_a$

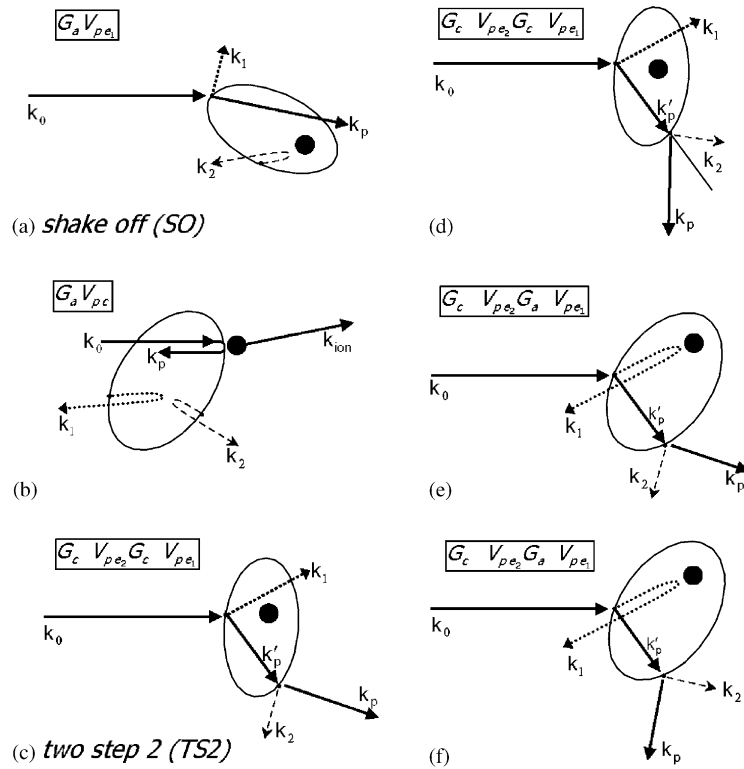


Fig. 2.1. A schematic representation of the scattering mechanisms mediated by the respective transition operators shown in the appropriate inset. The momentum vectors of the incoming and scattered projectile are denoted by arrows labeled \mathbf{k}_0 and \mathbf{k}_p , respectively, whereas the momenta of the two ejected electrons are referred to by the arrows \mathbf{k}_1 and \mathbf{k}_2 . The ionic core is shown as a full dot. The mechanism depicted in the inset (a) is generally referred to as the shake-off process (SO) when $k_p \gg k_2$, $k_1 \gg k_2$. The mechanism shown in the inset (c) is conventionally called the two-step 2 process (TS2).

and $E_2 < \epsilon_a$. It should be noted that this mechanism can also be viewed in terms of the wave functions rather than in terms of G_a . In this case the slow electron is ejected by means of the finite overlap of the initial-state wave function of this electron with the continuum. This process is called shake-off (SO) [62,63].

3. The second term in Eq. (2.37) can be interpreted (see Fig. 2.1(b)) as a direct scattering of the projectile from the ionic core (the atom except for the active electrons). The two active electrons are then ejected due to the electron-electron scattering (and electron-core scattering) as contained in G_a (cf. Eq. (2.19)). The kinematical conditions for this process are $\mathbf{k}_p \approx -\mathbf{k}_0$, $\mathbf{k}_{ion} \approx 2\mathbf{k}_0$ and $\mathbf{k}_1 \approx -\mathbf{k}_2$. Here it is assumed that the experimental conditions are such that $E_1 \approx E_2 < \epsilon_a$ and the velocity of the incoming projectile is much higher than that of the ejected electrons. In the shake-off picture this process can be seen as a double shake-off of the two-electrons upon the sudden removal of the nucleus by the projectile.
4. The fourth and the sixth terms of expansion (2.37) are schematically shown in Fig. 2.1(c). These processes are of a second order in the scattering potential and can be viewed as follows: after a binary collision of the projectile with one of the active electrons, it scatters from the second active

electron. This sequential process shows up in the spectrum at (cf. Fig. 2.1(c)): $\mathbf{k}_1 \approx \mathbf{k}_0 - \mathbf{k}'_p$, $\mathbf{k}_{\text{ion}} \approx 0$ and $\mathbf{k}_2 \approx \mathbf{k}'_p - \mathbf{k}_p$. If the projectile possesses the same mass m_p as the electron mass m_e we arrive at $\mathbf{k}_2 \perp \mathbf{k}_p$, $k_2^2 + k_p^2 = k_p'^2$ and $\mathbf{k}_1 \perp \mathbf{k}'_p$, $k_1^2 + k_p'^2 = k_0^2$. For this process we assume that E_1 and E_2 (and E_0) are much larger than ϵ_a . In the literature this two-step mechanism of double ionization is called TS2 [64].

It is worthwhile to mention that the presence of *two* electrons in the continuum (in addition to the scattered projectile) induces a left-right asymmetry in the intermediate two-particle collision, even in absence of spin-orbit interactions. This dichroic effect, which is absent in an isolated two-particle scattering, is illustrated in Figs. 2.1(c) and (d): The whole experiment as shown in Figs. 2.1(c) and (d) is cylindrically symmetric with respect to \mathbf{k}_0 . However, the two-particle collision between the scattered projectile with (intermediate) momentum \mathbf{k}'_p and the second electron (escaping with momentum \mathbf{k}_2) is generally *not* cylindrically symmetric with respect to \mathbf{k}'_p . I.e., in general the processes depicted in Figs. 2.1(c) and (d) are not identical and will have different matrix elements. This dichroic effect is correlation induced: it is strongly dependent on the interaction of the first electron (with the momentum vector \mathbf{k}_1) with the projectile and the second electron. If electron “1” does not interact with the second electron and with the scattered projectile in the final state, it would not see the difference between the diagrams shown in Fig. 2.1(c) and Fig. 2.1(d). The auxiliary momentum \mathbf{k}'_p cannot be detected in the experiment, it can however be deduced from Fig. 2.1(c) once the measured spectrum can be identified with the scattering mechanism depicted in Fig. 2.1(c).

5. In a *single* ionization experiment the first scattering event (shown in Fig. 2.1(c) and (d)) between the projectile and the first electron results in the well-known “binary peak” [65]. At the opposite direction of the binary peak a further structure appears which is called the “recoil peak” and originates from the scattering of the ionized electron from the ionic core [65].

In the present situation of double ionization the “recoil peak” can be identified by examining the terms shown pictorially in Fig. 2.1(e) and (f) and Figs. 2.2(a) and (b). In Fig. 2.1(e) one of the atomic electrons recoils off the nucleus after a collision with the projectile. The recoil process can in principle be facilitated by the initial-state binding (i.e. by G_a as given by Eq. (2.19)) or by final-state interactions of this electron with the ionic core. The second electron is then ionized upon a single interaction with the projectile. This latter process is not cylindrically symmetric with respect to \mathbf{k}'_p . Therefore, in general there will be a difference between Fig. 2.1(e) and (f) [and Fig. 2.2(a) and (b)]. The kinematical conditions under which the processes Fig. 2.1(e) and (f) are observable in the spectrum are respectively those of Fig. 2.1(c) and (d) except for $\mathbf{k}_{\text{ion}} \approx -\mathbf{k}_1$. In addition, this interpretation assumes that $E_2 \gg E_1$ (and $E_0 \gg \epsilon_a$).

In the cases shown in Fig. 2.2(a) and (b) the first electron escapes directly into the continuum after a single collision with the projectile. The projectile scatters then from the second electron and this electron recoils off the ionic core. The kinematical conditions are then those discussed in Fig. 2.1(d) but the ion has a finite momentum $\mathbf{k}_{\text{ion}} \approx -\mathbf{k}_2$.

6. In Figs. 2.2(c)–(e) the mechanisms for the projectile’s (elastic) back-reflection are displayed along with the respective transition operators (cf. Eq. (2.37)). These mechanisms are particularly relevant for lighter projectiles ($m_p \ll m_c$ where m_c is the mass of the ionic core). Again we notice the appearance of the dichroic effect in Figs. 2.2(d) and (e). In cases of Figs. 2.2(c)–(e) one expects: $\mathbf{k}_{\text{ion}} \approx 2\mathbf{k}_0$. The emergence directions of the collision fragments can then be determined from Eqs. (2.1) and (2.2). For example, if $m_p = m_e$ we arrive for the process of

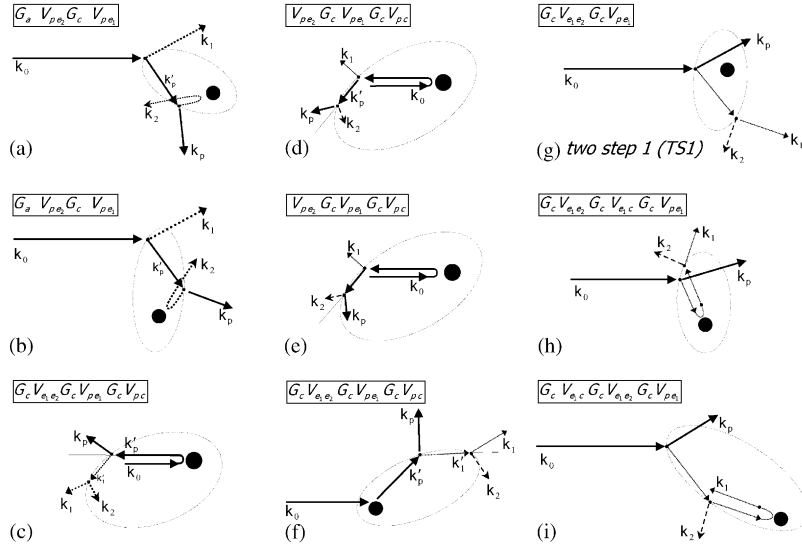


Fig. 2.2. The same as in Figs. 2.1. The mechanisms shown schematically in (g) is often referred to as the two-step 1 process (TS1).

Fig. 2.2(c) at $\mathbf{k}_1 \perp \mathbf{k}_2$ and $k_1^2 + k_2^2 = k_1'^2$. In addition $\mathbf{k}_p \perp \mathbf{k}_1'$ and $k_1'^2 + k_p^2 = k_0'^2 \approx k_0^2$. Hence, if \mathbf{k}_{ion} and \mathbf{k}_p are determined one can deduce \mathbf{k}_1' .

The processes of Figs. 2.2(c)–(e) are distinguishable in that in Fig. 2.2(c) the two electrons emerge in the same half plane (with respect to \mathbf{k}_0) whereas in Figs. 2.2(c)–(e) the active electrons emerge in different half planes. In Fig. 2.2(d) the projectile escapes in between the emission directions of the electrons in contrast to the case shown in Fig. 2.2(e).

7. Further scattering mechanisms in which a direct scattering of the projectile from the ionic core is involved are shown in Fig. 2.2(f) where the projectile scatters from the ionic core and then from one of the active electrons. This excited electron collides then with the other electron and both emerge with momenta \mathbf{k}_1 and \mathbf{k}_2 . The kinematical conditions associated with this process are readily derived from Eqs. (2.1) and (2.2): $\mathbf{k}_1 \perp \mathbf{k}_2$ and $k_1^2 + k_2^2 = k_1'^2$, whereas $\mathbf{k}_1' = \mathbf{k}_0 - \mathbf{k}_{\text{ion}}$. If $m_p = m_e$ then we obtain the relation $\mathbf{k}_p \perp (\mathbf{k}_1 + \mathbf{k}_2)$.
8. In Figs. 2.2(g) and (i) few multiple double scattering mechanisms are depicted in which the electron-electron scattering is involved. In all of these cases the projectile scatters once from one of the active electrons. Subsequently a scattering of this excited electron from the other active electron (and/or from the ionic core) leads to double ionization. The two-step process shown in Fig. 2.2(g) is called conventionally *TS1*. From Eqs. (2.1) and (2.2) we conclude the following conditions for this process: $\mathbf{k}_1 \perp \mathbf{k}_2$ and $\mathbf{k}_{\text{ion}} \approx 0$. In contrast, for the case of Fig. 2.2(h) we obtain the kinematical condition $\mathbf{k}_1 \perp \mathbf{k}_2$, $\mathbf{k}_{\text{ion}} \approx -2(\mathbf{k}_1 + \mathbf{k}_2)$ and $\mathbf{k}_0 + \mathbf{k}_p = -(\mathbf{k}_1 + \mathbf{k}_2)$. In Fig. 2.2(i) we encounter the same situation as in Fig. 2.2(g) however one of the electrons recoils off the ion after the electron-electron single collision. Thus same kinematical conditions as Fig. 2.2(g) applies to Fig. 2.2(i) except that $\mathbf{k}_{\text{ion}} \approx -2\mathbf{k}_1$.

As mentioned above the analysis done for the matrix elements of the various transition operators is rather qualitative. A more precise estimate of the transition amplitudes entails a complicated

multi-dimensional integrals. E.g., McGuire [64] has estimated the importance of the processes SO, TS1, and TS2 in the case of a helium target considering the (integrated) total double ionization cross sections. The cross sections for the TS1 and TS2, are expected to behave essentially as the product of two single ionization cross sections. Thus, these cross sections decrease rapidly with an increasing incident energy (roughly as E_0^{-1}). On the other hand the cross section for the SO mechanism may be considered as the product of one single ionization cross section times a factor which is essentially energy independent. Hence this cross section shows a slower decrease with energy (roughly as $E_0^{-1/2}$). According to McGuire's results [64], the SO contribution should be dominant at electron impact energies larger than ≈ 1 keV.

2.3. Double ionization in the perturbative regime

In the preceding sections we gave a general overview on the formal theory of the double ionization of atomic targets by charged particle impact and pointed out several prominent scattering mechanisms. However, the complexity of even the lowest order terms of the transition matrix elements [cf. Eqs. (2.37) and (2.46)] makes approximate methods unavoidable. Here, perturbation theory offers a useful starting point, once a small parameter of the problem is identified. To identify the interaction to be treated perturbatively we remark that most of the double ionization experiments (with electron projectiles) have been performed in a regime where the projectile is swift (with respect to the Bohr velocity of the initially bound electrons) and transfers only little momentum to the target. Hence a first-order perturbative treatment of the projectile–target interaction is appropriate (we assume that the charge of the projectile is sufficiently small so that $Z_p/v_p \ll 1$). This approximation, which is conventionally called the first Born approximation (FBA), is obtained upon neglecting in the Møller operator $\Omega_f^- [\Omega_i^+]$ in Eq. (2.27) [Eq. (2.28)] any coupling of the projectile to the target, i.e. the FBA Møller operator ω_{FBA}^\pm is obtained from Ω^\pm in the limit of vanishing coupling constant $Z_p \rightarrow 0$.² This means that ω_{FBA}^\pm coincides with the Møller operator of the undisturbed atom $\omega_{\text{FBA}}^\pm = \mathbf{1} + g_a^\pm V_a$, where $V_a = V_{e_1 e_2} + V_{e_1 c} + V_{e_2 c}$ (cf. Eqs. (2.7) and (2.9)). From Eqs. (2.27) and (2.8) it follows that the transition matrix element T_{fi} can be written as

$$T_{fi} = T_{e1} + T_{e2} + T_c, \quad (2.47)$$

$$T_{e1} = \langle \psi^-(\mathbf{k}_1, \mathbf{k}_2), \mathbf{k}_0 | V_{pe1} | \mathbf{k}_0, \varphi_a \rangle = -\frac{Z_p}{2\pi^2 K^2} \langle \psi(\mathbf{k}_1, \mathbf{k}_2) | e^{i\mathbf{K} \cdot \mathbf{r}_1} | \varphi_a \rangle, \quad (2.48)$$

$$T_{e2} = \langle \psi^-(\mathbf{k}_1, \mathbf{k}_2), \mathbf{k}_0 | V_{pe2} | \mathbf{k}_0, \varphi_a \rangle = -\frac{Z_p}{2\pi^2 K^2} \langle \psi(\mathbf{k}_1, \mathbf{k}_2) | e^{i\mathbf{K} \cdot \mathbf{r}_2} | \varphi_a \rangle, \quad (2.49)$$

$$T_c = \langle \psi^-(\mathbf{k}_1, \mathbf{k}_2), \mathbf{k}_0 | V_{pe2} | \mathbf{k}_0, \varphi_a \rangle = \frac{Z_p}{2\pi^2 K^2} \langle \psi(\mathbf{k}_1, \mathbf{k}_2) | 2 | \varphi_a \rangle. \quad (2.50)$$

In these equations the momentum transfer vector $\mathbf{K} = \mathbf{k}_0 - \mathbf{k}_p$ is introduced and the positions of the two electrons with respect to the residual ion are labeled by \mathbf{r}_1 and \mathbf{r}_2 . The wave function $\varphi(\mathbf{r}_1, \mathbf{r}_2)$

² Hereafter we restrict the consideration to Eq. (2.27), equivalent steps apply to Eq. (2.28). Furthermore it is assumed that the residual ion core is structureless.

describes the state of the two electrons bound to the residual core whereas the wave function $\psi_{\mathbf{k}_1, \mathbf{k}_2}^-(\mathbf{r}_1, \mathbf{r}_2)$ stands for the motion of these same electrons in the double continuum of the residual ion. Therefore, in principle the scattering amplitude T_c , given by Eq. (2.50), has to vanish identically since the wave functions $\psi_{\mathbf{k}_1, \mathbf{k}_2}^-(\mathbf{r}_1, \mathbf{r}_2)$ and $\varphi(\mathbf{r}_1, \mathbf{r}_2)$ are eigenfunctions of the same Hamiltonian for different eigenvalues. This fact is not based on physical grounds, it is merely a particular feature of the FBA; using other approximations can lead to a finite projectile scattering from the core. At any case, even within the FBA, the exact forms of these wave functions $\psi_{\mathbf{k}_1, \mathbf{k}_2}^-(\mathbf{r}_1, \mathbf{r}_2)$ and $\varphi(\mathbf{r}_1, \mathbf{r}_2)$ are not known and the overlap of approximate expressions for $\psi_{\mathbf{k}_1, \mathbf{k}_2}^-(\mathbf{r}_1, \mathbf{r}_2)$ and $\varphi(\mathbf{r}_1, \mathbf{r}_2)$ is, in general, finite. The approximate initial and final-state wave functions can nevertheless be orthogonalized by introducing a new final-state wave function as

$$\bar{\psi}_{\mathbf{k}_1, \mathbf{k}_2}^-(\mathbf{r}_1, \mathbf{r}_2) = \psi_{\mathbf{k}_1, \mathbf{k}_2}^-(\mathbf{r}_1, \mathbf{r}_2) - \frac{T_c^*}{2} \varphi(\mathbf{r}_1, \mathbf{r}_2) . \quad (2.51)$$

The term T_c , as given by Eq. (2.50), vanishes when using the wave function $\bar{\psi}_{\mathbf{k}_1, \mathbf{k}_2}^-(\mathbf{r}_1, \mathbf{r}_2)$ to describe the final state of the secondary electrons. It should be noted, however that the overlap integral $\langle \psi_{\mathbf{k}_1, \mathbf{k}_2}^-(\mathbf{r}_1, \mathbf{r}_2) | \varphi(\mathbf{r}_1, \mathbf{r}_2) \rangle$ now enters the definition of the wave function (Eq. (2.51)). Therefore, cross sections calculated using orthogonalized and non-orthogonalized final-state wave functions are in general different and a priori it is not obvious which wave function is more reliable. In the limit of very small momentum transfer $K \ll 1$ the orthogonalized and non-orthogonalized wave functions yields the same transition matrix elements; for in this case the exponentials in Eqs. (2.48) and (2.49) can be expanded with respect to K which leads to the optical relation

$$T_{fi} \propto K \langle \psi_{\mathbf{k}_1, \mathbf{k}_2}^-(\mathbf{r}_1, \mathbf{r}_2) | \hat{\mathbf{K}} \cdot (\mathbf{r}_1 + \mathbf{r}_2) | \varphi(\mathbf{r}_1, \mathbf{r}_2) \rangle + O(K^2) . \quad (2.52)$$

From this relation it is evident that, to a first order in K , the particle-impact double ionization cross sections are closely related to cross sections of double ionization upon absorption of a linearly polarized photon (in the length formulation). The electric field vector is pointing into the \mathbf{K} direction. In the optical limit initial and final states are always orthogonal. This is due to the odd-parity of the dipole operator which imposes that the initial and the final states must have different parities and therefore a vanishing direct overlap. A detailed discussion of the dipolar limit is given in Section 5.

2.3.1. *Scaling properties of the cross sections*

For single ionization by charged-particle impact it is well-established that within the FBA the cross sections satisfy certain scaling properties [66] with respect to the projectile charge and mass state. For the charged particle-impact double-ionization the cross sections also follow a scaling law [67] within the FBA. This law is conveniently derived as follows: We choose an electron as a reference projectile incident with momentum \mathbf{k}_i . In the case of electron-impact double ionization [also called (e,3e)] the momentum vectors of the secondary electrons are traditionally labeled as $\mathbf{k}_b, \mathbf{k}_c$ (cf. Section 4) whereas the momentum vector of the scattered electron is denoted by \mathbf{k}_a . This case [(e,3e)] we compare with a situation where a charged particle with initial momentum \mathbf{k}_0 , mass m_p , and charge z_p double ionizes the target leading to the emission of secondary electrons with vector momenta $\mathbf{k}_1, \mathbf{k}_2$ (Fig. 2.3). In both cases we choose the momentum transfer vectors \mathbf{K} to be identical and $\mathbf{k}_b \equiv \mathbf{k}_1, \mathbf{k}_c \equiv \mathbf{k}_2$. In addition we choose the incident velocities such that $1/k_i = Z_p \mu_{pt} / k_0$ where μ_{pt} is the projectile–target reduced mass. These conditions ensure that the FBA is equally

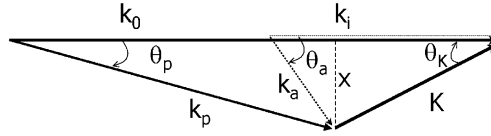


Fig. 2.3. A schematics of the conditions under which one should compare double ionization events upon the impact of a projectile with mass m_p with those following electron impact. The vector momenta of the electrons emitted from the target are the same in both case and therefore are not shown in the drawing. The incident momentum of the electron is \mathbf{k}_i and that of the projectile with mass m_p is \mathbf{k}_0 . In both cases the momentum transfer vector \mathbf{K} is the same. The angle of \mathbf{K} with respect to the incident direction is θ_K . The final-state momentum vector of the electron (the projectile with mass m_p) are \mathbf{k}_a (\mathbf{k}_p) and the associated scattering angle is θ_a (θ_p). The component of the momentum transfer vector transverse to the incident direction is denoted by x .

justified for a variety of projectiles. The imposed constraints for a meaningful comparison are shown schematically in Fig. 2.3.

From Fig. 2.3 we deduce that the scattering angle of the projectile electron θ_a is related to the scattering angle θ_p of other projectiles (with arbitrary masses) via

$$\tan \theta_a = \frac{x}{k_i - K \cos \theta_K}, \quad (2.53)$$

$$\tan \theta_p = \frac{x}{k_0 - K \cos \theta_K}, \quad (2.54)$$

$$\tan \theta_p = \frac{k_i - K \cos \theta_K}{Z_p \mu_{pt} k_i - K \cos \theta_K} \tan \theta_a. \quad (2.55)$$

As depicted in Fig. 2.3 θ_K is the polar angle of the momentum transfer vector with respect to the incident direction and is the same for electron or for other projectiles (per requirement). Under the experimental conditions specified above we conclude from Eqs. (2.34), (2.48)–(2.50) that the scaled cross section $\sigma^* = \sigma/C$ where $C = Z_p^2 \mu_{pt}^2 k_0/k_p$ is independent of the charge and mass state of the projectile. That is, σ^* has to be determined only for one particular projectile, say an electron, while the cross sections for the other projectiles are then deduced via scaling. Since the large majority of experiments have been performed in a regime where the FBA might work we therefore specialize for the rest of this work to the case of electron-impact double ionization, the so-called (e,3e) process. It should be noted however that in recent years several pioneering double-ionization experiments have been performed using ion impact in the regime where the FBA and perturbative treatments in general are expected to break down [23–27,29,30]. In this case it would be valuable to assess the validity of the scaling law (which is exact within the range of validity of the FBA) as a tool to explore the deviations from the perturbative regime.

3. Calculational schemes

The practical calculations of the cross sections for the (e,3e) process entails the evaluation of the transition matrix elements, as given e.g. by Eq. (2.27). This can be done following one of the two

strategies: (1) One solves directly the Lippmann–Schwinger equation for the transition operator, as given by Eq. (2.29). This is done for example by means of a close coupling technique, as discussed below. (2) The second method is to find appropriate expressions for the many-body excited state Ψ^- which enters in the expression for the transition matrix elements (2.27). This may be done as well by solving an integral equation for the wave function of a Lippmann–Schwinger type, however one has then to deal with a number of complications that result from the infinite range of the Coulomb interaction. Therefore, the line followed in practice is to derive expressions for the wave function Ψ^- by solving directly the Schrödinger equation with boundary conditions appropriate for continuum states.

In principle the two approaches are equivalent, however in the perturbative regime the direct calculations of the T -matrix Lippmann–Schwinger equations have yielded till now more accurate results for the cross sections than the wave functions route due to the lack of a precise expression for Ψ^- . On the other hand it has been possible to utilize the wave function method for cross section calculations beyond the non-perturbative. In addition, the wave function Ψ^- describes the excited target independently of the kind of perturbations which trigger the excitation process. I.e. once an acceptable solution for Ψ^- is found it can be employed for any excitation process that leads to Ψ^- . In contrast, the direction evaluation of the transition matrix elements \mathcal{T}_{fi} is restricted to the process associated with \mathcal{T}_{fi} .

As discussed in Section 2.3 the transitions matrix elements simplifies considerably in the perturbative regime with respect to the projectile–target interaction. Fortunately, most of the experimental work has been done in a situation where the FBA might be a useful starting point. Therefore we devote a special attention to this case.

3.1. The many-body wave function approach to double ionization

The wave function Ψ^- which appears in the transition matrix elements (2.27) describes in the simplest case three-continuum electrons moving the field of a doubly charged core (the two knocked-out electrons and the scattered projectile electron). Thus, to obtain the wave function Ψ^- a solution of the four-body Schrödinger equation is required, which cannot be done in an exact manner. Even in the first order perturbation theory as defined in Section 2.3 one needs for the evaluation of the matrix elements (2.48)–(2.50) the three-body wave function ψ^- (two electrons in the field of the residual ion). Again exact expressions for ψ^- are not available. Nevertheless some useful approximations for the four-body and for the three-body wave functions Ψ^- and ψ^- can be obtained from a general consideration of the structure of the Schrödinger equation. The arguments made in the course of the derivation of the approximate expressions for Ψ^- and ψ^- are of a general nature and can be utilized to obtain approximate wave functions for N continuum particles.

For generality we consider N charged particles of equal masses m and with charges Z_j , $j \in [1, N]$ subject to the field of a residual positive charge Z . For our purposes it is justified to neglect terms of the orders m/M (m is the mass of the electron and M is that of the residual ion). In this case the center-of-mass system and the laboratory reference frame coincide. Furthermore, only continuum states are considered, i.e. the total energy E and the particles' energies are high enough so that all particles move in the continuum of the residual ion. The non-relativistic time-independent Schrödinger

equation for the N -body system can be written in position space as

$$\left[H_0 + \sum_{j=1}^N \frac{ZZ_j}{r_j} + \sum_{\substack{i,j \\ j>i=1}}^N \frac{Z_i Z_j}{r_{ij}} - E \right] \Psi(\mathbf{r}_1, \dots, \mathbf{r}_N) = 0, \quad (3.1)$$

where \mathbf{r}_j is the position of particle j with respect to the residual charge Z and $\mathbf{r}_{ij} := \mathbf{r}_i - \mathbf{r}_j$ denotes the relative coordinate between particles i and j . The kinetic energy operator H_0 has the form (in the limit $m/M \rightarrow 0$) $H_0 = -\sum_{\ell=1}^N \Delta_{\ell}/2m$ where Δ_{ℓ} is the Laplacian with respect to the coordinate \mathbf{r}_{ℓ} .

We seek a solution for (3.1) which describes N continuum particles that escape with asymptotic momenta \mathbf{k}_j relative to the residual charge Z . The form of the boundary conditions for this problem has been suggested in Ref. [68], due to an unpublished work by Redmond to be

$$\lim_{\substack{r_{lm} \rightarrow \infty \\ r_n \rightarrow \infty}} \Psi(\mathbf{r}_1, \dots, \mathbf{r}_N) \rightarrow (2\pi)^{-3N/2} \prod_{s=1}^N \xi_s(\mathbf{r}_s) \psi_s(\mathbf{r}_s) \prod_{\substack{i,j=1 \\ j>i}}^N \psi_{ij}(\mathbf{r}_{ij}), \quad \forall l, m, n \in [1, N]; m > l. \quad (3.2)$$

We introduced the functions $\xi_j(\mathbf{r}_j)$, $\psi_j(\mathbf{r}_j)$, $\psi_{ij}(\mathbf{r}_{ij})$ as

$$\xi_j(\mathbf{r}_j) := \exp(i\mathbf{k}_j \cdot \mathbf{r}_j), \quad (3.3)$$

$$\psi_j(\mathbf{r}_j) := \exp[\mp i\alpha_j \ln(k_j r_j \pm \mathbf{k}_j \cdot \mathbf{r}_j)], \quad (3.4)$$

$$\psi_{ij}(\mathbf{r}_{ij}) := \exp[\mp i\alpha_{ij} \ln(k_{ij} r_{ij} \pm \mathbf{k}_{ij} \cdot \mathbf{r}_{ij})]. \quad (3.5)$$

The $+$ and $-$ signs refer to outgoing and incoming wave boundary conditions, respectively, and \mathbf{k}_{ij} is the momentum conjugate to \mathbf{r}_{ij} , i.e. $\mathbf{k}_{ij} := (\mathbf{k}_i - \mathbf{k}_j)/2$. The Sommerfeld parameters α_j, α_{ij} are given by

$$\alpha_{ij} = \frac{Z_i Z_j}{v_{ij}}, \quad \alpha_j = \frac{ZZ_j}{v_j}. \quad (3.6)$$

The total energy of the system E which appears in (3.1) is given by

$$E = \sum_{l=1}^N E_l \quad \text{where} \quad E_l = \frac{k_l^2}{2m}. \quad (3.7)$$

In Eq. (3.6) v_j denotes the velocity of particle j relative to the residual charge whereas $v_{ij} := \mathbf{v}_i - \mathbf{v}_j$. It suffices to restrict the considerations to outgoing-wave boundary conditions. The derivation for incoming-wave boundary conditions runs along the same lines. For the derivation of scattering states that behaves asymptotically according to (3.2) we write for $\Psi(\mathbf{r}_1, \dots, \mathbf{r}_N)$ the ansatz

$$\Psi(\mathbf{r}_1, \dots, \mathbf{r}_N) = \mathcal{N} \Phi_I(\mathbf{r}_1, \dots, \mathbf{r}_N) \Phi_{II}(\mathbf{r}_1, \dots, \mathbf{r}_N) \chi(\mathbf{r}_1, \dots, \mathbf{r}_N). \quad (3.8)$$

The functions Φ_I , Φ_{II} are appropriately chosen and will be specified below, \mathcal{N} is a normalization constant and $\chi(\mathbf{r}_1, \dots, \mathbf{r}_N)$ is a function of an arbitrary form. It is advantageous to choose the function

Φ_I as the solution for the independent particle problem, i.e.

$$\left(H_0 + \sum_{j=1}^N \frac{ZZ_j}{r_j} - E \right) \Phi_I(\mathbf{r}_1, \dots, \mathbf{r}_N) = 0. \quad (3.9)$$

This independent-particle equation is completely separable. For free-particles (i.e. for $Z \equiv 0$) the solution is a product of plane waves $\xi_j(\mathbf{r}_j)$ each describing the free motion of particle j . The function Φ_I has the form

$$\Phi_I(\mathbf{r}_1, \dots, \mathbf{r}_N) = \bar{\Phi}_I(\mathbf{r}_1, \dots, \mathbf{r}_N) \prod_{j=1}^N \xi_j(\mathbf{r}_j). \quad (3.10)$$

From Eq. (3.9) we deduce the regular exact solution Φ_I to be

$$\Phi_I(\mathbf{r}_1, \dots, \mathbf{r}_N) = \prod_{j=1}^N \xi_j(\mathbf{r}_j) \varphi_j(\mathbf{r}_j). \quad (3.11)$$

$\varphi_j(\mathbf{r}_j)$ stands for the confluent hypergeometric function (we use the notation of Ref. [69])

$$\varphi_j(\mathbf{r}_j) = {}_1F_1[\alpha_j, 1, -i(k_j r_j + \mathbf{k}_j \cdot \mathbf{r}_j)]. \quad (3.12)$$

In the case where the continuum particles are strongly coupled to the residual ion, i.e. if $|ZZ_j|/v_j \gg |Z_j Z_i|/v_{ij}; \forall i, j \in [1, N]$ the function Φ_I provides a good approximation to the total wave function, i.e. to Eq. (3.1) since in this case one may neglect the inter-particle interaction in favor of the strong interaction with the ion.

The other extreme case is when the correlation among the continuum particles is very strong (as compared to the interaction strength with the residual ion). This is the case when $|Z_j Z_i|/v_{ij} \gg |ZZ_j|/v_j; \forall i, j \in [1, N]$. To include this limit in the theoretical treatment we choose for Φ_{II}

$$\Phi_{II}(\mathbf{r}_1, \dots, \mathbf{r}_N) = \bar{\Phi}_{II}(\mathbf{r}_1, \dots, \mathbf{r}_N) \prod_{j=1}^N \xi_j(\mathbf{r}_j), \quad (3.13)$$

with

$$\bar{\Phi}_{II}(\mathbf{r}_1, \dots, \mathbf{r}_N) := \prod_{j>i=1}^N \varphi_{ij}(\mathbf{r}_{ij}). \quad (3.14)$$

Here $\varphi_{ij}(\mathbf{r}_{ij}) := {}_1F_1[\alpha_{ij}, 1, -i(k_{ij} r_{ij} + \mathbf{k}_{ij} \cdot \mathbf{r}_{ij})]$. The functions $\varphi_{ij}(\mathbf{r}_{ij}) \prod_{l=1}^N \xi_l(\mathbf{r}_l)$ solve for the Schrödinger Eq. (3.1) in the case of extreme correlations between the particle i and the particle j , i.e. $|ZZ_l| \ll |Z_i Z_j| \gg |Z_m Z_n|, \forall l, m, n \neq i, j$, i.e. it is a solution of the differential equation

$$\left(H_0 + \frac{Z_i Z_j}{r_{ij}} - E \right) \varphi_{ij}(\mathbf{r}_{ij}) \prod_{j=1}^N \xi_j(\mathbf{r}_j) = 0. \quad (3.15)$$

However, in the general case the function (3.13) does not solve for Eq. (3.1) in absence of the field of the residual ion (i.e. for $Z \rightarrow 0$). This is due to the fact that the two-body subsystems formed

by the continuum particles are coupled to each other. From the theory of the interacting electron gas [70] it is well known that this problem is complicated and the appropriate approach depends very much on the strength of the kinetic energy as compared to the potential energy, e.g. for the dense electron gas perturbation theory is a good starting point. In the present case of three and four interacting particles we proceed differently. At first we note that

$$\Delta_m \bar{\Phi}_{\text{II}} = \sum_{l=1}^{m-1} \Delta_m \varphi_{lm} \prod_{\substack{j>i \\ i \neq l}}^N \varphi_{ij} + \sum_{n=m+1}^N \Delta_m \varphi_{mn} \prod_{\substack{j>i \\ j \neq n}}^N \varphi_{ij} + A_m, \quad m \in [1, N], \quad (3.16)$$

where the differential operator A_m has the form

$$\begin{aligned} A_m = & 2 \sum_{l=1}^{m-1} \left[(\nabla_m \varphi_{lm}) \cdot \left(\sum_{n=m+1}^N \nabla_m \varphi_{mn} \right) \right] \prod_{\substack{j>i \\ j \neq n, i \neq l}}^N \varphi_{ij} \\ & + \sum_{l=1}^{m-1} \left[(\nabla_m \varphi_{lm}) \cdot \left(\sum_{\substack{l \neq s=1 \\ s=1}}^{m-1} \nabla_m \varphi_{sm} \right) \right] \prod_{\substack{j>i \\ s \neq i \neq l}}^N \varphi_{ij} \\ & + \sum_{n=m+1}^N \left[(\nabla_m \varphi_{mn}) \cdot \left(\sum_{\substack{t=m+1 \\ t \neq n}}^N \nabla_m \varphi_{mt} \right) \right] \prod_{\substack{j>i \\ j \neq t \neq n}}^N \varphi_{ij} \quad m \in [1, N]. \end{aligned} \quad (3.17)$$

The differential operator that couples the two-body subsystems (in absence of the residual ion field in (3.1), i.e. for $Z=0$) is obtained by substituting the function (3.13) in Eq. (3.1) and making use of the relation (3.16). This leads to the conclusion that the coupling term which prevents separability has the form

$$A = \sum_{m=1}^N A_m. \quad (3.18)$$

The terms A_m are mixing operators that couple, in absence of the residual ion, the individual two-body subsystems that can be formed out of the continuum particles. Hence all the terms in the sum (3.17) vanishes for a three-body system (only one two-body system does exist in absence of the residual ion). From Eq. (3.16) we conclude that the mixing term (3.17) is a part of the kinetic energy operators. Since such parts decay with distance faster than the Coulomb potential one can expect the existence of an ‘‘asymptotic’’ separability, i.e. at large inter-particle distances. To test this anticipation one has to calculate explicitly the term A using the known functional form of $\varphi_{ij}(\mathbf{r}_{ij})$.

To determine the form of the total wave function, i.e. the solution (3.8) of Eq. (3.1), we need, in addition to Φ_{I} and Φ_{II} , an expression for $\chi(\mathbf{r}_1, \dots, \mathbf{r}_N)$. Upon the substitution of the expressions (3.13) and (3.11) into the ansatz (3.8) and insertion in the Schrödinger equation (3.1) we deduce

a differential equation for the determination of $\chi(\mathbf{r}_1, \dots, \mathbf{r}_N)$:

$$\left\{ H_0 - \frac{A}{\bar{\Phi}_{\text{II}}} - \sum_{\ell=1}^N [(\nabla_{\ell} \ln \bar{\Phi}_{\text{I}} + \nabla_{\ell} \ln \bar{\Phi}_{\text{II}}) \cdot \nabla_{\ell} + (\nabla_{\ell} \ln \bar{\Phi}_{\text{I}}) \cdot (\nabla_{\ell} \ln \bar{\Phi}_{\text{II}})] + E \right\} \times \chi(\mathbf{r}_1, \dots, \mathbf{r}_N) = 0 . \quad (3.19)$$

The functions $\bar{\Phi}_{\text{I}}$ and $\bar{\Phi}_{\text{II}}$ have been chosen in such a way that all the two-body Coulomb potentials are diagonalized exactly, as we have shown explicitly above. Therefore, the function χ which is still to be determined, contains information on many-body couplings. To obtain an expression for χ we rewrite it in the form

$$\chi(\mathbf{r}_1, \dots, \mathbf{r}_N) = \prod_{j=1}^N \xi^*(\mathbf{r}_j) [1 - f(\mathbf{r}_1, \dots, \mathbf{r}_N)] , \quad (3.20)$$

where $f(\mathbf{r}_1, \dots, \mathbf{r}_N)$ is an arbitrary function. Inserting (3.20) into Eq. (3.19) leads to the inhomogeneous differential equation

$$\left\{ H_0 - \sum_{\ell=1}^N [\nabla_{\ell} (\ln \bar{\Phi}_{\text{I}} + \ln \bar{\Phi}_{\text{II}}) + i\mathbf{k}_{\ell}] \cdot \nabla_{\ell} \right\} f + \mathcal{R}(1 - f) = 0 . \quad (3.21)$$

The inhomogeneous term \mathcal{R} is given by

$$\begin{aligned} \mathcal{R} := \sum_{m=1}^N \left\{ (\nabla_m \ln \bar{\Phi}_{\text{I}}) \cdot (\nabla_m \ln \bar{\Phi}_{\text{II}}) + \sum_{l=1}^{m-1} \sum_{p=m+1}^N (\nabla_m \ln \varphi_{lm}) \cdot (\nabla_m \ln \varphi_{mp}) \right. \\ \left. + \frac{1}{2} \sum_{l=1}^{m-1} \sum_{s \neq l}^{m-1} (\nabla_m \ln \varphi_{lm}) \cdot (\nabla_m \ln \varphi_{sm}) \right. \\ \left. + \frac{1}{2} \sum_{n=m+1}^N \sum_{n \neq q=m+1}^N (\nabla_m \ln \varphi_{mn}) \cdot (\nabla_m \ln \varphi_{mq}) \right\} . \quad (3.22) \end{aligned}$$

The inhomogeneous term \mathcal{R} contains the coupling between all individual two-particle subsystems: The first term in Eq. (3.22) describes the coupling of a two-body subsystem formed by particles i and j to all two-body subsystems formed by the individual continuum particles and the residual ion. The second term originates from (3.18) and, as explained above, is a measure for the coupling among two-body subsystems of the continuum particles (in absence of Z). For these coupling terms to be negligible the norm of the term \mathcal{R} must be small.

To simplify the structure of \mathcal{R} , as given by (3.22), we note that

$$\nabla_{\ell} \ln \bar{\Phi}_{\text{I}} = \alpha_{\ell} k_{\ell} \mathbf{F}_{\ell}(\mathbf{r}_{\ell}) , \quad (3.23)$$

where

$$\mathbf{F}_{\ell}(\mathbf{r}_{\ell}) := \frac{{}_1F_1[1 + i\alpha_{\ell}, 2, -i(k_{\ell}r_{\ell} + \mathbf{k}_{\ell} \cdot \mathbf{r}_{\ell})]}{{}_1F_1[i\alpha_{\ell}, 1, -i(k_{\ell}r_{\ell} + \mathbf{k}_{\ell} \cdot \mathbf{r}_{\ell})]} (\hat{\mathbf{k}}_{\ell} + \hat{\mathbf{r}}_{\ell}) . \quad (3.24)$$

Furthermore, the relation applies

$$\begin{aligned}\nabla_m \ln \bar{\Phi}_{\text{II}} &= \sum_{n=m+1}^N \nabla_m \ln \varphi_{mn} + \sum_{l=1}^{m-1} \nabla_m \ln \varphi_{lm} \\ &= \sum_{n=m+1}^N \alpha_{mn} k_{mn} \mathbf{F}_{mn}(\mathbf{r}_{mn}) - \sum_{l=1}^{m-1} \alpha_{lm} k_{lm} \mathbf{F}_{lm}(\mathbf{r}_{lm}) ,\end{aligned}\quad (3.25)$$

where

$$\mathbf{F}_{ij}(\mathbf{r}_{ij}) := \frac{{}_1F_1[1 + i\alpha_{ij}, 2, -i(k_{ij}r_{ij} + \mathbf{k}_{ij} \cdot \mathbf{r}_{ij})]}{{}_1F_1[i\alpha_{ij}, 1, -i(k_{ij}r_{ij} + \mathbf{k}_{ij} \cdot \mathbf{r}_{ij})]} (\hat{\mathbf{k}}_{ij} + \hat{\mathbf{r}}_{ij}) . \quad (3.26)$$

The expression \mathcal{R} can then be written in term of $\mathbf{F}_{ij}(\mathbf{r}_{ij})$, $\mathbf{F}_l(\mathbf{r}_l)$, i.e.

$$\begin{aligned}\mathcal{R} &:= \sum_{m=1}^N \left\{ \alpha_m k_m \mathbf{F}_m(\mathbf{r}_m) \cdot \left[\sum_{n=m+1}^N \alpha_{mn} k_{mn} \mathbf{F}_{mn}(\mathbf{r}_{mn}) - \sum_{s=1}^{m-1} \alpha_{sm} k_{sm} \mathbf{F}_{sm}(\mathbf{r}_{sm}) \right] \right. \\ &\quad - \sum_{l=1}^{m-1} \sum_{p=m+1}^N \alpha_{lm} \alpha_{mp} k_{lm} k_{mp} \mathbf{F}_{lm} \cdot \mathbf{F}_{mp} + \frac{1}{2} \sum_{l=1}^{m-1} \sum_{s \neq l}^{m-1} \alpha_{lm} \alpha_{sm} k_{lm} k_{sm} \mathbf{F}_{lm} \cdot \mathbf{F}_{sm} \\ &\quad \left. + \frac{1}{2} \sum_{n=m+1}^N \sum_{q=m+1}^N \alpha_{mn} \alpha_{mq} k_{mn} k_{mq} \mathbf{F}_{mn} \cdot \mathbf{F}_{mq} \right\} .\end{aligned}\quad (3.27)$$

A straightforward approximation is to neglect the term \mathcal{R} altogether. In this case the function $f = 0$ solves for equation (3.21). Then, the solution of Eq. (3.1) takes on the approximate form

$$\Psi(\mathbf{r}_1, \dots, \mathbf{r}_N) \approx \mathcal{N} \prod_{m > l, j=1}^N \zeta_j(\mathbf{r}_j) \varphi_j(\mathbf{r}_j) \varphi_{lm}(\mathbf{r}_{lm}) . \quad (3.28)$$

Thus, the validity of the approximate expression (3.28) is directly related to whether the inhomogeneous term (3.27) can be neglected. Till now, such a justification is documented only in the case of large inter-particle separations. This is readily seen from the asymptotic behaviour of the functions $\mathbf{F}_{ij}(\mathbf{r}_{ij})$, $\mathbf{F}_l(\mathbf{r}_l)$

$$\lim_{r_{ij} \rightarrow \infty} |\mathbf{F}_{ij}(\mathbf{r}_{ij})| \rightarrow \left| \frac{\hat{\mathbf{k}}_{ij} + \hat{\mathbf{r}}_{ij}}{\mathbf{k}_{ij} \cdot (\hat{\mathbf{k}}_{ij} + \hat{\mathbf{r}}_{ij}) r_{ij}} \right| + \mathcal{O}(|k_{ij}r_{ij} + \mathbf{k}_{ij} \cdot \mathbf{r}_{ij}|^{-2}) , \quad (3.29)$$

which implies that \mathcal{R} diminishes faster than the Coulomb potential in the asymptotic regime, i.e.

$$\lim_{\substack{r_{ij} \rightarrow \infty \\ r_l \rightarrow \infty}} \mathcal{R} \rightarrow \mathcal{O}(|k_{ij}r_{ij} + \mathbf{k}_{ij} \cdot \mathbf{r}_{ij}|^{-2}, |k_l r_l + \mathbf{k}_l \cdot \mathbf{r}_l|^{-2}) \quad \forall j > i, l \in [1, N] . \quad (3.30)$$

Thus the approximation (3.28) is justified in the asymptotic region and possesses the correct boundary conditions (3.2) in the limit of large inter-particle separations. It should be stressed however that, in contrast to the function given by Eq. (3.2), the wave function (3.28) is defined in the entire Hilbert space and diagonalizes all the two-body potentials at any distance. A further important remark

concerning the utilization of the wave function (3.28) for the calculations of the cross sections is that the limit Eq. (3.30) is energy dependent. With increasing velocities of the escaping particles the asymptotic region is reached faster, i.e. the asymptotic regime covers a much larger area for fast particles than for slow ones. Therefore, the wave function (3.28) is a high energy approximation. Nevertheless, the method has been applied at low energies as well. In this case the reliability of this approach is not clear from a mathematical point of view.

3.1.1. Normalization of the N -body wave functions

For the evaluation of cross sections using the wave function (3.28) it is decisive to have an accurate expression for the normalization factor \mathcal{N} of the wave function (3.28); since it is this factor which determines the overall structure of the phase space available for the continuum particles. Traditionally \mathcal{N} is determined by solving a $3N$ -dimensional integral over the norm of the function (3.28). Obviously this task is intractable for an arbitrary number N of continuum particles. Alternatively, one can obtain the factor \mathcal{N} from flux arguments, i.e. by requiring that the flux through an asymptotic manifold defined by a constant large inter-particle separations should be the same, regardless of whether we use the wave function (3.28) and calculate the flux (\mathbf{J}_Ψ) or if we employ normalized plane-waves which generate the flux \mathbf{J}_{PW} . On the other hand the plane-wave flux is given by

$$\begin{aligned} \mathbf{J}_{PW} &= -\frac{i}{2}(2\pi)^{-3N} \left\{ \prod_l^N \xi_l^*(\mathbf{r}_l) \nabla \left[\prod_l^N \xi_l(\mathbf{r}_l) \right] - \prod_l^N \xi_l(\mathbf{r}_l) \nabla \left[\prod_l^N \xi_l^*(\mathbf{r}_l) \right] \right\} \\ &= (2\pi)^{-3N} \sum_{l=1}^N \mathbf{k}_l . \end{aligned} \tag{3.31}$$

Here the total gradient $\nabla := \sum_{l=1}^N \nabla_l$ has been introduced. For the evaluation of the flux \mathbf{J}_Ψ which is related to the wave function (3.28) one needs the total gradient of the wave function. This is derived by exploiting Eqs. (3.23) and (3.25) which yields

$$\begin{aligned} \nabla \Psi := \mathcal{N} \sum_{m=1}^N \left\{ \mathbf{i} \mathbf{k}_m \Psi + \alpha_m k_m \mathbf{F}_m \Psi + \left[\sum_{n=m+1}^N \alpha_{mn} k_{mn} \bar{\mathbf{F}}_{mn}(\mathbf{r}_{mn}) \prod_{\substack{j>i \\ j \neq n}}^N \varphi_{ij} \right. \right. \\ \left. \left. - \sum_{l=1}^{m-1} \alpha_{lm} k_{lm} \bar{\mathbf{F}}_{lm}(\mathbf{r}_{lm}) \prod_{\substack{j>i \\ i \neq l}}^N \varphi_{ij} \right] \prod_{s=1}^N \xi_s(\mathbf{r}_s) \varphi_s(\mathbf{r}_s) \right\} . \end{aligned} \tag{3.32}$$

Here we used the notation $\bar{\mathbf{F}}_{mn} = \mathbf{F}_{mn} \varphi_{mn}$. Since only the asymptotic flux is considered, i.e. the flux at large inter-particle distances, only the first term of Eq. (3.32) is relevant, as can be deduced from Eqs. (3.24) and (3.26). Taking the asymptotic expansion of the confluent hypergeometric

function [69] into account we derive for the flux \mathbf{J}_ψ

$$\mathbf{J}_\psi = \mathcal{N}^2 \prod_{j=1}^N \frac{\exp(\pi\alpha_j)}{\Gamma(1-i\alpha_j)\Gamma^*(1-i\alpha_j)} \prod_{m>l=1}^N \frac{\exp(\pi\alpha_{lm})}{\Gamma(1-i\alpha_{lm})\Gamma^*(1-i\alpha_{lm})} \sum_{n=1}^N \mathbf{k}_n, \quad (3.33)$$

where $\Gamma(x)$ is the Gamma function. From the requirement that asymptotically $\mathbf{J}_\psi = \mathbf{J}_{\text{PW}}$ and from Eqs. (3.31) and (3.33) we conclude that the normalization constant has the form

$$\mathcal{N} = (2\pi)^{-3N/2} \prod_{j=1, m>l=1}^N \exp[-\pi(\alpha_{lm} + \alpha_j)/2] \Gamma(1-i\alpha_j) \Gamma(1-i\alpha_{lm}). \quad (3.34)$$

For two charged particles moving in the field of a heavy nucleus the wave function (3.28) with the normalization, given by Eq. (3.34), simplifies to the three-body wave function proposed in Refs. [71]. This simplified form is needed in the perturbative regime, i.e. when calculating (2.48)–(2.50).

3.2. First-order perturbation treatments

As discussed in Section 2.3, in a first-order (Born) treatment of the projectile target interaction, the description of the double ionization reduces to the treatment of a three-body continuum state (the two knocked out electrons and the positive ion). This section deals with the calculational schemes in this regime.

3.2.1. The three-body Coulomb wave approach: The 3C method

In this method Eq. (3.28) for $N=3$ is utilized for the description of the motion of the knocked-out electrons as they move in the double continuum of the residual ion (the projectile electron moves freely). The matrix elements (2.48)–(2.50) are then evaluated numerically to yield the (e,3e) cross sections. In the literature this approach is called the 3C method which stand for the three-body Coulomb wave method. Generalization to the non-perturbative regime is straightforward by choosing in Eq. (3.28) $N=4$, as done in Ref. [46]. However, rather sophisticated numerical methods are then needed to evaluate the nine-dimensional integrals as given by Eq. (2.27).

3.2.2. The convergent close coupling approach: The CCC method

In this theory the transition matrix elements are evaluated by solving a Lippmann–Schwinger equation for the three-body problem. This approach has been implemented within the FBA only. Hitherto only the electron-impact double-ionization of an atomic helium target has been treated with this method.

To evaluate the matrix elements (2.48)–(2.50) one proceeds as follows. The (Born) transition operators $\exp(i\mathbf{K} \cdot \mathbf{r}_{b/c})$ is expanded in multipoles where $\hat{\mathbf{K}}$ is chosen as the quantization axis, i.e.

$$\exp(i\mathbf{K} \cdot \mathbf{r}_{b/c}) = \sqrt{4\pi} \sum_J i^J j_J(Kr_{b/c}) \sqrt{2J+1} Y_{J0}(\hat{\mathbf{r}}_{b/c}). \quad (3.35)$$

Here $Y_{JM}(\hat{\mathbf{r}})$ denotes a standard spherical harmonic as function of the direction $\hat{\mathbf{r}}$ and J, M is an angular quantum number and its projection on the quantization axis. Expansion (3.35) allows to perform the angular integration involved in (2.48)–(2.50). The cross sections (2.34) expressed in

terms of spherical harmonics reads

$$\sigma = \frac{8k_a}{k_0} \frac{1}{K^4} \left| \sum_J \sum_{l_1 l_2} \sum_{m_1 = -m_2} i^{J-l_1-l_2} Y_{l_1 m_1}(\hat{\mathbf{k}}_b) Y_{l_2 m_2}(\hat{\mathbf{k}}_c) \begin{pmatrix} l_1 & J & l_2 \\ m_1 & 0 & m_2 \end{pmatrix} \right. \\ \left. \times \exp[i(\delta_{l_1} + \delta_{l_2})] (2J + 1) [\mathcal{M}_{Jl_1 l_2}(K, k_b, k_c) + \mathcal{M}_{Jl_2 l_1}(K, k_c, k_b)] \right|^2. \quad (3.36)$$

The angular-independent matrix elements $\mathcal{M}_{Jl_1 l_2}$ are then calculated by means of a convergent close coupling technique (CCC). This is achieved by expanding the final two-electron continuum state using square-integrable (L^2) states and solving for the atomic scattering of one of the target electrons from the singly charged ion. I.e., upon the perturbation of the target by the passing projectile one of the target electron is elevated in energy. It then re-scatters from the singly ionized target ejecting the second electron. This latter process is treated in a non-perturbative way. Technically [36,19,8], the double ionization processes are identified as an excitation of the positive-energy pseudostates of the ion. Thus in the final state one of the ejected electron occupies a true continuum state with energy E_b and orbital angular momentum l_1 whereas the other electron resides in an excited state of the ionic which is labeled by l_2 with energy E_c . Therefore, the boundary conditions employed by the CCC are appropriate for situations where the “excited” electron shields the residual ion field which is experienced by the true continuum electron. This is done irrespective of the energies E_b and E_c . Nevertheless, since the initial bound state which enters the matrix elements (2.48)–(2.50) is well localized, the boundary conditions seem to be of a minor importance as far as the numerical results are concerned.

In recent years there has been an impressive amount of work concerning the solution of the three-body problem as well as improving on the 3C model. It is beyond the scope of the present article to cover all these topics. Here we discuss only those theories that have been applied to the case of particle-impact double ionization. The interested reader is referred to Refs. [68,71–83] where further references can be found.

3.3. Beyond the perturbative regime

The treatment of the projectile–target interaction within the first order perturbation theory (i.e. within FBA) brings about significant simplifications in that one only needs to describe two-electron transitions of the target. As will be shown below however, the experimental results indicate some deficiency of the FBA treatment, even in the high energy regime. Therefore, and in view of the planned experiments in the low-energy regime, a theoretical treatment is desirable that takes account of the projectile–target interaction in a dynamical way.

3.3.1. The second Born approximation (2BA)

One obvious extension is the second Born approximation. It takes into account the successive interactions of the incoming electron with the two target electrons [40]. The intermediate state of the scattered electron is described by a plane wave. This electron collides with the second bound electron after having singly ionized the target without or with simultaneous excitations. This process corresponds to the TS2 mechanism discussed above (cf. Fig. 2.1). Because of these two successive

interactions the symmetry with respect the momentum transfer is broken. Similar effects arise when using the second Born approximation to describe the electron-impact single ionization [the (e,2e) process] at low incident energies [84]. In the second Born calculations done so far for the (e,3e) process, the final state has been modeled by a 3C wave function. Alternatively, to reduce the computational efforts, Ref. [40] uses a product of two Coulomb wave functions multiplied by the density of state corresponding the final state interaction of the two slow electrons. One of the principal difficulties of the calculations is that the integration over the intermediate scattered-electron states may well be singular and these singularities should be treated carefully.

3.3.2. The four-body Coulomb wave function: The 6C approach

A further method which goes beyond the FBA is to evaluate the matrix elements (2.27) using the wave function (3.28) with $N = 4$, as done in Ref. [46]. As clear from Eq. (3.28) the wave function consists in this case of a product of six two-body Coulomb waves (and therefore the name 6C), each describing the scattering within the individual two-body subsystems that can be combined within a four-body systems. Thus, all the four continuum particles are treated on equal footing, i.e. this treatment goes beyond the second Born type. The connection between the perturbation theory and the use of the 6C wave function is best illustrated within the Green function formalism, as done in Ref. [81]. There it is shown that the use of (3.28) implies that all two-particle collisions are treated to infinite orders. The treatment of the projectile target interaction within this scheme resembles then the so-called ladder-approximation which is well-known in the realm of many-body theory [70]. The price to be payed for using the sophisticated 6C wave function [Eq. (3.28) with $N = 4$] is that one has to deal with the nine dimensional integrals (2.27) in the continuum which is a serious problem. In certain situations this numerical obstacle has been tackled [46] successfully.

3.3.3. Dynamical screening and effective charges: The C4FS method

The numerical problems in using (3.28) for $N = 4$ can be circumvented by the following observation. In the Schrödinger equation (3.1) the term which prevents separability is the inter-particle interaction potential $Z_i Z_j / r_{ij}$. If it were not for this term the complete problem reduces to Eq. (3.9) which is exactly solvable (the solution of which we derived as Eq. (3.11)). Thus, if an approximate method is developed which encompasses the correlation term $Z_i Z_j / r_{ij}$ into the potentials $Z_j Z / r_j$ in an effective, position-independent manner, the complete Schrödinger equation (3.1) can then be solved by a function of form (3.11). This scheme is realized by the effective charge method which will be illustrated for the electron-impact double ionization. For the general case we refer to Ref. [81].

For the (e,3e) the final state consists of three interacting electrons labeled a, b, c moving in the field of a nucleus of charge $Z_T = 2$. Thus the total potential in Eq. (3.1) reduces to

$$-\frac{Z_T}{r_a} - \frac{Z_T}{r_b} - \frac{Z_T}{r_c} + \frac{1}{r_{ab}} + \frac{1}{r_{ac}} + \frac{1}{r_{bc}} = \frac{Z_b}{r_b} + \frac{Z_c}{r_c} + \frac{Z_{bc}}{r_{bc}}. \quad (3.37)$$

Here Z_b, Z_c, Z_{bc} are introduced as unknown functions yet to be determined. Their functional form is specified by a linear expansion in terms of the two-body interactions, as explained in Ref. [85]. For this expansion to be exact we require Eq. (3.37) to be identically fulfilled and the boundary conditions imposed on (3.1) are not violated. The approximation which makes this procedure favorable for

numerical calculations is the assumption $r_j \propto k_j$, $j = a, b, c$, which yields for the effective charges

$$\begin{aligned} Z_b &= -Z_T - \frac{Z_T}{2} \frac{k_b}{k_a} + \frac{k_b}{|\mathbf{k}_a - \mathbf{k}_b|} , \\ Z_c &= -Z_T - \frac{Z_T}{2} \frac{k_c}{k_a} + \frac{k_c}{|\mathbf{k}_a - \mathbf{k}_c|} , \\ Z_{bc} &= 1 . \end{aligned} \tag{3.38}$$

With these effective charges it is readily concluded that the eigenfunction of (3.1) can be approximated by

$$\Psi_{\mathbf{k}_a, \mathbf{k}_b, \mathbf{k}_c}(\mathbf{r}_a, \mathbf{r}_b, \mathbf{r}_c) \approx (2\pi)^{-3/2} \exp(i\mathbf{k}_a \cdot \mathbf{r}_a) \psi ,$$

where

$$\begin{aligned} \psi &= (2\pi)^{-3} N \exp(i\mathbf{k}_b \cdot \mathbf{r}_b + i\mathbf{k}_c \cdot \mathbf{r}_c) {}_1F_1(i\alpha_{bc}, 1, -i[k_{bc}r_{bc} + \mathbf{k}_{bc} \cdot \mathbf{r}_{bc}]) \\ &\quad {}_1F_1(i\alpha_b, 1, -i[k_b r_b + \mathbf{k}_b \cdot \mathbf{r}_b]) {}_1F_1(i\alpha_c, 1, -i[k_c r_c + \mathbf{k}_c \cdot \mathbf{r}_c]) . \end{aligned} \tag{3.39}$$

The normalization factor is

$$N = \exp(-\pi\alpha_{bc}/2) \Gamma(1 - i\alpha_{bc}) \exp(-\pi\alpha_b/2) \Gamma(1 - i\alpha_b) \exp(-\pi\alpha_c/2) \Gamma(1 - i\alpha_c) .$$

Here the effective Sommerfeld parameters have been defined as $\alpha_c = Z_c/k_c$, $\alpha_b = Z_b/k_b$ and $\alpha_{bc} = Z_{bc}/(2k_{bc})$, where \mathbf{k}_{bc} is the momentum conjugate to \mathbf{r}_{bc} .

It should be noted that the approximation $k_j \propto r_j$ which lead to the wave function (3.39) does not mean that this treatment of the (e,3e) process is classical. In fact we are utilizing the wave function (3.39) to perform the calculations. Our approximation means merely that the total potential (3.37) is exactly diagonalized by (3.39) along the trajectories for which $k_j \propto r_j$.

Since the functions Z_j , $j = a, b, c$ are position independent, the transition amplitude (2.27) is readily reduced to the form (2.48)–(2.50) derived in Section 2.3.

The amplitudes $T_{e1} \equiv T_{ab}$, $T_{e2} \equiv T_{ac}$, $T_c \equiv T_a$ describe, respectively, the *direct* scattering of the projectile electron (*a*) from the two electrons (*b, c*) bound to the target and from the nucleus. Multiple scattering events within the four-body system are contained in $|\Psi\rangle$ as final state interactions. The transition matrix elements T_{fi} depend dynamically on all four vector momenta $\mathbf{k}_0, \mathbf{k}_a, \mathbf{k}_b, \mathbf{k}_c$, as evident from Eqs. (3.38) and (3.39): If the projectile electron approaches in velocity space one of the ejected electrons, say electron *b* the interaction of this ejected electron with the residual ion turns repulsive (i.e. Z_b , as defined by Eq. (3.38) becomes positive) as to simulate the repulsion between the scattered and the ejected electron *b*. For this reason the wave function (3.39) is called the C4FS which stands for Coulomb four body final-state wave function. In contrast within the first Born approximation (FBA) the effective charges in Eqs. (3.38) reduce to $Z_b = -Z = Z_c$, $Z_{bc} = 1$ and T_{fi} depends dynamically only on \mathbf{K} , \mathbf{k}_b and \mathbf{k}_c .

3.3.4. The many-body Green function theory: The GF method

All the methods discussed so far deals with the double ionization by evaluating in some way the wave functions of the excited electrons and calculating the desired transition matrix elements. This approach is suitable for few-particle systems but it becomes inappropriate for large systems. This is not only because of the dramatically increasing complexity of the wave functions with

increasing number of particles (cf. Eq. (3.28)). For “large systems”, i.e. in the thermodynamic limit, new macroscopic phenomena appear like collective modes, phase transitions and thermodynamic properties. While many of the macroscopic properties are strictly defined for infinitely large systems with constant density, it turns out that the onset of these macroscopic features can also be observed in finite systems [83]. Thus it is desirable to develop a method that is conceptually and practically applicable for finite systems, like the four-body problem and that offers a tractable scheme for the treatment of systems with a larger number of interacting particles. The ideal tool for this purpose is the Green function technique. Here we will briefly sketch the method as applied to the four-body problem. Applications of this same approach to critical phenomena in finite systems can be found in Ref. [83].

3.3.4.1. The Green function expansion. Let us consider a non-relativistic system consisting of N particles that interact via two-body potentials v_{ij} , as for example in Eq. (3.1). The total potential is then $U^{(N)} = \sum_{j>i=1}^N v_{ij}$ (there is no need to specify the form of v_{ij}). The function $U^{(N)}$ satisfies the recurrence relations [86]

$$U^{(N)} = \frac{1}{N-2} \sum_{j=1}^N u_j^{(N-1)}, \quad (3.40)$$

$$u_j^{(N-1)} = \frac{1}{N-3} \sum_{k=1}^{N-1} u_k^{(N-2)}, \quad j \notin [1, N-1], \quad (3.41)$$

where $u_j^{(N-1)}$ stands for the total potential of a system of $N-1$ interacting particles in which the j particle is missing. It has been shown using operator algebra that the recurrence relations (3.40) and (3.41) are reflected in similar relations for the total Green operator $G^{(N)}$ and for the transition operators $T^{(N)}$ [86]:

$$T^{(N)} = \sum_{j=1}^N T_j^{(N-1)}, \quad (3.42)$$

$$T_j^{(N-1)} = \tilde{u}_j^{(N-1)} + T^{(N)} G_0 \tilde{u}_j^{(N-1)}, \quad j \in [1, N]. \quad (3.43)$$

Here we defined the scaled potentials $\tilde{u}_j^{(N-1)} = (u_j^{(N-1)})/(N-2)$. The operators $T^{(N)}$ are related to the transition operator $t_j^{(N-1)}$ of a system with $N-1$ particles that interact via the scaled potential $\tilde{u}_j^{(N-1)}$ (i.e. $t_j^{(N-1)} = \tilde{u}_j^{(N-1)} + \tilde{u}_j^{(N-1)} G_0 t_j^{(N-1)}$):

$$\begin{pmatrix} T_1^{(N-1)} \\ T_2^{(N-1)} \\ \vdots \\ T_{N-1}^{(N-1)} \\ T_N^{(N-1)} \end{pmatrix} = \begin{pmatrix} t_1^{(N-1)} \\ t_2^{(N-1)} \\ \vdots \\ t_{N-1}^{(N-1)} \\ t_N^{(N-1)} \end{pmatrix} + [\mathbf{K}^{(N-1)}] \begin{pmatrix} T_1^{(N-1)} \\ T_2^{(N-1)} \\ \vdots \\ T_{N-1}^{(N-1)} \\ T_N^{(N-1)} \end{pmatrix}. \quad (3.44)$$

The kernel $[\mathbf{K}^{(N-1)}]$ is a matrix operator and is given by

$$[\mathbf{K}^{(N-1)}] = \begin{pmatrix} 0 & t_1^{(N-1)} & t_1^{(N-1)} & \dots & t_1^{(N-1)} \\ t_2^{(N-1)} & 0 & t_2^{(N-1)} & \dots & t_2^{(N-1)} \\ \dots & \dots & \dots & \dots & \dots \\ t_{N-1}^{(N-1)} & \dots & t_{N-1}^{(N-1)} & 0 & t_{N-1}^{(N-1)} \\ t_N^{(N-1)} & \dots & t_N^{(N-1)} & t_N^{(N-1)} & 0 \end{pmatrix} G_0 . \tag{3.45}$$

Eq. (3.41) makes clear that $t_j^{(N-1)}$ is expressible in terms of the transition operators of the $N - 2$ interacting subsystems as $t_j^{(N-1)} = \sum_{k \neq j}^{N-1} T_k^{(N-2)}$, where the operators $T_k^{(N-2)}$ are deduced from Eq. (3.44) with N being replaced by $N - 1$.

Since the relation $G^{(N)} = G_0 + G_0 T^{(N)} G_0$ applies we conclude that the Green operator of the interacting N particle system has the form $G^{(N)} = G_0 + \sum_{j=1}^N G_j^{(N-1)}$. The operators $G_j^{(N-1)}$ are related to the Green operators $g_j^{(N-1)}$ of the systems in which only $N - 1$ particles are correlated by virtue of $\tilde{u}_j^{(N-1)}$. This interrelation is given via

$$\begin{pmatrix} G_1^{(N-1)} \\ G_2^{(N-1)} \\ \vdots \\ G_{N-1}^{(N-1)} \\ G_N^{(N-1)} \end{pmatrix} = \begin{pmatrix} g_1^{(N-1)} - G_0 \\ g_2^{(N-1)} - G_0 \\ \vdots \\ g_{N-1}^{(N-1)} - G_0 \\ g_N^{(N-1)} - G_0 \end{pmatrix} + [\tilde{\mathbf{K}}^{(N-1)}] \begin{pmatrix} G_1^{(N-1)} \\ G_2^{(N-1)} \\ \vdots \\ G_{N-1}^{(N-1)} \\ G_N^{(N-1)} \end{pmatrix} , \tag{3.46}$$

where $[\tilde{\mathbf{K}}^{(N-1)}] = G_0 [\tilde{\mathbf{K}}^{(N-1)}] G_0^{-1}$. Hence, if the Green operator of the interacting $N - 1$ body system is known the Green operator of the N particles can then be deduced by solving a set of N linear, coupled integral equations (namely Eqs. (3.44), (3.46)). If only the solution of the $N - M$ problem is known where $M \in [1, N - 2]$ one has to perform a hierarchy of calculations starting by obtaining the solution for the $N - M + 1$ problem and repeating the procedure to reach the solution of the N body problem. For $N = 3$ the present scheme reduces to the well established Faddeev equations [87,88]. These relations for the Green's function have far reaching consequences, as they relate the spectral and thermodynamic properties of a many-body interacting system to the strength of the residual interactions: In each step in the recurrence loop (3.41) the interactions in the system is diluted by cutting all interaction lines to the particle which is removed from the system.

3.3.4.2. Application to the four-body problem. Using the above GF technique the four body Green operator can be expressed in terms of approximate solutions of three body systems. Methods to obtain the latter have been discussed in the previous sections. For $N = 4$ the first iteration of Eq. (3.46) yields

$$G^{(4)} = \sum_{j=1}^4 g_j^{(3)} - 3G_0 , \tag{3.47}$$

where $g_j^{(3)}$ is the Green operator of the interacting three body system (particle j is non-interacting). This $g_j^{(3)}$ we assume is known in some approximate form. For example, within the 3C or the C4FS approach the Hamiltonian of the three body system reduces to a sum of three commuting Hamiltonians $h_k^{(2)}$ in which only two particles are interacting (particle k is free). Therefore, the three-body Green function is approximated within the 3C-type approaches by $g_j^{(3)} \approx G_0^{-2} \prod_{k=1}^{(3)} g_k^{(2)}$, $k \neq j \in [1, 4]$ where $g_k^{(2)}$ is the resolvent of $h_k^{(2)}$. Employing this expression for the three-body Green's function, the present procedure [Eq. (3.47)] yields for the four-body GF $G^{(4)} = [\sum_{j=1}^4 G_0^{-2} \prod_k^3 g_k^{(2)}] - 3G_0$, $j \neq k$. A well-known advantage of the GF method is its flexibility and versatility. For example if parts of the problem can be conveniently solved numerically or analytically one can choose the reference Green's function G_0 as to encompass these solutions. For example in the GF calculations for the (e,3e) process shown in the next section the reference GF G_0 is chosen to be the Green operator of the three continuum particles moving independently in the Coulomb nuclear field. What remains in the potential (3.40) are the correlation terms among the continuum particles that are treated according to the method presented above.

4. Experimental techniques

In the preceding sections we gave a general overview on the theory of double ionization of atomic targets by charged particle impact and pointed out several prominent scattering mechanisms. However, most of the experiments have been performed in the regime where the projectile is swift (with respect to the Bohr velocity of the initially bound electrons) and transfers only little momentum to the target. Hence first-order perturbative treatments with regard to the projectile-target interaction are expected to yield useful results (this implies that the charge of projectile is sufficiently small so that $Z_p/v_p \ll 1$). As shown above, in this regime, the cross sections satisfy a scaling law that allows to relate the double ionization with projectiles having arbitrary masses and charges to the electron-impact double ionization. Therefore, we specialize for the rest of this work to the case of electron-impact double ionization, i.e. the (e,3e) process. It should be noted however that in recent years several pioneering double-ionization experiments have been performed using highly charged ions in a regime where perturbative treatments are expected to break down [23–27,29,30]. The physics underlying these non-perturbative processes is not discussed here. We start this part of the article by a detailed discussion of the experimental techniques used in (e,3e) processes.

4.1. Notations

The reaction leading to the electron impact direct double ionization of a target X can be symbolically written as



This reaction conserves the total energy and the total linear momentum, as stated by Eqs. (2.1) and (2.2). The outgoing electrons, though indistinguishable, are indexed a for the fast “scattered” one and b and c for the slow “ejected” ones. The atom and the residual ion are assumed to be in their ground state. The ion recoil energy E_{ion} is generally negligible because of the smallness of

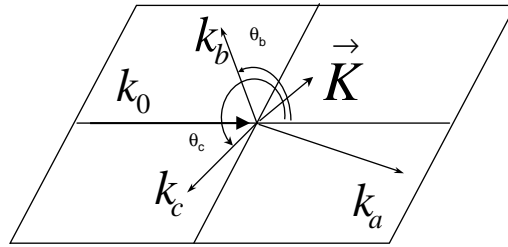


Fig. 4.1. The coplanar scattering geometry for the (e,3e) experiments. The two ejected electrons with momenta \mathbf{k}_b and \mathbf{k}_c are detected in the plane defined by the incoming and the scattered projectile with momentum vectors \mathbf{k}_0 and \mathbf{k}_a , respectively. The momentum transfer is labelled as \mathbf{K} .

the electron to ion mass ratio. The recoil ion momentum \mathbf{k}_{ion} is obtained by subtracting from the momentum transfer vector \mathbf{K} the momentum of the center of mass of the ejected electron, $(\mathbf{k}_b + \mathbf{k}_c)$. A general schematic diagram for the experiment is shown in Fig. 4.1. In the particular case of a coplanar geometry, all electrons are observed in the collision plane at in-plane angles θ_a, θ_b and θ_c with respect to the incident direction, while the out-of-plane (azimuthal) angles φ_b and φ_c are set to 0 or π . The mutual angle $\theta_{cb} = \theta_b - \theta_c$ is also often used. In what follows we consider the case of fully differential experiments with completely determined kinematics (apart from spin and magnetic sublevels), where all three final electrons are simultaneously analysed both in direction and in energy and are detected in coincidence. This allows one to determine the energy state in which the ion is left, i.e. to find the orbitals from which the outgoing electrons are knocked. But the price to be paid for that is the need for multiple coincidence techniques which make these experiments far more difficult than the corresponding (e,2e) single ionization ones, the addition of an extra solid angle of detection for the third electron, $\Delta\Omega$, roughly resulting in a reduction of the overall collection efficiency by a factor $\Delta\Omega/4\pi$. In addition, the double ionization cross section is typically two orders of magnitude smaller than the single ionization cross section. This puts two major constraints on the design of an (e,3e) experiment: the achievement of a large luminosity without degrading too much the energy and angular resolutions, and the need to use multi-detection techniques to reduce the necessary accumulation time.

4.2. Overview on measured double ionization cross sections

Because a double ionization experiments involves many variables (10 variables: $E_0, E_j, \theta_j, \varphi_j$ with $j = a, b, c$) linked by the energy and momentum conservations, we pay a particular attention to the terminology used and to a precise definition of n -fold differential cross sections. Extensive experimental and theoretical information exists on *total* double ionization cross sections under various projectiles impact. Such studies usually determine only the ratio σ^{2+}/σ^+ of double (σ^{2+}) to single (σ^+) ionization cross sections as a function of the incoming particle energy, and are therefore not sensitive to finer details of the ionization dynamics. *Differential* cross sections with respect to the energies and/or solid angles of emission of the final particles have seldom been reported, and discussion has been there mostly concentrated on integral characteristics determined from single or double differential cross sections. Cross sections for multiple ionization which are singly differential (SDCS) with respect to the energy-loss of the incident electron, $d\sigma/dE$, were reported

by van der Wiel and coworkers (see for instance [89]) for the inelastic scattering of 10 keV electrons from various rare gases. Doubly differential cross sections (DDCS) with respect to the ejected electron energy and solid angle Ω , i.e. $d^2\sigma/dE d\Omega$, were measured by Hippler and coworkers [90,91] for the double (or multiple) ionization of rare gases under 300 eV–10 keV electron impact. Several authors [92–99] measured in coincidence pairs of electrons scattered–ejected ($e_a - e_b$) or scattered–Auger ($e_a - e_A$) issued from the same indirect double ionization process. The detected electrons were angle and energy analysed, integrating over the parameters of the unobserved electron. Therefore, one measures triply differential cross sections (TDCS), $d^3\sigma/dE_a d\Omega_a d\Omega_b$ or $d^3\sigma/dE_a d\Omega_a d\Omega_A$, with respect to one energy and two solid angles, analog to the TDCS obtained in single ionization (e,2e) experiments (see for instance [100]), or in the fully differential double photoionization experiments, (γ ,2e) [101]. Higher-order differential cross sections are investigated in an (e,3e) experiment. All three final electrons are analysed both in direction and in energy and are detected in coincidence. Hence, the quantity that is measured at a given impact energy is a fivefold differential cross section, 5DCS or $d^5\sigma/dE_a dE_b d\Omega_a d\Omega_b d\Omega_c$. Only two energies appear in the denominator since the third one is known from the energy balance. However, these experiments are technically difficult and very time-consuming. Therefore, it is also of interest to consider an alternative method to study the double ionization process [102,103] avoiding the difficulties of a triple coincidence. This is achieved by a method that can be categorized as a halfway between (e,2e) and (e,3e) experiments: An arbitrary pair of electrons, that is (e_a, e_b), (e_a, e_c), or (e_b, e_c), is detected in coincidence, while integration is performed over the solid angle of emission of the undetected one, say Ω_c . Its energy is in general also unknown since the ion final state is not defined (except for helium). That is, the energy transfer to the target, $E_0 - E_a$, is fixed from the knowledge of E_a , but the energy partitioning between the two “atomic” electrons *is not*. In other words, E_c may take any value between 0 and $E_b + E_c$. However, the measured quantity is still differential in two energies, say E_a and E_b . One therefore measures a four-fold differential cross section (4DCS), $d^4\sigma/dE_a dE_b d\Omega_a d\Omega_b$. This is a major difference with respect to (e,2e) experiments, though a double coincidence is involved. These experiments are called the e,(3-1)e experiments since three electrons are present in the final state of which only two are detected. The difference in the information content between the 5DCS and the 4DCS can be illustrated by comparing with analogous single ionization quantities obtained in electron impact experiments. The (e,3e) 5DCS and the (e,2e) TDCS are analogous in the sense that they represent the fully differential process. The 4DCS measured via integration over Ω_a (hereafter noted $\sigma_{c,b}$) are analogous to the doubly differential cross sections (DDCS) extracted from angular distributions of the ejected electron [104,105], while the 4DCS with integration over Ω_c (noted $\sigma_{a,b}$) are analogous to the DDCS extracted, for instance, from electron energy-loss spectra [106,66].

4.3. Genesis of the (e,3e) experiments

As in the (e,2e) case, the (e,3e) experiments may be subdivided into two categories depending on the kinematical parameters: structure studies and ionization dynamics studies. It is remarkable that the same group of authors at Moscow who proposed (e,2e) structure studies to “investigate the electronic states of atoms, molecules and solids by quasi-elastic knock-on of an electron by a fast electron” [108,109] have reported a decade later [110,111] an analogous proposal to “study the two-electron Fourier amplitudes of atomic and molecular wave functions using the (e,3e) processes at high energies” (see also [112,113] and the more recent review by Neudatchin et al. [114]). Both

proposals rely on the idea that at large enough incident and outgoing electrons energies, a first-order Born approximation (so-called dipolar approximation in the photo double-ionization (PDI) case) using plane waves to describe all the free electrons should be sufficient. Hence, neglecting exchange effects between the incident electron and the target bound electrons, as well as all interactions between the ejected electron(s) and the ion and between all outgoing electrons, the corresponding TDCS or 5DCS for a two-electron atom are given by

(e,2e) case:

$$\frac{d^3\sigma}{dE_a dE_b d\Omega_a} = \frac{4k_a k_b}{k_0 K^4} |\langle \Psi_f(\mathbf{r}) | e^{i\mathbf{K}\cdot\mathbf{r}} | \Psi_i(\mathbf{r}) \rangle|^2, \quad (4.2)$$

(e,3e) case [34]:

$$\frac{d^5\sigma}{dE_a dE_b d\Omega_a d\Omega_b d\Omega_c} = \frac{4k_a k_b k_c}{k_0 K^4} |\langle \Psi_f(\mathbf{r}_1, \mathbf{r}_2) | e^{i\mathbf{K}\cdot\mathbf{r}_1 + i\mathbf{K}\cdot\mathbf{r}_2} | \Psi_i(\mathbf{r}_1, \mathbf{r}_2) \rangle|^2. \quad (4.3)$$

The (e,3e) case yields the well-known dipolar approximation (dipole-length formulation) corresponding to the PDI case, when the momentum transfer K goes to zero [115]. At high enough energies and momentum transfer, the (e,2e) TDCS may be factorized such as

$$\frac{d^3\sigma}{dE_a dE_b d\Omega_a} = \frac{(2\pi)^4 k_a k_b}{k_0 K^4} |T_M|^2 |\Psi(\mathbf{p})|^2 \quad (4.4)$$

where $|T_M|^2$ is the half-off-shell electron–electron Mott scattering cross section. The structure factor, $|\Psi(\mathbf{p})|^2$, is the spherically averaged electron momentum distribution, where $\Psi(\mathbf{p})$ is the Fourier transform of the position space wave function

$$\Psi(\mathbf{p}) = \frac{1}{(2\pi)^{3/2}} \int d\mathbf{r} \Psi_i(\mathbf{r}) \exp(-i\mathbf{p}\cdot\mathbf{r}). \quad (4.5)$$

The remaining part of the right hand term of Eq. (4.4) corresponds to a kinematical factor which can readily be determined in the experiments. Therefore, a measure of the (e,2e) TDCS allows a direct mapping of the one-electron momentum density $|\Psi(\mathbf{p})|^2$. Similarly, under the same approximation of high enough energies, the matrix element in the (e,3e) 5DCS easily reduces to the double Fourier transform $\Psi(\mathbf{p}_1, \mathbf{p}_2)$ [110]

$$\Psi(\mathbf{p}_1, \mathbf{p}_2) = \frac{1}{(2\pi)^{3/2}} \int d\mathbf{r}_1 d\mathbf{r}_2 \Psi_i(\mathbf{r}_1, \mathbf{r}_2) \exp(-i\mathbf{p}_1\cdot\mathbf{r}_1 - i\mathbf{p}_2\cdot\mathbf{r}_2). \quad (4.6)$$

Therefore, the cross section measured in an (e,3e) experiment is a direct measure of the two-electron momentum density $|\Psi(\mathbf{p}_1, \mathbf{p}_2)|^2$. The importance of studying this quantity becomes clear when a two-electron system is considered. In this case, the Fourier amplitude in Eq. (4.6) is merely the wave function of the two-electron system in the momentum representation. It contains all the details of the structure of the system, and in particular the momentum distribution associated with the relative motion of electrons (i.e. in \mathbf{r}_{12} coordinate). This motion is dominated by electron–electron correlations. It is through the strong dependence on r_{12} of the (e,3e) cross section that rich and new information is expected to be obtained with a high sensitivity to the correlated motion of the electrons in the initial state of the target. In many-electron systems, if the transition $i \rightarrow f$ involves the knock-out of two electrons from the same orbital then $\Psi(\mathbf{p}_1, \mathbf{p}_2)$ characterizes the electron–electron

correlations in that orbital, whereas if the transition involves electrons from different orbitals then $\Psi(\mathbf{p}_1, \mathbf{p}_2)$ enables the study of electron–electron correlations in different orbitals. Typical experimental conditions recommended by the Moscow group correspond to 5–10 keV incident electrons which are scattered strictly forward ($\theta_a \approx 0$), and symmetrical energy distribution between outgoing ejected electrons $E_b = E_c \sim 250$ eV. Under these conditions, the predicted absolute values of the cross sections are unfortunately quite low, $\sim 10^{-5}$ a.u. or less. This has hampered the attempts of such experiments until recently when the use of multi-detection techniques in specially designed (e,3e) apparatuses [16,116,19] has opened up the way to the exploration of initial state electron–electron correlations first in magnesium [11,16] and more recently in helium [7,19] and argon [7]. Meantime, “conventional” (e,3e) experiments have been successfully performed in a different energy regime where the cross sections are larger. These experiments [1–9,36,102] have been used to investigate the dynamics of double ionization, and were mostly performed at lower ejected electron energies, 4–60 eV, where the measured absolute 5DCS are two orders of magnitude larger than given above. Yet, the coincidence signal is very low, $\sim 10^{-3}$ Hz or less, and is mostly limited by the high accidental coincidence rate generated by the dominant single ionization events. Recently, a different approach was utilized [18–20] to perform the (e,3e) experiments. This is the so-called cold target recoil ion momentum spectroscopy (COLTRIMS) where the recoil ion is detected in coincidence with two emitted electrons [cf. Fig. 4.3]. The method is highly efficient and benefits from an effective collection solid angle close to 4π . Its advantages and limitations will be discussed in the next section, in comparison with “conventional” (e,3e) methods.

4.4. Experimental techniques

The aim of this section is to discuss some aspects of coincidence experiments which are specific to the study of double ionization. For a general discussion of coincidence techniques, the reader may consult, for instance Refs. [117–119]. We have already emphasized the technical difficulty of the (e,3e) experiments, due to the very low count rates. Such limitation is almost unavoidable as it is inherent to the physical process under study, for two reasons. First, the double ionization cross section is very small. Second, and this is the worst limitation, the ratio of double ionization to single ionization cross sections is very small, $\sim 0.5\%$ in He (and $\sim 5\%$ in Ar), which means that 99.5% of all the electrons of a given energy that reach the detector belong to a single ionization event, and only contribute to the accidental coincidences. Hence the need to achieve a large luminosity for the (e,3e) spectrometers. This usually results from a compromise between count rate and one or more other experimental parameters. We will discuss how this problem was tackled by the different groups and what approach was used to make the experiments feasible. The pertinent parts of the experimental set-ups and the specificities in the data analysis methods will be described subsequently.

4.5. General description of experimental arrangements

The first (e,3e) experiments reported for Ar and Kr [102,2,4] have been performed on a modified version of an (e,2e) spectrometer [118], to which a third energy analyser and detection system were added. The luminosity problem was essentially solved by tolerating a large increase in the acceptance solid angles and energy windows. The solid angles $\Delta\Omega_b$ and $\Delta\Omega_c$ were set to $\sim 2 \times 10^{-2}$ sr which is an acceptable value as long as no sharp structure is expected in the 5DCS angular distribution,

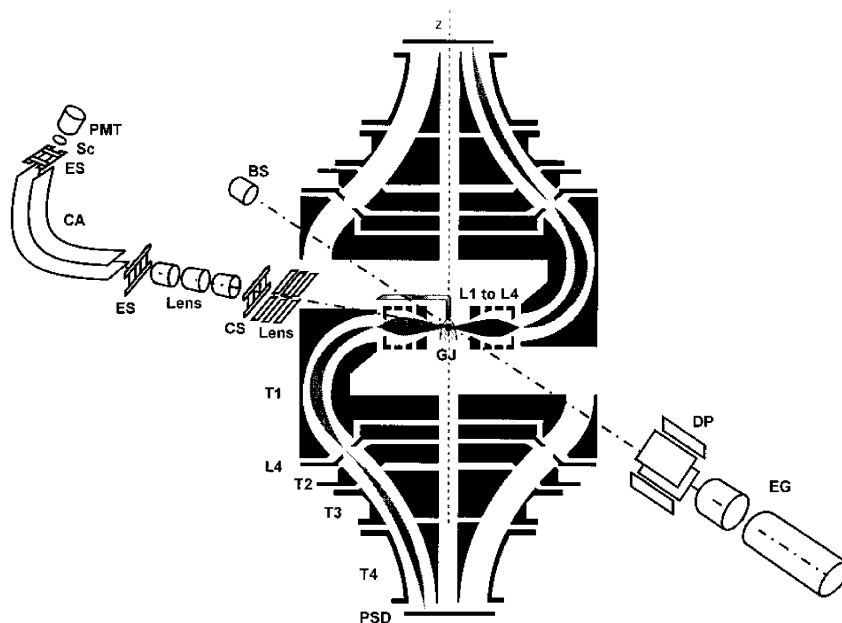


Fig. 4.2. A schematic view of the spectrometer used for the electron-impact ionization studies [(e,2e)-(e,3e)]. The electron gun (EG), deflector plates (DP), gas jet (GJ), and the beam stop (BS) are shown. The cylindrical analyzer (CA) preceded by its associated optics and followed by the scintillator (Sc) and the photomultiplier tube (PMT), the entrance and exit slits (ES) to the (CA), and the collimating slits (CS). The dual toroidal analyzers (T_1) are of cylindrical symmetry about the Z-axis. They are preceded by the entrance annular lenses, L_1 – L_4 , and followed by two three-element toroidal lenses, T_2 – T_4 . L_4 is the entrance or exit annular slits to the toroids. Electrons ejected in the x – y horizontal plane of collision are imaged as two half rings on the position sensitive detectors (PSDs) at the top and the bottom, respectively.

as is the case in the reported measurements. The energy windows, $\Delta E_a, \Delta E_b, \Delta E_c$, were fixed to 5–15 eV. This is the most serious limitation of these experiments since an effective coincidence energy resolution of a few eV would be necessary in order to distinguish between different ion final states. That is, the compromise chosen there was to increase the count rate at the expense of the final state selectivity of these experiments. There exist now two second generation (e,3e) apparatuses [120,16,116] whose common main feature is to include multi-detection techniques for the slow ejected electrons. Only the main characteristics of the Orsay (e,3e) spectrometer [Fig. 4.2] are briefly described below. More or less the same philosophy has been used by the Maryland group in the design of their (e,3e) spectrometer [16], whose two major specificities are: (I) the two ejected electrons are detected on a series of discrete detectors, in an out-of-plane arrangement, so that many triple-coincidence measurements can be carried out at the same time. (ii) a good momentum resolution is achieved, $\Delta K \sim 0.07$ a.u.. Besides these two (e,3e) spectrometers, an (e,2e+ion) COLTRIMS one is now operational [18], and will be briefly described. The Orsay apparatus [116] utilizes a crossed electron-beam gas-beam technique, and is based on the combination of three electrostatic energy analyzers, arranged in a configuration which is unique for electron impact ionization experiments. A “single channel” cylindrical analyzer is devoted to the observation of the fast scattered electron under a variable angle, θ_a . Whereas independent multi-detection of the two ejected

electrons (eventually with dissimilar energies) is realized in two twins toroidal analyzers. The ejected electrons emitted into the collision plane are detected over almost the full in-plane angular range by imaging one half-plane of emitted electrons into one toroidal analyzer, placed above the collision plane, while the other half-plane of emitted electrons is imaged into the other toroidal analyzer, which is placed below the collision plane. The detection system associated with each toroid utilizes the imaging properties of the toroids. It essentially comprises three multichannel plates (MCP) and a two-dimensional position sensitive resistive anode. One important specificity of this spectrometer is that the scattering angle θ_a is determined to a high accuracy, $\pm 0.02^\circ$, while the acceptance angle $\Delta\theta_a$ is kept reasonably small, $\pm 0.10^\circ$. This results in a high momentum transfer resolution, see below, $\Delta K = \pm 0.02$ a.u. or less. Similarly, the overall uncertainty in the ejection angles determination is $\Delta\theta_{b,c} < \sim 1^\circ$. An other essential feature of the spectrometer is its excellent long term stability. This is a crucial requirement for the (e,3e) long run experiments which may last up to 2 months! However, due to this long accumulation time and to a local, rather high non-coincident count rate on each detector assembly, the data had to be corrected in the off-line analysis for local changes in the collection efficiency of the MCPs (so-called fatigue effect). The correction typically amounts to 5–15%, and is determined by daily repeating the measurement of the same (e,2e) angular distributions, see [5,6]. These complementary (e,2e) experiments and the correction function are obtained with much better statistics than the (e,3e) ones, due to the larger single ionization cross sections. The data acquisition system is based on two identical time-to-amplitude converters (TACs), simultaneously started by the time signal from one detector (usually the a-signal), and, respectively, stopped by the b- and c-time pulses. Depending on the type of experiments which are performed, the output signals from the TACs are applied either to a logical OR gate in the case of a “double” (e,2e) experiment where both binary and recoil lobes are simultaneously measured, or to an AND gate in the case of an (e,3e) experiment. Therefore, a triple coincidence is registered if and only if the TACs are both stopped within a given time window arbitrarily set to 300 ns. Two types of e,(3-1)e experiments may also be performed. In the so-called ab-mode where the angular correlation between the fast electron and one emitted electron is measured the same experimental configuration is used as in the “double” (e,2e) experiments except for the energy balance which is adjusted to meet the double ionization requirements. In the so-called bc-mode where the angular correlation between the two “atomic” electrons is measured, the a-analyser channel is simply turned off, and only one TAC is needed to perform this quasi-(e,2e) type experiment. The TACs have a dead time of 6–7 μs , which restricts the imaging count rate in the coincidence mode to ~ 150 kHz. A more restrictive limitation is due to the long term local fatigue of the MCPs discussed above which imposes a maximum non coincident count rate < 100 kHz on each of the b- and c-channels. However, the count rate limitation is ultimately governed by the physics of an (e,3e) process. This imposes an optimum beam current, I_{opt} , which usually corresponds to single count rates on the MCPs ~ 50 kHz, and to a total (true + accidental) triple coincidence count rate $< 1 - 2c/s$, which is far below any of the dead time constraints of the electronics. The latest experimental development has come recently from the COLTRIMS technique, with the so-called “reaction microscope” [18] developed in Ullrich’s group and Schmidt-Böcking’s group in Germany. In short, a pre-cooled supersonic He jet intersects the electron beam at the collision centre. Ions and low-energy electrons produced in ionizing collisions are extracted to opposite directions by a uniform electric field, applied along the primary beam, and are detected by two position sensitive multichannel plates. An additional solenoidal magnetic field is forcing the slow electrons with non-zero transverse momenta to spiral trajectories. In this way,

Table 1

Comparison of the merits and performances of the (e,3e) multi-detection spectrometers versus the (e,2e+ion) spectrometer

	Conventional (e,3e)	COLTRIMS (e,2e+ion)
Acceptance solid angle $\frac{\Delta\Omega}{4\pi}$	Angle-multi-detection $\leq 7\%$	Angle-multi-detection $\geq 70\%$
Energy-multi-detection	Potentially	Yes
Ejected electron-energy range	Nominal $E_{ej} \pm 40\%$	$0 < E_{ej} < 30$ eV
Ejected electron-energy maximum	No max \rightarrow EMS $d^5\sigma$	max ≈ 30 eV $d^5\sigma$
Measured physical quantity	$dE_a dE_b d\Omega_a d\Omega_b d\Omega_c$	$dE_a dE_b d\Omega_a d\Omega_b d\Omega_c$
Angular resolution	High $\Delta\theta_a = 0.10^\circ$	$\Delta\theta_a \approx 3^\circ$
Momentum transfer resolution	High $\Delta K = 0.02$ a.u.	$\Delta K = 0.4$ a.u.
Ion-recoil momentum resolution	High $\Delta k_{ion} = 0.1$ a.u. All targets	$\Delta k_{ion} = 0.3$ a.u. Light targets (He, H ₂)
Complete experiments	Single or double ionization	Single or double ionization
Less differential studies	n -fold ionization (n small)	\approx any n -fold ionization
Investigated phase space region	Detailed zooms	Global view

essentially all ions, and all electrons with energies below roughly 30 eV, are detected on the PSD’s with a very large solid angle, about 70% of 4π . From the measured times-of-flight and positions on the detectors, the initial momentum vectors of all particles can be reconstructed. The experiment measures an ion and two electrons in triple coincidence, but of course it is a quasi-(e,3e) experiment, as it yields the same information.

4.6. Comparison of merits and performances

It is certainly of interest here to show a brief comparison of the merits and performances of the (e,3e) “conventional” multi-detection spectrometers versus the (e,2e+ion) spectrometer. Such comparison is summarized in Table 1. Both methods use angle-multi-detection. Main difference is that the solid angle collected in the COLTRIMS is close to 4π (with some dead zones, see [121]), whereas it is a factor of 10 or so lower in the conventional (e,3e) case and being limited to a coplanar geometry in [116], or to a series of discrete out-of-plane measurements in [16]. Besides, the multi-angle detection in conventional (e,3e) necessitates the use of several electron spectrometers in a complex arrangement, as compared to the more elegant approach in COLTRIMS where electrons and ions are “guided” to the detectors in a compact design (Fig. 4.3). A high energy and angular collection efficiency means measuring at once a large fraction of the phase space, but this should not be confused with a better quality experiment in terms of statistics. In both types of spectrometers the data are reduced during the off-line analysis to “bins” (or single data points) corresponding to small energy and angle (or momentum) intervals, δE_i and $\delta\theta_i$. If these intervals are chosen to be identical in both apparatuses, and assuming as it is the case comparable incident electron flux and target gas density, then the number of events per unit time and hence the statistics would be the same for each group of three coincident bins. The statistics can only be improved by degrading the resolution per bin, i.e. increasing δE_i and/or $\delta\theta_i$, as done in the (e,2e+ion)

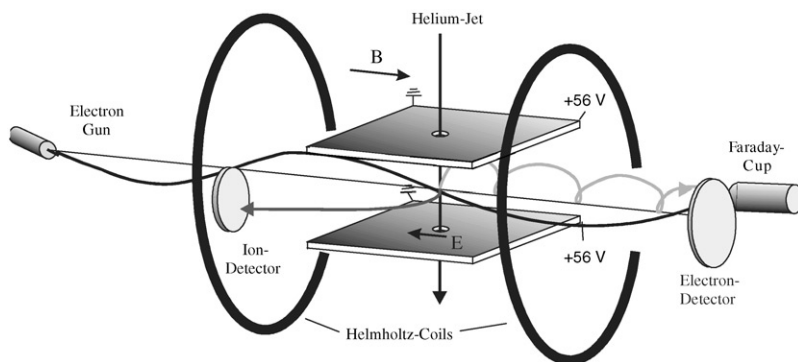


Fig. 4.3. A schematic view of the COLTRIMS apparatus as used for the $(e,3e)$ reaction.

experiments, or by accumulating over a longer period as done in the $(e,3e)$ experiments, but with the additional constraint that a long term stability of the system is needed. On the other hand, the statistics are essentially limited by the accidental coincidence rate in conventional $(e,3e)$ experiments. Whereas in COLTRIMS nine momentum components are determined, one more than necessary to completely fix the kinematics, and the redundant information obtained is used to discriminate against and hence reduce the accidental coincidences. COLTRIMS uses energy-multi-detection in the ejected energy range 0 to 30 eV, whereas such E -multi-detection does potentially exist in the $(e,3e)$ case within a range of some 30–50% of the nominal ejected energy. However, it has not so far been used. Due to the presence of the electric and magnetic fields, and to the multi-hit detection technique used, the COLTRIMS is presently limited to ejected electron energies below ~ 30 eV. No such limitation exists for the $(e,3e)$ where at least in principle any ejected energy larger than ~ 1 eV can be measured. For example, the Maryland group has reported results with 50, 100 and 200 eV energies. This is an important issue if one wants to reach the impulsive regime where electron momentum spectroscopy (EMS) can be performed. Next point is the following: both methods measure cross sections which are fully (five-fold) differential in several parameters: three in-plane and three out-of-plane angles, plus three energies. The resolution for each parameter determines the quality of the experiment, in particular how much integration is involved in the data. The high angular resolution achieved in the $(e,3e)$ case, particularly for the scattered electron, $\Delta\theta_a = 0.10^\circ$ (together with the high accuracy, $\pm 0.02^\circ$, achieved in the measurement of the actual scattering angle), result in a high momentum transfer resolution, $\Delta K = 0.02$ a.u. or less, and a high ion recoil momentum resolution, $\Delta q_r = 0.1$ a.u.. These are typical (not ultimate) numbers to be compared in the $(e,2e+\text{ion})$ case to $\Delta\theta_a = \sim 3^\circ$, $\Delta K = 0.4$ a.u. and $\Delta k_{\text{ion}} = 0.3$ a.u., respectively, [18,19]. It should be noted that the COLTRIMS method is generally capable of achieving better momentum resolution, e.g. in ion-atom collisions or in photoionization studies. The figures quoted here partly result from the necessary degradation of the resolution per bin δE_i and/or $\delta\theta_i$ in order to improve the statistics in quasi- $(e,3e)$ experiments.

Due to the need of a cold target with a small momentum spread a supersonic gas jet is needed in the COLTRIMS, so that the technique is limited (at least presently) to light targets such as He and H_2 . Whereas no such limitation occurs in the $(e,3e)$ where all targets can be envisaged, and where apart from He results have also been obtained for Ne, Ar, Kr and Mg. Nevertheless, for

the fundamental He target the conventional (e,3e) experiments are presently restricted to particular cases with relatively large cross sections such as the small momentum transfer regime. Finally, as far as complete experiments involving full determination of the kinematical parameters of all final state particles are concerned, both techniques are essentially limited to single ionization or double ionization studies where up to 3 final particles need to be detected. In addition, they can both be extended to investigate higher ionization states but on the expense of measuring less differential cross sections, that is integrating over the parameters of the undetected particles. However, in this respect these measurements should be easier to perform and less ambiguous in their output when using the COLTRIMS technique due to the measurement of the ion charge state. To summarize, one may say that the obvious advantage of the (e,2e+ion) method is to be able to simultaneously measure all ejected electrons for arbitrary energies below 20–30 eV, for arbitrary emission angles and for a large range of momentum transfer, hence giving at once a global picture of the double ionization process over almost the full final state momentum space. Whereas the (e,3e) method concentrates on a smaller region of the six-dimensional space, but in more details due to the higher momentum resolution. To give an easy analogy: COLTRIMS is analog to a high-tech camera embarked on a satellite at high altitude, for instance geostationary, taking a picture of the earth. One sees all of the Earth, that is one has in principle all the information but with a modest resolution. Whereas (e,3e) corresponds to the same high-tech camera (the same imaging techniques and the same position sensitive detectors are used), embarked for instance in a plane at lower altitude: a picture of a smaller region is taken but looking at much smaller details. Clearly, in several aspects listed above the two techniques are not competing against each other, they are rather very much complementary.

4.7. Procedure of off-line data analysis

The long run (e,3e) data, which necessitates long accumulation times (1–8 weeks) are accumulated in several successive 24h-files, sequentially separated by shorter test-runs of a well-known process (usually an outer-shell (e,2e) process). The raw data from these (e,3e) files are then concatenated in a sum-file, from which the true and accidental coincidence windows to be used in the data analysis are determined. Finally, the (x, y) images are converted to polar (r, θ) coordinates, and the total useful angular range subtended by each PSD is divided into sectors or bins whose width $\delta\theta_b$ or $\delta\theta_c$ defines the acceptance angle for each of the data points of an angular distribution. Depending on the experiment, $\delta\theta_b$ and $\delta\theta_c$ are usually $\pm 1^\circ$ to $\pm 8^\circ$.

4.8. Background coincidences subtraction and percentage statistical error

A typical three-dimensional triple coincidence time spectrum is shown in Fig. 4.4. The x and y axes of the spectrum are the arrival times of the slow b and c electrons with respect to the fast one. The peak at the center corresponds to the triple coincidence double ionization signal, superimposed on a background due to four different contributions [122,123]. One contribution is fully accidental, where the three electrons e_a , e_b and e_c are uncorrelated, hence a uniform time distribution. The other three contributions are semi-random as they are due to two correlated electrons, the third one being random, hence the shape of walls or ridges. Two of them are parallel to the time axes (e_a-e_b and e_a-e_c walls) and the third runs parallel to the diagonal (e_b-e_c wall). Each wall is widened by the resolution time of the corresponding double coincidence experiment, τ_{ab} , τ_{ac} and τ_{bc} . Note that

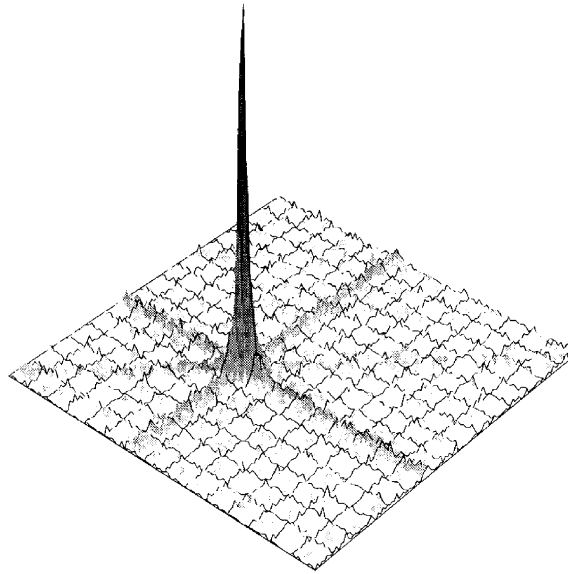


Fig. 4.4. The (e,3e) three-dimensional triple coincidence time spectrum for the double ionization of argon. The horizontal axes correspond to the arrival times t_b and t_c of the ejected electrons (e_b and e_c) with respect to the fast one. The peak at the center corresponds to the triple coincidence signal, superimposed on a uniform (random) background due to three fully uncorrelated electrons, and on three semi-random background contributions (or walls) due to two correlated electrons, the third one being random.

each of these walls is also a double ionization signal, which measures the respective e,(3-1)e cross section, but with a very low efficiency given by the probability of simultaneously finding a third electron within the 300 ns time interval corresponding to the TACs ramps. Lahmam–Bennani and coworkers [122,120] gave a detailed analysis on how to subtract the contribution of the walls and of the uniform background from the total number of counts in the peak. Formulas were derived which give the number N_T of true triple coincidences registered in the peak during the accumulation time t , and its standard deviation, σ_T . The ultimate measure of the quality of the experiment is the percentage statistical uncertainty σ_T/N_T for a given time t . Following the conclusions of Dupré et al. [122], this quantity is minimized by two different actions: (i) minimizing the coincidence resolution times, τ_{ab} , τ_{ac} and τ_{bc} , e.g. by accelerating the electrons prior to analysis, which reduces the transit time spread and hence τ ; (ii) optimizing the target gas density n_g and beam current I . Indeed, in an (e,3e) experiment, the percentage statistical uncertainty is not a monotonic function of $n_g I$ as in the (e,2e) case (see Fig. 4.3 of Ref. [120]), but first decreases for low $n_g I$ values, then passes through a minimum which determines the optimum choice for $n_g I$, and increases for larger values. This is the consequence of the additional presence of the uniform background due to three fully uncorrelated electrons, which introduces a quadratic term in the σ_T/N_T dependence over $n_g I$. The existence of this minimum strongly limits the operating conditions. In the (e,3e) experiments reported so far, it was necessary to operate at rather low $n_g I$ values ($I=1\text{--}50$ nA) to allow the coincidence signal to emerge from the accidental background. The corresponding drastic reduction in signal was compensated by a degradation of the angular and energy resolutions whose effect is to increase the signal without affecting the signal to background ratio.

4.9. Effective coincidence energy resolution

The influence on the data of the energy resolution was investigated by Lahmam–Bennani et al. [118] for the (e,2e) case and generalized by Dupré et al. [122] for the (e,3e) case. In the latter, the observed coincidence rate, f_5 , per unit time may be expressed as

$$f_5 = \sigma_5 i (\epsilon_a \Delta\Omega_a) (\epsilon_b \Delta\Omega_b) (\epsilon_c \Delta\Omega_c) \Delta E_5, \quad (4.7)$$

where σ_5 refers to the five-fold differential cross section, $\Delta\Omega_\alpha$ is the acceptance solid angle for analyser α ($\alpha = a, b$ or c), ϵ_α is the overall detection efficiency and $i = (\ln_g I/e)$ where l is the length of the collision volume. Assuming Gaussian shapes for each analyzer's individual energy transmission function, the (e,3e) effective coincidence energy resolution (ECER), ΔE_5 , was shown to be given by

$$\Delta E_5 = \frac{\Delta E_a \Delta E_b \Delta E_c}{\sqrt{\Delta E_a^2 + \Delta E_b^2 + \Delta E_c^2}}. \quad (4.8)$$

It is important to note here that this (e,3e) “energy” resolution in fact has the dimension of an energy squared, as it is also obvious from equation Eq. (4.7). Physically, this can be understood as follows: One may consider that one “energy-dimension” represents the deviation from its nominal value of the energy loss, $E_0 - E_a$, suffered by the incident electron, or alternatively of the excess kinetic energy, $E_b + E_c$, left to the two “atomic” electrons. The second one would then represent different possible partitionings of this kinetic energy. As an example, an effective energy resolution $\Delta E_5 = 16 \text{ eV}^2$ may be interpreted as being due to a sum $(E_b + E_c)$ known to within 4 eV, and a partitioning E_b versus E_c known to within another 4 eV. In the case where ΔE_a is much larger than ΔE_b and ΔE_c , Eq. (4.8) reduces to $\Delta E_a \sim \Delta E_b \Delta E_c$, which is basically independent of ΔE_a .

The (e,3-1e) case is essentially an (e,3e) experiment where one energy transmission function, say c , is infinitely wide. Setting $\Delta E_c \rightarrow \infty$ one obtains $\Delta E_4 = \Delta E_a \Delta E_b$. Obviously, any triple coincidence (e,3e) experiment has a better ECER, ΔE_5 , than the corresponding ΔE_4 of a double coincidence (e,3-1e) experiment which uses the same ΔE_a and ΔE_b .

4.10. Absolute scale determination

Most of the (e,3e) experiments reported by Lahmam–Bennani's group at several keV impact energy have been assigned an absolute scale for the cross sections, with an accuracy of about 10% to 30%. This is a very important issue in comparison with theory. Indeed, data obtained only on a relative scale cannot distinguish between different theoretical models which predict about the same shape for the angular distributions but might differ in intensity by very large factors, e.g. see [36]. Part of the sensitivity of the (e,3e) angular distributions to the electron correlations would then be lost. Therefore, before discussing the results, we briefly present the method of absolute scale determination. This method [2,5] relies on Eq. (4.7), and requires knowledge of all quantities therein appearing. Of these, only f_5 and I are directly measurable. The other quantities can, however, be determined as follows, using known double differential cross sections (DDCS), or alternatively elastic cross sections (ECS), and known (e,2e) triple differential cross sections (TDCS) for single ionization, all measured under the same experimental conditions (i.e. beam current, target density, analyzers settings: detected electrons energies, efficiencies, solid angles, ...) as in the (e,3e) experiments.

We illustrate this point on the simple case of a He target. First, the product $(\epsilon_a \Delta\Omega_a)$ is determined by measuring the DDCS, noted σ_a , given by

$$f_a = \sigma_a i(\Delta\Omega_a) \Delta E_a, \quad (4.9)$$

where f_a is the a-analyzer single count-rate. ΔE_a is determined from the width of the elastic peak, while the DDCS σ_a is obtained for instance from tabulated Compton profiles [124]. Then, the quantities $(\epsilon_b \Delta\Omega_b)$ and $(\epsilon_c \Delta\Omega_c)$ are determined by measuring (e,2e) TDCS's for He and comparing them with first-Born theoretical TDCS's, such as the orthogonalized Coulomb wave (OCW) model or the convergent close coupling (CCC) model, which have been widely proved to very well reproduce the measured TDCS in the keV regime, at least for He on the binary lobe (see e.g. [100,125], respectively). Finally, the effective coincidence energy resolution, ΔE_5 , as defined in Eq. (4.8), is straightforwardly obtained from the measurement of the individual resolutions, ΔE_a , ΔE_b and ΔE_c .

5. Comparative analysis of the experimental and the numerical results: Helium

The analysis and comparison of the experimental and theoretical cross sections is done in two steps. At first, we focus on fully resolved cross sections and analyse the experimental and theoretical results as to reveal the underlying mechanisms of the electron-impact double ionization. In the next step we consider integrated cross sections and point out which information can be extracted from these quantities. In most cases we consider a helium atom as a target. This target is of a special interest since the residual ion in the final state has no relevant structure, as far as (e,3e) is considered. Hence in the final channel a “pure” four-body problem is achieved (which is reduced to a three-body one in the perturbative regime).

5.1. Fully resolved cross sections for the electron-impact double ionization

Over the last decade a number of experimental and theoretical studies on (e,3e) from He($1S^e$) have been conducted. For the analysis and the understanding of the complicated structure of the results of these studies it is imperative to single out the features in the cross sections which are purely related to the symmetry of either the initial bound state or/and to the properties of the transition operator.

5.1.1. Selection rules for the (e,3e) in the perturbative regime

Most of the (e,3e) experiments have been performed within the perturbative regime (whose range has been specified in Section 2.3). In this case the problem is reduced to the description of a correlated three-body system (the two slow electrons and the residual ion) and a uniform motion of the scattered projectile. The symmetry properties of the correlated three-body function $\psi_{\mathbf{k}_b, \mathbf{k}_c}^-(\mathbf{r}_b, \mathbf{r}_c)$ follow directly from the symmetry features of the Schrödinger equation (3.1), e.g.

$$\psi_{\mathbf{k}_b, \mathbf{k}_c}^-(\mathbf{r}_b, \mathbf{r}_c) = \psi_{\mathbf{k}_c, \mathbf{k}_b}^-(\mathbf{r}_c, \mathbf{r}_b), \quad (5.1)$$

$$\psi_{\mathbf{k}_b, \mathbf{k}_c}^-(\mathbf{r}_b, \mathbf{r}_c) = \psi_{-\mathbf{k}_b, -\mathbf{k}_c}^-(-\mathbf{r}_b, -\mathbf{r}_c). \quad (5.2)$$

Furthermore, since the He ground state is a singlet, its spatial wave function has to be invariant under exchange of the two electrons. The FBA transition operator (i.e. the operator $\exp(i\mathbf{K} \cdot \mathbf{r}_b) + \exp(i\mathbf{K} \cdot \mathbf{r}_c) - 2$ occurring in Eqs. (2.48)–(2.50)) is also symmetric under exchange of the two ejected

electrons. Therefore, the three-body final state has to satisfy

$$\psi_{\mathbf{k}_b, \mathbf{k}_c}^-(\mathbf{r}_b, \mathbf{r}_c) = \psi_{\mathbf{k}_b, \mathbf{k}_c}^-(\mathbf{r}_c, \mathbf{r}_b) = \psi_{\mathbf{k}_c, \mathbf{k}_b}^-(\mathbf{r}_b, \mathbf{r}_c) . \quad (5.3)$$

From the symmetry relations (5.1)–(5.3) one can derive [35] several selection rules that are independent of the approximations made to arrive at an approximate expression for the wave function $\psi_{\mathbf{k}_b, \mathbf{k}_c}^-(\mathbf{r}_b, \mathbf{r}_c)$ or/and for the transition matrix elements. For a formal derivation of these rules we assume that the three-body initial and the final-state wave functions $\varphi(\mathbf{r}_a, \mathbf{r}_b)$ and $\psi_{\mathbf{k}_a, \mathbf{k}_b}^-(\mathbf{r}_a, \mathbf{r}_b)$ are known exact. In the perturbative regime the total transition matrix elements \mathcal{T}_{fi} can be written as (cf. Eqs. (2.48)–(2.50))

$$\begin{aligned} \mathcal{T}_{fi} \propto & \langle \psi_{\mathbf{k}_b, \mathbf{k}_c}^-(\mathbf{r}_b, \mathbf{r}_c) | \cos(\mathbf{K} \cdot \mathbf{r}_b) + \cos(\mathbf{K} \cdot \mathbf{r}_c) | \varphi(\mathbf{r}_b, \mathbf{r}_c) \rangle \\ & + i \langle \psi_{\mathbf{k}_b, \mathbf{k}_c}^-(\mathbf{r}_b, \mathbf{r}_c) | \sin(\mathbf{K} \cdot \mathbf{r}_b) + \sin(\mathbf{K} \cdot \mathbf{r}_c) | \varphi(\mathbf{r}_b, \mathbf{r}_c) \rangle . \end{aligned} \quad (5.4)$$

From the structure of this equation for the transition amplitude we deduce that the following minima should appear in the cross sections:

- (a) In the case $\mathbf{k}_b = -\mathbf{k}_c$ the exact wave function $\psi_{\mathbf{k}_b, \mathbf{k}_c}^-(\mathbf{r}_b, \mathbf{r}_c)$ has an *even* parity as can be seen immediately from Eq. (5.3) and (5.1) when rewriting $\psi_{\mathbf{k}_b, \mathbf{k}_c}^-(\mathbf{r}_b, \mathbf{r}_c)$ in the form

$$\begin{aligned} \psi_{\mathbf{k}_b, \mathbf{k}_c}^-(\mathbf{r}_b, \mathbf{r}_c) &= \frac{1}{2} [\psi_{\mathbf{k}_b, \mathbf{k}_c}^-(\mathbf{r}_b, \mathbf{r}_c) + \psi_{-\mathbf{k}_c, -\mathbf{k}_b}^-(\mathbf{r}_b, \mathbf{r}_c)] \Rightarrow \\ \psi_{\mathbf{k}_b, -\mathbf{k}_b}^-(\mathbf{r}_b, \mathbf{r}_c) &= \frac{1}{2} [\psi_{\mathbf{k}_b, -\mathbf{k}_b}^-(\mathbf{r}_b, \mathbf{r}_c) + \psi_{\mathbf{k}_b, -\mathbf{k}_b}^-(\mathbf{r}_b, \mathbf{r}_c)] = \psi_{\mathbf{k}_b, -\mathbf{k}_b}^-(\mathbf{r}_b, \mathbf{r}_c) . \end{aligned} \quad (5.5)$$

Therefore, the second term in Eq. (5.4) vanishes for $\mathbf{k}_c = -\mathbf{k}_b$ and the first non-vanishing term in Eq. (5.4) is proportional to K^2 . Only terms proportional to K^{2n} and $n = \text{integer}$ do contribute to the measured cross sections. Hence, for a fixed \mathbf{k}_b and a small but fixed momentum transfer K a minimum occurs at $\mathbf{k}_c = -\mathbf{k}_b$ in the cross section when it is considered as a function of \mathbf{k}_c . The same applies when the role of the two ejected electrons is interchanged.

- (b) In the case of very high energies of the ejected electrons the position vectors of the ionized electrons $\mathbf{r}_c, \mathbf{r}_b$ are almost in the directions $\mathbf{k}_c, \mathbf{k}_b$. In this situation and for a fixed K a zero point in the angular distribution of ejected electrons is observed whenever $\mathbf{k}_c \perp \mathbf{K}$ and $\mathbf{k}_b \perp \mathbf{K}$. In general, this zero point turns into a minimum at moderate energies.
- (c) The momentum distribution of the ionized electrons possesses a zero point at $\mathbf{k}_c = \mathbf{k}_b$ due to the electron–electron repulsion.
- (d) In addition, a minimum appears if $(\mathbf{k}_b + \mathbf{k}_c) \perp \mathbf{K}$ since the optical transition is forbidden in this case (cf. Refs. [126,101] and references therein).

All the minima listed above turn to zero points for optical transitions [126–128,101].

5.1.2. Numerical and experimental results

To contrast the positions of the minima predicted by the symmetry analysis with the experimental findings we scan the angular distributions of one of the electrons say electron b while the other ejected electron is detected under a fixed angle θ_c (cf. Fig. 4.1).

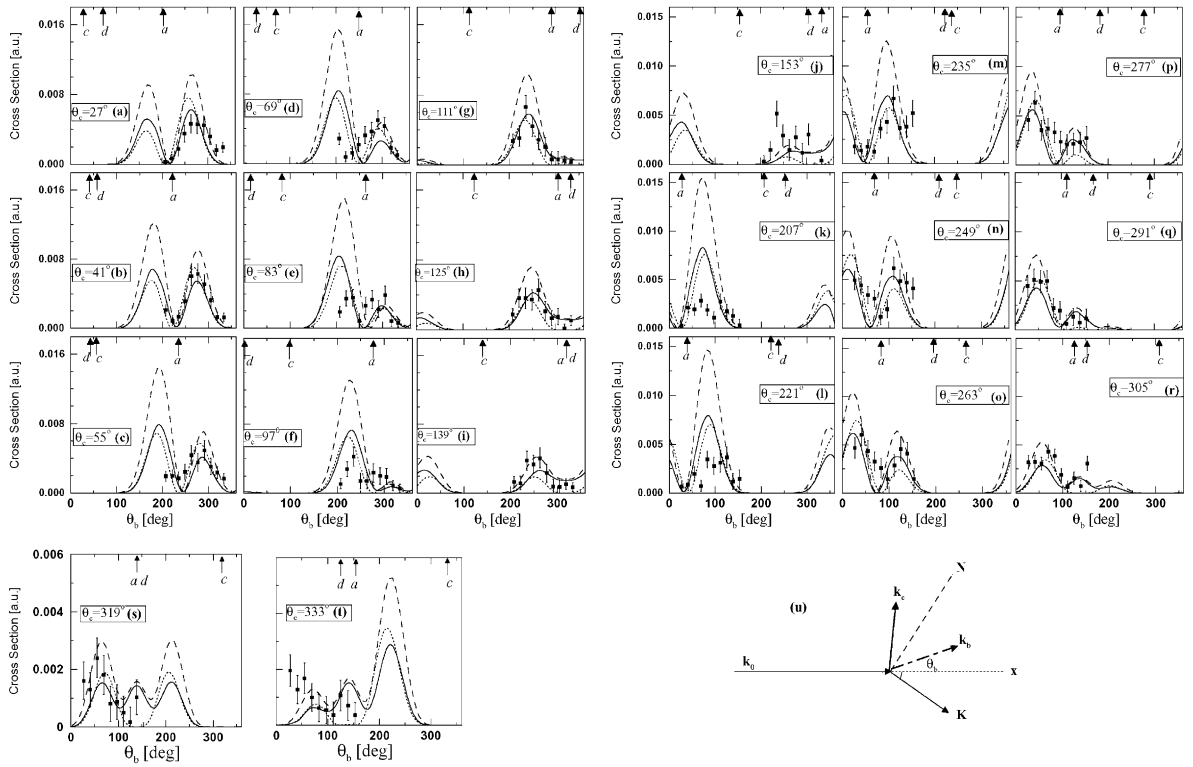


Fig. 5.1. The measured and calculated absolute (e,3e) fivefold differential cross section for helium. The scattering angle of the fast electron is fixed $\theta_a = +0.45^\circ$. The incident energy is 5.6 keV. The ejected electrons are detected with equal energies $E_b = E_c = 10$ eV. The angular distribution of one of the electrons (electron b) is scanned while the other ejected electron is detected under a fixed angle θ_c . The angle θ_c is indicated on the figures. The arrows labeled a, c, d mark the angular positions of, respectively, the minima (a), (c), (d) as specified in the text. The geometrical arrangement for the minimum (d) is illustrated in (u). The normal to \mathbf{K} is denoted by \mathbf{N} . The momentum transfer vector \mathbf{K} is indicated. Using in the calculations the wave functions Eq. (3.39) and (5.6) lead to the results shown as solid curves. The dotted curves represent the cross sections in the optical limit (2.52). The solid and dotted curves have been scaled down by a factor 10 for comparison. The dashed curve is the result for the (e,3e) cross section when employing (3.39) and a Slater-type initial state to evaluate the cross sections.

The positions of the minima listed above are indicated by arrows labeled a, b, c, d corresponding to the minima (a)–(d).

As clear from Eqs. (2.48)–(2.50), a representation of the (singlet) ground state of the helium atom is required. For this purpose we employ a Hylleraas-type wave function of the form

$$\varphi(\mathbf{r}_b, \mathbf{r}_c) \approx N \{ \exp[-C_c r_c - C_b r_b] + \exp[-C_b r_c - C_c r_b] \} \exp[C_{cb} |\mathbf{r}_c - \mathbf{r}_b|], \quad (5.6)$$

where N is a normalization factor and C_c , C_b and C_{cb} are positive real numbers used to minimize the binding energy of $\text{He}(^1S^e)$. If we set $C_c \equiv C_b$ and $C_{cb} \equiv 0$ we retrieve a Slater-type wave function. For the results depicted in Figs. 5.1(a)–(t) we used the C4FS model, as described in Section 3.3.3.

The general trends and *shapes* of the angular distributions are reproduced satisfactorily by the theory. Different representations of the initial state do not affect the angular shape, however, the

magnitudes of the cross sections are strongly dependent on the initial state description. Furthermore, we observe substantial differences in absolute values of the theoretical and experimental cross sections. Similar behavior has also been noted for the case of one photon two-electron ionization [cf. Ref. [101] and references therein]. One of the underlying reason for this trend is that the selection rules introduced above are applicable to any treatment of the process, regardless of the approximations employed for the description of the scattering dynamics. On the other hand, these selection rules determines the basic pattern of the electrons' angular correlation (cf. discussion below), but they do not influence the over-all magnitude of the cross sections.

It is worthwhile to remark that the (e,3e) cross sections shown in Figs. 5.1(f)–(t) reveal some deviations from the optical limit, i.e. from the theoretical calculations with only the first term in Eq. (2.52). Generally however the optical limit seems to be reached in this geometry (and within the present model). The deviations from the optical limits have two generic sources: (1) Considerable contributions from higher multipoles in the Born amplitude (i.e., multipoles other than the leading order dipolar term). These contributions are usually called the non-dipolar contributions; or (2) contributions from higher terms in the Born series which do not connect to optical transitions.

To analyze in detail the origin of the features in the cross sections as θ_c is changed from the situations in Fig. 5.1(a) to that of Fig. 5.1(t), we recall the angular positions of the minima **a, b, c, d** (these are zero points for photon impact):

- (a) $k_b \cos \theta_b = -k_c \cos \theta_c$,
- (b) $k_0 \cos \theta_b - k_a \hat{\mathbf{k}}_a \cdot \hat{\mathbf{k}}_b = 0$ and $k_0 \cos \theta_c - k_a \hat{\mathbf{k}}_a \cdot \hat{\mathbf{k}}_c = 0$,
- (c) $k_c \cos \theta_c = k_b \cos \theta_b$,
- (d) $k_b(k_0 \cos \theta_b - k_a \hat{\mathbf{k}}_a \cdot \hat{\mathbf{k}}_b) = -k_c(k_0 \cos \theta_c - k_a \hat{\mathbf{k}}_a \cdot \hat{\mathbf{k}}_c)$.

The angular position of the minimum (**d**) seems complicated and therefore we included in Fig. 5.1(u) as schematic illustration. We note that in our present case we choose $E_b = E_c$. Thus, the vectors \mathbf{k}_b and \mathbf{k}_c have to be positioned symmetrically with respect to an axis normal to $\hat{\mathbf{K}}$ (axis *N* in Fig. 5.1(u)).

In Figs. 5.1(a)–(t) we indicated by arrows the positions of the minima predicted above (the label on the arrow correspond to the number of the minimum). Following the behavior of the cross sections as the positions of the minima (a)–(d) vary, it become clear that these minima are the determining factor of the shape of the electrons' angular correlations. [exemption are noticed when the (e,3e) cross sections differ substantially from the photo-ionization cross sections (cf. Figs. 5.1(f)–(t))]. The characteristic two-lobe structure is due to the fact that when $E_b = E_c$ the photo-ionization cross sections has the symmetry features: (i) For $\hat{\mathbf{k}}_c = \pm \hat{\mathbf{K}}$ (i.e. for $\theta_c \approx 139^\circ$ and for $\theta_c = 319^\circ$), the angular distribution, as depicted in Figs. 5.1(a)–(t) must be cylindrically symmetric with respect to $\hat{\mathbf{K}}$. This is the case in Figs. 5.1(i),(s). (ii) For $\hat{\mathbf{K}} \cdot \hat{\mathbf{k}}_c = 0$, (i.e. for $\theta_c \approx 49^\circ$ and for $\theta_c \approx 229^\circ$) the angular distribution of electron *b* possess reflection symmetry with respect to an axis normal to $\hat{\mathbf{K}}$ (this is due to the fact that the polarization vector for linearly polarized photon enters bi-linearly in the photo-ionization cross section, i.e. it defines an axis rather than a vector). This condition is approximately reached in Figs. 5.1(b), (c), (l), (m).

Thus, combining these symmetry properties and the positions of the minima imposed by the symmetry selection rules (a)–(d) we conclude that the angular distributions can have an angular pattern with three lobes. The three-lobe case is clearly observed in Fig. 5.1(q).

Above we argued that the two lobes in Figs. 5.1(i),(s) and Figs. 5.1(b), (c), (m), (l) have to be of approximately the same magnitudes due to the requirements (i) and (ii). The diminishing size of the lobe located around $\theta_b > 300^\circ$ in the intermediate cases depicted in Figs. 5.1(c)–(h) occurs because the minimum (**d**) passes through this lobe. Same observations and interpretations apply to Figs. 5.1(j)–(t). The seemingly complicated behavior of the ratio of the magnitudes of the two dominant lobes in Figs. 5.1 can be fully explained by tracing the position of the minimum (**d**) as θ_c varies.

While the overall structure of the angular correlation can be explained by the rules (a)–(d) which are most effective in the regime of the optical limit, a more detailed analysis, in particular of Figs. 5.1(f)–(t), reveals considerable deviations from the anticipations made on the basis of the rules (a)–(d). E.g. the minima (**a**, **d**) are not present in the (e,3e) cross sections. These deviations seem to be supported by the experimental results. As mentioned above deviations of this kind may arise due to the contributions of higher-order multipoles in expansion (2.52) or from second or higher-order terms in the Born series contribution. The former contributions are distinguishable from the latter in that all FBA terms (dipolar and non-dipolar) have to show the typical FBA cylindrical symmetry with respect to **K**. The calculations depicted in Figs. 5.1 show the FBA cylindrical symmetry so that the deviations of the (e,3e) cross sections from the optical cross sections can be assigned to higher-order multipoles in the FBA transition amplitudes. For a fixed K (as is the case for Fig. 5.1) the contributions of these multipoles to (2.52) depend not only on K but also dynamically on \mathbf{k}_b and \mathbf{k}_c . This is the reason why, for a fixed K , approaching the optical limit is very much dependent on the geometrical arrangement of \mathbf{k}_b and \mathbf{k}_c . Clearly, with diminishing K the contributions of the higher order multipoles are suppressed.

So far we discussed the occurrence of minima in the (e,3e) cross sections. Naturally the region between two minima will be a maximum. Apart from this obvious statement one can expect the appearance of peaks in the cross section from some general arguments. In Section 2.2 we discussed a possible way to do that by pointing out that peaks should appear in the cross sections due to a certain sequence of double ionization processes. The footprints of these mechanisms will be unravelled below by analyzing further experimental and theoretical data. Another idea [35] to determine the positions of peaks in the (e,3e) cross section is based on an analogy to single ionization cross section [(e,2e)]: For the (e,2e) reaction and in the region of validity of the FBA one expects a dominant peak when the projectile knocks out directly the bound electrons. This peak is called the binary peak [65] and it appears at the direction of the momentum transfer vector **K**. The binary peak is associated with a minimal momentum transfer to the ion. A further peak, called the recoil peak, occurs in the opposite direction to the **K**. For the (e,3e) reaction one imposes thus the condition that the recoil momentum of the ion should be minimal and determines thus the positions of the momentum vectors of the two ejected electrons. This has been done in Ref. [35]. It turned out that the positions of the “binary” peak are located on a sphere, the so-called the Bethe sphere Ref. [35]. It should be stressed that the determination of the (e,3e) binary peak does not imply any specific mechanisms for the (e,3e) process (except for the energy and momentum conservation laws). In fact various double ionization pathways may occur on the Bethe sphere, as explicitly demonstrated in Ref. [35].

For the case of Fig. 5.1 it has been shown in Ref. [3] that the (e,3e) cross section near the Bethe-sphere (where a peak is expected) is suppressed by the minima **a** – **d** which seems to have higher priority than the Bethe-sphere maxima. However, if those restrictive minima are released, for

reasons of geometry and/or not approaching the optical limit, the maxima due to the Bethe-sphere condition show up.

Further evidence for the existence of the selection rules **(a)**–**(d)** and for the appearance of peak structures associated with double ionization mechanisms comes from recent COLTRIMS experiments [18–20]. In these experiments the fast projectile electron has an energy $E_0=2$ keV and the two ejected electrons escape with low final state kinetic energies ($E_b, E_c < 30$ eV). Thus one may expect the FBA to be valid and exchange processes between the projectile electron and the slow electrons can be neglected. The cross sections are presented in the angle scanning mode: For a given momentum transfer and for fixed energies of the ejected electrons the cross section is plotted as a function of the ejected electrons emission angles. This allows a direct comparison with data presented in Fig. 5.1. Here we would like however to exploit the strength of COLTRIMS in giving a global view on the cross sections in order to highlight the dominant double ionization mechanisms. The momentum transfer is fairly large $K = 2 \pm 0.4$ a.u., i.e. we are far off the optical limit. While the validity of the FBA and the optical limit may be questioned in this regime, the double ionization mechanisms as discussed in Section 2.2.1 are still valid (this is no more the case when E_0 is comparable to the double ionization energy). For the experiment discussed here the relevant reaction mechanisms and the corresponding matrix elements are: the shake-off (SO), the two-step 1 (TS1) and the two-step 2 (TS2) processes. We recall that in the shake-off process only one target electron acquires its momentum upon a direct ionizing collision with the projectile and is emitted into the direction of K . The second (slow) electron is “shaken” into the continuum, i.e. it is emitted due to the subsequent relaxation of the singly charged ionic core. The emission characteristic of this low-energy electron is intimately related to the spatial distribution of the electronic charge from which it is shaken off, for He it is isotropic, i.e. in this case the electron should not be emitted into a particular direction. Its energetic position is as well determined by the initial momentum distribution (Compton profile) which sets a limit on the momentum of the shake-off electrons. The recoiling ion balances the momentum of the shake-off electron [cf. Eq. (2.1)]. As discussed in Section 2.2.1 the TS1 process means that the incident electron scatters from one target electron that in turn, on its way out into the vacuum, collides from the second electron leaving the atom target doubly ionized (cf. Fig. 2.2). From this picture it is clear the residual ion should have a small recoil momentum. As shown in (cf. Fig. 2.2), if the two electrons as are fast they escape upon a TS1 process perpendicular to each others. As pointed out in Section 2.2.1, both processes (SO) and (TS1) are of a first order in the projectile-target interaction and possess hence the typical FBA axial symmetry with respect to K . In contrast, the TS2 is a second order scattering process in which the projectile interacts and ejects into the continuum the two target electrons sequentially (cf. Fig. 2.1). A signature of a second- or higher-order processes is a break of the FBA axial symmetry of the cross section with respect to K . We recall however the statement of Section 2.2.1 that the double ionization mechanisms have their origin in quantum mechanical transition amplitudes which may interfere if they have an appreciable contribution and are of roughly the same order in magnitudes. In addition, the positions for the appearance of the peaks have been determined purely on the ground of kinematical considerations. Dynamical aspects, such as final-state interactions have not been taken into account and may well lead to serious modification of the cross sections. These precautions are valid in the low velocity regime of the continuum particles and become less important for swift electrons.

At first we discuss the (e,3e) COLTRIMS cross sections in the coplanar scattering geometry as illustrated in Fig. 4.1, i.e. when both target electrons are ejected in the scattering plane defined by the

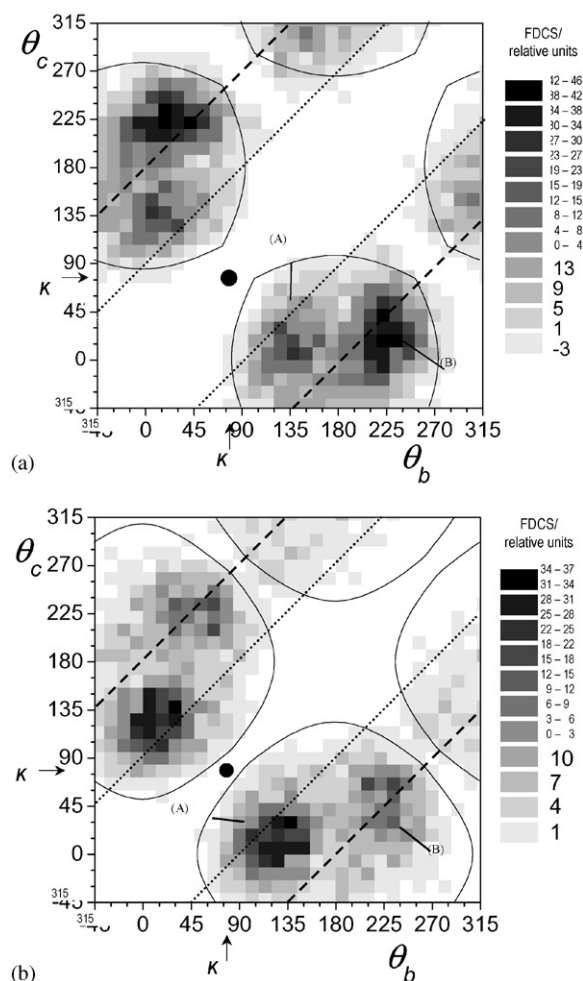


Fig. 5.2. Fivefold differential cross sections (FDCS) for the $(e,3e)$ reaction using a He target. The incident energy is $E_0 = 2$ keV. The momentum transfer vector \mathbf{K} ($K = 2$ a.u.) is marked by an arrow and by the solid circle in the diagram. The experiment is performed in the coplanar scattering geometry see 4.1. The dashed lines on the figures mark the angular combinations for which the relative electron emission angle is $|\theta_b - \theta_c| = 180^\circ$ and dotted lines mark relative angles $|\theta_b - \theta_c| = 90^\circ$. The angular range inside the solid circular lines is not affected by the detector dead time. (a) Shows the experimental cross section for $E_b = E_c = 5$ eV whereas in (b) $E_b = E_c = 20$ eV.

incoming and scattered projectile. In Fig. 5.2(a) the data for equal-energy electrons ($E_b = E_c = 5$ eV) are shown in a density plot representations of the cross sections in a substantial angular range of θ_b and θ_c . The angular range is limited by the electron detectors dead-time. The region which is not affected by this limitation is marked to be inside the circular solid line. The cross sections in Fig. 5.2(a) reveal four maxima: The two in the lower right part have to be equivalent to those in the upper left part. This is because for $E_b = E_c$ an interchange of $\theta_b = \theta_c$ means an interchange of the two electrons and therefore such an operation should leave the cross sections invariant. For photo-double ionization ($\gamma, 2e$) one observes the same structure of four-maxima in the cross sections however the minima between these maxima turn into regions of vanishing intensity. The origin

of these structures lies in the rules (a)–(d), as discussed above. As explained previously, for the $(\gamma, 2e)$ reaction all four peaks must have the same shape and the same magnitude, since the linear polarization vector defines only an axis but no direction. The positions of these peaks correspond to both electrons being ejected at $\sim 60^\circ$ with respect to the direction of the polarization vector. The electron–electron relative angle is $|\theta_b - \theta_c| \approx 120^\circ$. As discussed above, in the case of $(e, 3e)$ there is no forward–backward symmetry with respect to \mathbf{K} and hence the four “hills” need not be of the same height and shape [as for $(\gamma, 2e)$].

When the momentum transfer becomes considerable ($K = 2$ a.u. here) a different emission pattern emerged: The cross section maximum [marked (B) in Fig. 5.2] correspond to a configuration where one electron is emitted roughly along \mathbf{K} whereas the second electron is emitted along $-\mathbf{K}$, i.e. the two slow electrons recede from the residual ion in back-to-back configuration [18–20].

The two other peaks marked (A) have a lower magnitude and correspond to a situation where both electrons are enclosing $\sim 60^\circ$ with the momentum transfer direction \mathbf{K} and having a relative angle of $|\theta_b - \theta_c| \approx 120^\circ$. This basic angular shape is retained for different energies of the electrons but the relative intensities of the peaks are strongly dependent on E_b and E_c : If $E_b = E_c = 20$ eV (Fig. 5.2(b)) the back-to-back emission [peaks (B)] becomes relatively unimportant compared to emission of both target electrons into the half-plane of the momentum transfer [peaks (A)].

Fig. 5.3 shows the theoretical cross sections evaluated within the CCC method that has been discussed in Section 3.2.2. The interaction of the fast projectile with the target is described within the FBA while the interaction of the slow ejected electrons is treated non-perturbatively. The helium ground state is described by a 20 parameters Hylleraas wave function. The calculations describe well the experimental findings with regard to the observed cross section patterns and the evolution of the relative peak intensities is also correctly predicted. The absolute magnitudes of the cross sections are not determined experimentally. However, in Figs. 5.2, 5.3 one observe some deviations of the theory from the experimental data: the positions of the calculated peaks (B) are shifted with respect to what is found experimentally. The CCC results which are performed within the FBA and therefore possess a complete axial symmetry with respect to the momentum transfer direction \mathbf{K} . That is the reason for the invariance of the CCC cross sections under reflection of both electrons’ momentum vectors with respect to K . In the experiments however [Figs. 5.2] this FBA axial symmetry is broken: according to FBA symmetry the peak (B) has to appear when one electron is emitted along \mathbf{K} and the other is ejected along $-\mathbf{K}$. Experimentally one observes a shift along the dashed diagonal line of this peak’s position to smaller angles. As pointed out in the preceding discussion a description of such effects requires the calculations of higher-order terms in the Born series.

The origin of the peaks (A) can be attributed to the TS1 process [18–20]. This is concluded from the observation that the relative electrons’ emission angles is $\sim 90^\circ$ and from the fact that the recoil ion momentum is small [cf. Fig. 2.2].

In Fig. 5.4 (e,3e) COLTRIMS results are displayed for a different kind of scattering geometry, namely for a non-coplanar scattering geometry: As schematically shown in Fig. 5.4 in the experiment one electron is detected under 45° above the scattering plane ($\phi_b = 45^\circ$) and the second emerges 45° below the scattering plane ($\phi_b = 135^\circ$). The electrons’ energies are $E_b = E_c = 20$ eV [18–20]. Also shown in Fig. 5.4 are the theoretical CCC results which agree well with the experimental findings. For the case of Fig. 5.4 the electrons momentum sum vector $\mathbf{k}_b + \mathbf{k}_c$ is always in the scattering plane and lies parallel to \mathbf{K} , if \mathbf{K} is in the plane spanned by \mathbf{k}_b and \mathbf{k}_c . This is the case along the dashed line in Figs. 5.4 where the two binary peaks in the cross sections are observed. The

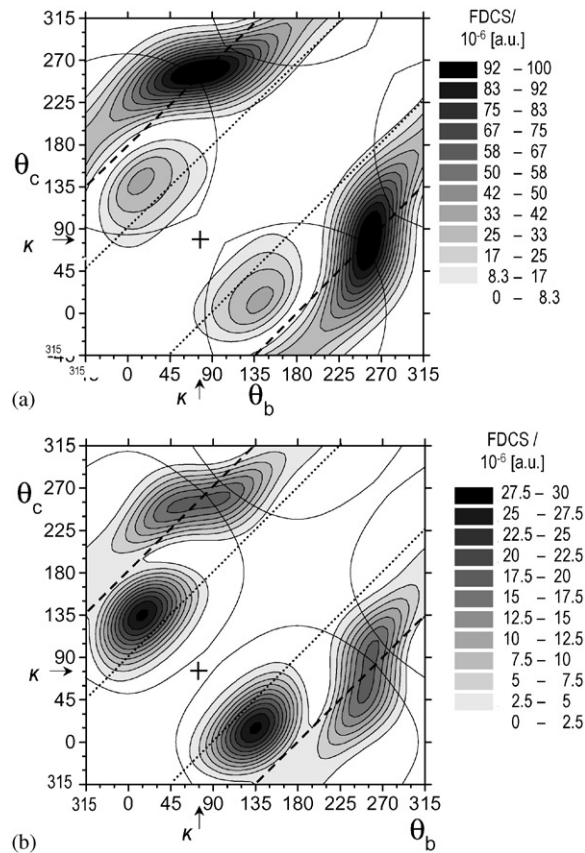


Fig. 5.3. The calculated FDCS for the same conditions as in Fig. 5.2 using the convergent close-coupling method (CCC) for the treatment of the interaction of the slow ejected electrons non-perturbatively while the projectile electron moves freely in the initial and final state. The experimentally accessible angular range is indicated and lies within the solid circular lines. (a) Shows the theoretical results for $E_b = E_c = 5$ eV and in (b) the (e,3e) theoretical cross sections for $E_b = E_c = 20$ eV are depicted.

recoil ion momentum k_{ion} is minimal if $\theta_b = \theta_c = \theta_q$ [cf. scattering geometry depicted in Fig. 5.4]. Unfortunately, this angular region is not accessible experimentally due to detector dead-time but the theory indicates a substantial cross section there (position is marked by a dot) as a consequence of the reduced repulsion of the slow-electrons (compared to the coplanar geometry).

5.1.3. Beyond the first-Born approximation

In our discussion of the (e,3e) theoretical and experimental results we assigned certain discrepancies between theory and experiments to the contributions of terms beyond the first-order Born approximation. Theories that account for such terms have been reported only recently [86,40,84]. Likewise, experiments that are exclusively devoted to such features are very recent [10]. One of the non-perturbative methods is the Green-function approach that has been sketched in Section 3.3.4. Signatures of the non-FBA terms are the break of the axial symmetry with respect to \mathbf{K} . In addition, within the FBA the cross section does not depend on the charge of the projectile. Therefore, we

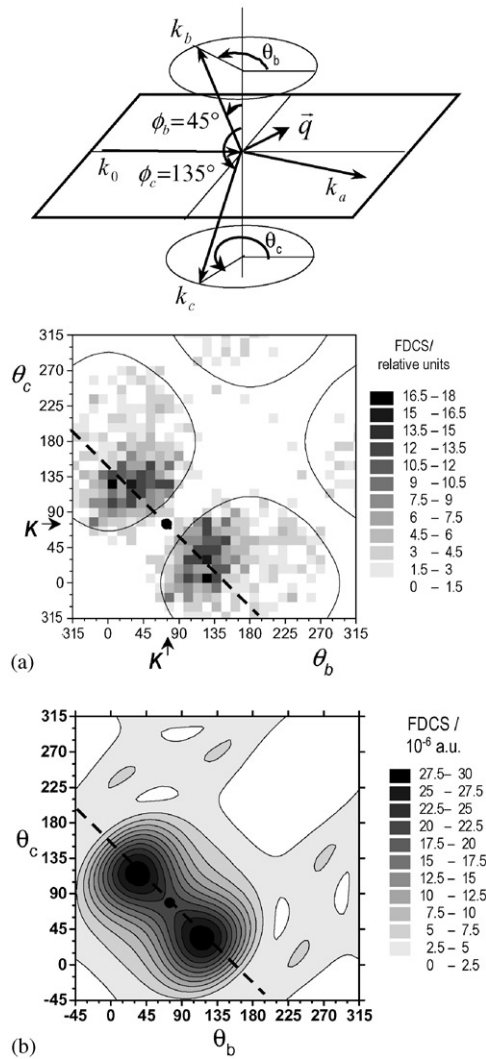


Fig. 5.4. The fivefold differential cross section for the out-of-plane geometry as shown schematically in the upper drawing. In (a) the experimental results are shown for a momentum transfer $K = 2 \pm 0.4$ a.u. and the electrons' energies are $E_b = E_c = 20$ eV. In (b) the results of the CCC theory are depicted. The dashed lines mark angular combinations for which the electron momentum sum is parallel to the momentum transfer direction.

consider in Figs. 5.5 the results for the electron and the positron impact double ionization of an atomic helium target in the ground state along with the experimental data [3] and a full numerical evaluation of the first Born term within a convergent close coupling (CCC) method [36] (cf. Section 3.2.2). The FBA corresponds to one term in the GF expansion Eq. (3.47) where the (uniform) projectile motion is decoupled from the rest of the system. The GF results show clear difference between using positrons or electrons as a projectiles (the FBA results are insensitive to the projectile charge). Above we explained at length the origin of the main peaks in the FBA spectrum. Thus let us focus our attention on the additional structures predicted by the GF theory. From the level

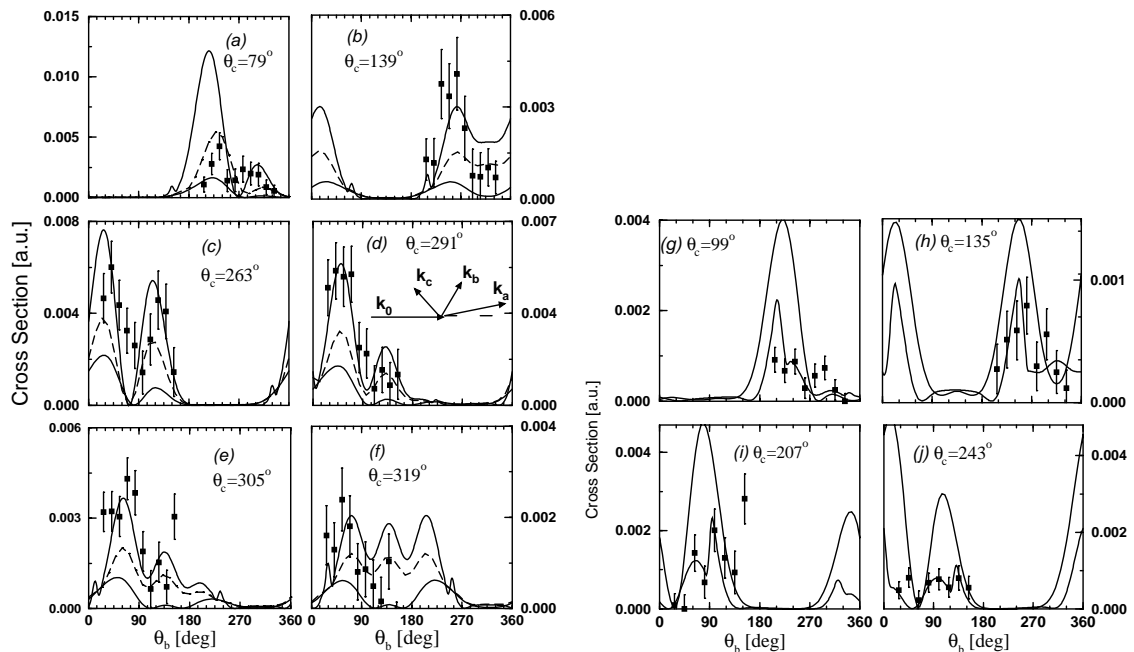


Fig. 5.5. The fully resolved double ionization cross section (FDCS) of $\text{He}(1S^e)$ following electron (solid lines) or positron (dotted line) impact. The scattering geometry is shown by the inset in (d). \mathbf{k}_0 and \mathbf{k}_a are the initial and final state momenta of the projectile while \mathbf{k}_c and \mathbf{k}_b refer to the momenta of the two ejected electrons. The incident energy is 5.6 keV and $k_c^2/2 = k_b^2/2 = 10$ eV. All angles are measured with respect to \mathbf{k}_0 . The projectile is scattered through an angle of 0.45° . The emission angle θ_c of one of the electrons is fixed at the value indicated on the figures while the cross section is scanned as function of the emission angle θ_b of the second electron. The thick solid (dotted) line is the result of the present model for electron (positron impact) whereas the light solid curve is the outcome of the CCC method within the first Born approximation [36]. The data (full square [3]) are on absolute scale. In (g)–(j) the ejected electron energies are varied to $E_c = E_b = 4.5$ eV. In this case [i.e. for (g)–(j)] the experimental FDCS are relative.

of agreement between the FBA and the GF calculations shown in Figs. 5.5 we infer that the first Born limit is approached differently depending on the emission angles and energies of the ejected electrons. The GF theory predicts additional subsidiary peaks in the spectrum shown in Figs. 5.5 which seems to be absent in the FBA (CCC) results (cf. also Refs. [3,36]). The cause of these peaks can be traced down in the theoretical calculations. It lies in interferences between the various terms in the sum (3.47) when evaluating the cross sections. It should be noted however that theories beyond the FBA are still in their infancy, e.g. the GF results shown in Fig. 5.5 have been obtained within the first iteration of (3.46). The evaluation of higher-order terms have not been done yet.

6. Double ionization of many-electron atoms

6.1. The double ionization of noble gases

The theoretical treatment of the double ionization of the outer shell (np^6) of noble gases is a more difficult problem than for the case of the ground-state He target. Even within the frozen-core

approximation one has to deal with a six-electron problem instead of a two active electrons in case of a helium or magnesium atom target. In a first theoretical attempt [115], Dal Cappello and Le Rouzo used the model proposed by Tweed [140] to calculate the 5DCS for (e,3e) reactions for noble gases. This model, called the orthogonalized-Coulomb-wave model takes into account the mutual repulsion between the two ejected electrons by using adjustable charges [141–143]. However, this theory is in a gross disagreement with the $(\gamma, 2e)$ experiments of Schwarzkopf et al. [144] on helium. For up to now, the best model to tackle the double ionization of noble gases seems to be the 3C model [71]. While the CCC-FBA [145] as discussed above is providing good results, it is unfortunately limited to the case of a helium target. The 3C model incorporates the final-state correlation by multiplying the product of two Coulomb waves, representing individual electrons being subject to the full nuclear potential, by a confluent hypergeometrical function which accounts for the mutual repulsion. The Coulomb boundary conditions are exactly satisfied in the asymptotic region. It is important to note that the 3C model as discussed here is appropriate for the description of two slow ejected electrons, while the scattered electron (which is very fast in the experiments) is considered as a non-interactive particle, and hence is described by a plane wave. But this model is not easy to apply when we consider orbitals such as 5p or 5d (which are present in an accurate initial wavefunction). Dal Cappello et al. [146,147] have shown that the repulsive factor (Gamow factor) is often adequate to describe angular correlation in the final state, particularly for symmetric energy configuration of the two slow electrons. This simplified approach, called the approximate 3C model, has been checked in the case of helium and it has been observed that the angular distributions obtained by using this approximation and the exact 3C wave function are often the same, the difference being mostly in the amplitude of the 5DCS. The approximate 3C incorporates only the normalization factor (Gamow factor) of the Coulomb wave corresponding to the interaction of the two slow electrons. Usually, this procedure renders possible efficient numerical evaluation of the cross sections. Moreover, it is possible within this framework to consider the second Born approximation. Within the standard Born approximation, the 5DCS can be written as (cf. Eq. (4.3))

$$\frac{d^5\sigma}{d\Omega_s d\Omega_1 d\Omega_2 dE_1 dE_2} = \frac{4K_s K_1 K_2}{K_i} |M_{B1} + M_{B2}|^2, \quad (6.1)$$

where $d\Omega_s$, $d\Omega_1$ and $d\Omega_2$ denote, respectively, the elements of solid angle for the scattered and the two ejected electrons. The energies of the two ejected electrons are E_1 and E_2 . $\mathbf{K}_{1/2}$ are the momenta of the two slow electrons whereas \mathbf{K}_i , \mathbf{K}_s are respectively the momenta of the incoming and the scattered projectile. Here M_{B1} and M_{B2} are the matrix elements representing the first and the second Born approximation, respectively. By using the well-known frozen-core approximation we are able to reduce the N -electron-target problem to a six-electron-target problem [148]. The matrix element M_{B1} is given by

$$M_{B1} = \frac{-1}{2\pi} \langle \psi_f^- e^{i\mathbf{K}_s \cdot \mathbf{r}_0} | \frac{-6}{r_0} + \sum_{i=1}^{i=6} \frac{1}{r_{0i}} | \psi_i e^{i\mathbf{K}_i \cdot \mathbf{r}_0} \rangle \quad (6.2)$$

where ψ_i is the wavefunction of the initial state (np^6 ; $n=2, 3, 4$ and 5 , respectively, for neon, argon, krypton and xenon) and that of the final state (np^4 and the two ejected electrons). Considering low momentum transfer (as in the experiments of the Orsay group [102,2,5,6,150]) and assuming that the radial functions used to describe the ion (np^4) are the same as the radial functions for electrons in the initial state of the target (np^6) we have been able to reduce this six-electron problem to

a problem of two active electrons. In this case the matrix element is a linear combination of simple matrix elements such as

$$M_{B1ij} = \frac{-2}{K^2} \langle \psi_f^- | e^{i\mathbf{K}\cdot\mathbf{r}_1} + e^{i\mathbf{K}\cdot\mathbf{r}_2} - 2 | \phi_i(\mathbf{r}_1) \phi_j(\mathbf{r}_2) \rangle, \quad (6.3)$$

where ϕ represents the one-electron orbital of the initial wavefunction;

$$\phi(r) = Y_{ml}(\hat{r}) R(n, \varepsilon; r) \quad (6.4)$$

and

$$R(n, \varepsilon; r) = [(2n)!]^{-1/2} (2\varepsilon)^{n+1/2} r^{n-1} \exp(-\varepsilon r). \quad (6.5)$$

The initial wavefunction of the target used here is that of Hda et al. [148] and has been defined by Dal Cappello et al. [151]. It is a correlated wave function calculated by superposition of configurations. The final-state wavefunction ψ_f^- is the approximate 3C model. If we consider that the shake-off mechanism and the TS1 mechanism are included in the first Born approximation [62,152], the second Born approximation is necessary in order to include the contribution of the TS2 mechanism [45]. This last mechanism consists to take into account the interactions between the incoming (projectile) electron and the target. The M_{B2} term will be given by

$$M_{B2ij} = \frac{-2}{\pi^2} \int \frac{d\mathbf{k} \langle \psi_f^- | e^{i\mathbf{K}_a\cdot\mathbf{r}_1} + e^{i\mathbf{K}_a\cdot\mathbf{r}_2} - 2 | e^{i\mathbf{K}_b\cdot\mathbf{r}_1} + e^{i\mathbf{K}_b\cdot\mathbf{r}_2} - 2 | \phi_{i(\mathbf{r}_1)} \phi_{j(\mathbf{r}_2)} \rangle}{K_a^2 K_b^2 (K_1^2 - k^2 - 2I_n)}, \quad (6.6)$$

where $\mathbf{K}_a = \mathbf{K}_i - \mathbf{k}$ and $\mathbf{K}_b = \mathbf{k} - \mathbf{K}_s$.

Here the closure approximation is used instead of adding all the intermediate states of the target [45,40], and the term I_n is treated as a parameter. Because the incident energy is high the value of M_{B2ij} does not depend strongly on the parameter I_n . It is important to note that the M_{B2ij} term is the one responsible for the broken symmetry around the momentum transfer. A further possibility would be to use an exact 3C which will treat the three final state electrons on equal footing, or to use the many-body Green function theory [86], but the calculations become very tedious in the case of the double ionization of noble gases. The term M_{B2ij} nevertheless needs a great amount of care [84] since the integrand is singular when

$$K_a^2 = 0 \quad (6.7)$$

or

$$K_b^2 = 0 \quad (6.8)$$

or

$$k^2 = K_1^2 - 2I_n. \quad (6.9)$$

The measurements of Lahmam-Bennani et al. [102,2,5,6,150] have been obtained in a coplanar configuration (all vectors \mathbf{K}_i , \mathbf{K}_s , \mathbf{K}_1 and \mathbf{K}_2 lie in the same plane) at small scattering angles, high incident energies (keV) and small ejected electrons energies (10–60 eV). Due to the very low ($e, 3e$) cross sections, the experiments were performed with modest energy resolution which did not allow to distinguish the $3P$, $1D$ and $1S$ states of the residual ion.

In such coplanar case, the scattering plane contains the vectors \mathbf{K}_i and \mathbf{K}_s . These vectors can be characterized by an azimuthal angle $\varphi_s = 0$. The other azimuthal angles φ_1 and φ_2 can take values

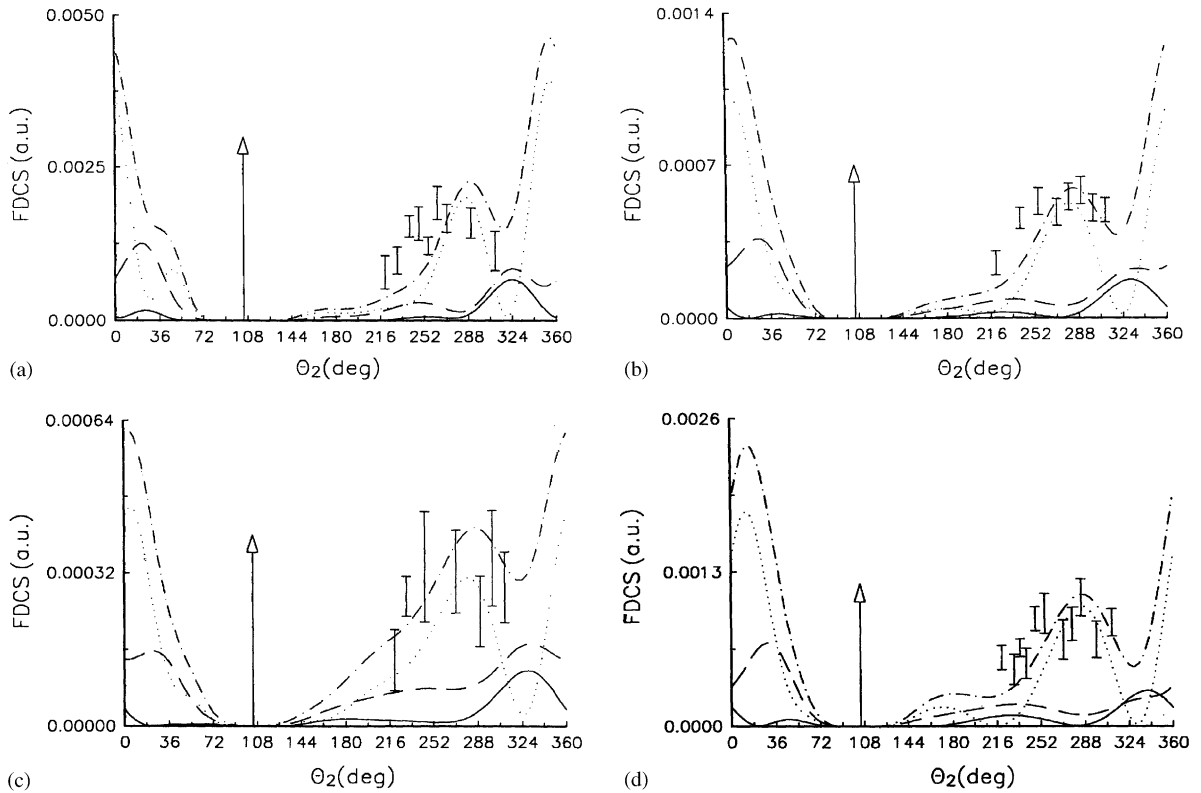


Fig. 6.1. The FDCSs (fivefold differential cross sections) in atomic units for the double ionization of krypton. The scattered electron energy is 5500 eV and the scattering angle is -1° . The ejection energies of the first and the second ejected electrons are, respectively, 15 and 15 eV (a), 45 and 45 eV (b), 30 and 60 eV (c), and 60 and 60 eV (d). The first-ejected-electron angles are 105° . The curves are the first-Born, approximate 3C calculations: solid line: 1S ion state; dotted line 3P ion state; dashed line 1D ion state; dash-dotted line $^1S + ^3P + ^1D$ ion state. Experimental data with error bars are from Ref. [2]. The arrow indicates the direction of the first ejected electron. The theoretical results are multiplied by a factor of 1.3 (b), 0.5 (c) and 12.5 (d).

either 0 or π , while the polar angles θ_1 and θ_2 vary between 0° and 360° (by convention angles are positive in the anti-clockwise direction).

6.1.1. Krypton measurements

This first set of experimental results [2] (obtained at a scattering angle of 1° and a scattered electron energy of 5500 eV) is compared in Fig. 6.1 [40] with the first-Born, approximate 3C model by Dal Cappello and co-workers [40,148]. The agreement is reasonable for all ejected electrons energy values (between 15 and 60 eV). In particular, the shape of the experimental distributions is generally well reproduced by the theory. However, the approximate 3C model is not able to reproduce the correct magnitude of the cross sections (the theoretical results have been multiplied by a factor varying between 0.5 and 12.5). Note that the contributions of the 3P final ion state are found to be dominant over those of the other states.

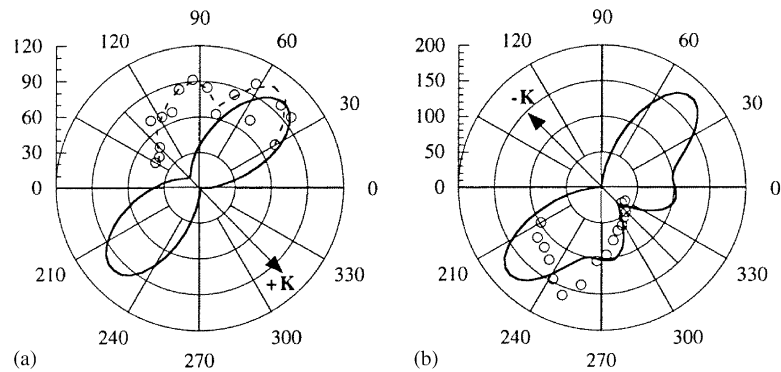


Fig. 6.2. The FDCSs (fivefold differential cross sections) for the double ionization of neon. The electron energies of the incoming, the first and the second ejected electrons are respectively 5500, 10, and 10 eV. The scattering angle is 0.45° . The solid line is the first-Born, approximate 3C calculations corresponding to the $^1S + ^3P + ^1D$ ion state. Experimental data with error bars are from Ref. [6]. The direction of the momentum transfer is indicated by the arrow. The horizontal axis represents the incident direction. The fixed electron direction corresponds to (a) the momentum transfer direction, or (b) to its opposite. The theoretical results are divided by 8 in (a) and by 2.7 in (b).

6.1.2. Neon measurements

The second set of experimental results was obtained using comparable energies (5500 eV for the scattered electron and 10 eV for each ejected electron) [6] but with a lower value for the scattering angle (0.45°). The aim of these experiments has been to test for the presence or absence of the two-step mechanism. Dal Cappello and Le Rouzo [34] and Dal Cappello et al. [151] have shown that, within the first Born approximation, the direction of the momentum transfer is a symmetry axis for the differential cross sections when one electron is ejected along this direction. If this symmetry is destroyed it means that the two-step mechanism is present (or that the second or higher order Born approximation is not negligible). The Fig. 6.2 [6] shows that the symmetry is effectively broken. However, unpublished calculations by Dal Cappello et al. show that the second Born approximation with use of the closure approximation gives a negligible contribution under the present experimental conditions. This disagreement may be due to the closure approximation itself, because Marchalant et al. [154] have shown that for the same scattered electron energy the second Born approximation is important in the process of simultaneous ionization-excitation of a helium target. We also note that the neon target is a particular case because the most probable final ion-state is $1D$ [155] instead of $3P$ for the other noble gases. Experiments showed a backward emission of both ejected electrons (as in the case of argon [5] and a forward emission of both ejected electrons (not present in the case of argon [5]).

6.1.3. Argon measurements

We can distinguish the first (e,3e) measurements [102] from the more recent ones [5] and the latest ones [150]. The first “historical” (e,3e) experiments [102] used electron energies of 5480, 20 and 10 eV, respectively, for the scattered and the ejected electrons, and 0.45° for the scattering angle. A good agreement with the approximate 3C model has been found in this case [84,40] [cf. Fig. 6.3].

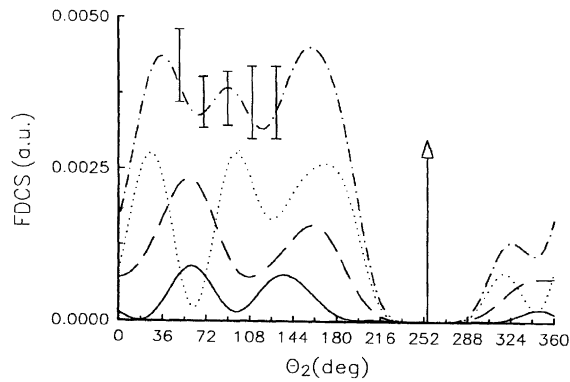


Fig. 6.3. The FDCSs (fivefold differential cross sections) in atomic units for the double ionization of argon. The electron energies are 5480 eV (scattered electron), 20 eV (first ejected electron), and 10 eV (second ejected electron). The scattering angle and the first-ejected-electron angles are -0.45° and 255° , respectively. The curves are: solid line: 1S ion state; dotted line 3P ion state; dashed line 1D ion state; dash-dotted line $^1S + ^3P + ^1D$ ion state; Experimental data with error bars are from Ref. [102]; The direction of the first ejected electron is indicated by the arrow. The theoretical results are multiplied by 0.4.

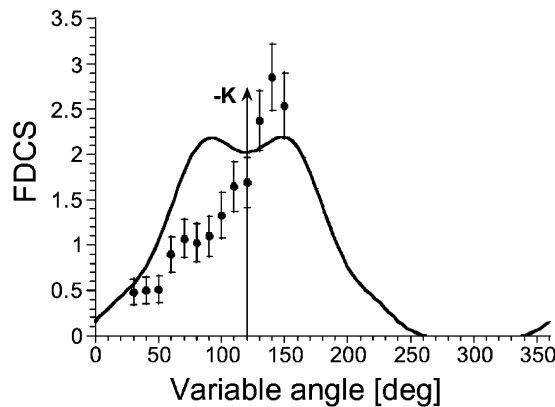


Fig. 6.4. The FDCSs (fivefold differential cross sections) for the double ionization of argon. The electron energies of the incoming, the first and the second ejected electrons are, respectively, 561.4, 9, and 9 eV. The scattering angle is 6.5° . The solid line corresponds to the $^1S + ^3P + ^1D$ ion state; The experimental data with error bars are taken from Ref. [150]. The opposite direction of the momentum transfer is indicated by the arrow. The fixed electron direction corresponds to the opposite of the momentum transfer direction.

In the second set of experimental data [5] the same kinematical conditions as in the neon case [6] were used. The main result is that the second Born approximation must be taken into account because the symmetry (about the momentum transfer direction) is also broken [5], as in the Ne case. The third set of experimental data [150] has been performed at lower incident energy (561.4 eV) in order to further probe the importance of the two-step mechanism. The broken symmetry and the appearance of a small structure near the main peak show clearly that the non-first order effects (such as TS2 mechanism) play an important role, more important than in the previous case [5]. Fig. 6.4

[150] shows that the approximate 3C model used in the first Born approximation is not sufficient here, even though the disagreement between first Born theory and experiments is generally speaking not too bad: the approximate 3C model correctly predicts the position of the two main peaks but is not able to explain the lack of symmetry and the small peak.

6.2. The double ionization of magnesium

The magnesium atom is a particularly attractive target for double ionization studies because it is a quasi-two-electron atom³ comparable with doubly excited states in He which exhibit strong ground-state electron correlation.

Experimental studies on the double ionization of magnesium have been conducted by Coplan and coworkers et al. [15,11] at College Park. The aim has been to obtain a direct information on the correlated initial state wave function as proposed by several authors. It has been suggested that certain experimental arrangement are most favorable for initial-state correlation studies, in particular:

- Berakdar [67] showed that the condition $k_{\text{ion}}=0$ (where k_{ion} is the ion recoil momentum) which is the counterpart condition of the single-particle electron–momentum spectroscopy [117], is reached on a two-dimensional Bethe sphere in momentum space. Initial-state correlation studies has to be performed such $k_{\text{ion}}=0$.
- Srivastava et al. [137] have made some calculations with this “Bethe-sphere” condition by varying the energies of the ejected electrons.
- Popov et al. [138] proposed to consider a situation where one ejected electron and the scattered electron have the same energy (for instance 250 eV) while the second ejected electron is slower (for instance 5 eV). This last situation is described by the shake-off mechanism which leads to a direct relationship between the differential cross section and the double Fourier transform of the initial state wavefunction (as single-particle electron–momentum spectroscopy [117]).

Coplan et al. have chosen a non-coplanar scattering geometry where one ejected electron is detected in a cone above the scattering plane while the second ejected electron is detected in another cone below the scattering plane. In this out-of-plane geometry the shake-off mechanism is not the most probable. Nevertheless, Coplan et al. were able to observe an atomic two-electron momentum distribution [11]. In fact, if we consider both ejected electrons as one single particle the double ionization looks like a single ionization. This was recently established by Perumal et al. [139] in the double ionization of helium by impact of Au^{53+} ions, and by Lahmam–Bennani et al. [7]. These results open several questions about the mechanisms of the double ionization: the three mechanisms (shake-off, TS1 and TS2) are not able to give such a result, and we may consider another mechanism where the two target electrons are ejected at same time (as in molecular dissociation) while sharing the momentum transfer given by the incoming particle.

³In magnesium the two active electrons are the two 3s electrons outside of a closed shell, i.e. the doubly ionized ground state has an inert gas electronic configuration.

7. Integral cross sections

In the preceding sections we investigated the fully differential cross sections, i.e. the cross sections where the momenta of all three final state electrons are determined. The (e,3e) experiments can as well be carried out in a less differential way by integrating over the kinematical parameters of one of the continuum electrons. Thus in this case the vector momenta of only two electrons are determined experimentally. This kind of measurements is called the (e,3-1e) experiments and constitutes a valuable and a less tedious method for the energy and/or angular differential studies of the double ionization process. In the following, we will first focus on the energy partitioning between the two slow escaping electrons at a given momentum and energy transfer to the target. Secondly, we will discuss the angular correlations between two out of the three electrons which will be shown to be of great utility in disentangling the different types of pathways of the double ionization channel.

7.1. Energy partitioning

Duguet et al. [129] used the (e,3-1e) technique to measure the energy partitioning between the two electrons ejected from an argon target, at a given momentum transfer and fixed energy transfer values. They detected the fast electron in coincidence with one slow electron at fixed angles θ_a and θ_b and variable energy E_b , measuring thus a four-fold differential cross section (4DCS). Their results for the absolute 4DCS measurements are shown in Fig. 7.1, revealing two main features: (i) A confirmation is given that the energy partitioning between the two escaping electrons is far from being even (with respect to the equal energy point). An almost vanishing probability is observed for the equal-energy sharing case, $E_b = E_c$, while the highest cross section is recorded when one electron emerges with almost all the available excess energy (the other is then very slow). (ii) A remarkable feature of Fig. 7.1 is that the U-type energy distribution is found to be not symmetrical about the mid-excess energy $(E_b + E_c)/2$. The relevance of this remark becomes clear when we

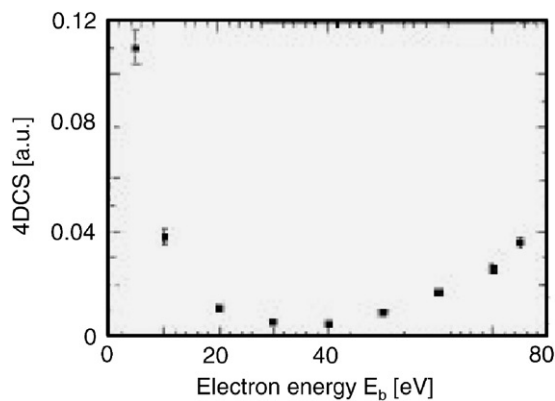


Fig. 7.1. The absolute fourfold differential cross section as function of the energy sharing between the two electrons ejected from an argon atom. The error bars are one statistical standard deviation. Experimental parameters are $\theta_a = 0.55^\circ$, $\theta_b = 50^\circ$, $E_0 = 5623$ eV and $E_a = 5500$ eV, so that the excess energy above the double ionization threshold is fixed, $E_b + E_c = 80$ eV.

compare with similar energy distributions measured in electron-impact single ionization [(e,2e)] [65] or photon-impact double ionization [(γ ,2e)] [131]; in both cases the final channel consists of two continuum electrons moving in the field of an ionic core. There [65,131], the energy spectrum of the outgoing electron is determined from the measurement of a singly differential cross section, $d\sigma/dE$, versus the electron energy E . Such cross section distributions must be symmetrical about a point midway between zero and the maximum available energy for the electrons pair, E_{\max} , for the two electrons are indistinguishable and if one of the electrons possesses the energy $E_b < E_{\max}$ the other electron must have the energy $E_c = (E_{\max} - E_b)$. When higher order differential cross sections are measured as is the case in [129], the obtained U-type energy distribution should not be symmetrical for two major reasons: (i) The first one is of an intrinsic “physical” nature as the pair of emitted electrons with complementary energies E_b and E_c might have a priori different angular distributions. Hence, different intensities should be observed when both electrons are detected at a particular angles, yielding a non-symmetrical energy distribution at these angles. (ii) The second reason is of an “experimental” nature, due to the fact that E_c is not measured in [129]. Because of the different possible final states of the Ar ion, there is at each E_b value not only one single possible energy for the undetected c -electron, but several discrete E_c values in the case of double ionization, and a whole continuum of energies in the case of triple ionization. (Nevertheless, the double ionization process should be largely dominant over the triple and higher order processes [89].) Each of these final states contributes to the energy spectrum of Fig. 7.1 with its proper U-type distribution, extending from $E_b = 0$ up to the corresponding threshold (i.e. $E_c = 0$). Obviously, the sum of all individual U’s yields an asymmetric total distribution. To solve this ambiguity, an (e,3e) experiment involving triple coincidences is needed to separately measure every individual distribution.

7.2. Angular correlations in integral cross sections

The energy partitioning discussed in the preceding section is studied by performing an (e,3-1e) coincidence experiment where the electron pairs (e_a) or (e_b) are detected at fixed outgoing angles. A different type of information concerning the double ionization mechanism is obtained if the coincidence angular correlations are measured at fixed energies. This can be done either in the cb -mode (where the two slow electrons b and c are detected) [103,132,133] or in the ab -mode (where the fast scattered electron a and one of the slow electrons b are detected) [102,10]. In both cases one electron remains undetected. The cross section for the cb -mode is obtained as

$$\sigma_{c,b} := \frac{d^6\sigma}{d\Omega_c d\Omega_b dE_c dE_b} = \int \frac{d^8\sigma}{d\Omega_c d\Omega_b d\Omega_a dE_c dE_b} d\Omega_a . \quad (7.1)$$

Experiments in the cb -mode have shown that by adequately choosing the kinematical parameters one may zoom in certain double ionization mechanisms. For instance, if the two slow electrons are detected in opposite half planes with respect to the incoming beam, as done in [103], different ionization mechanisms yield different angular distributions. In particular, if the emitted electrons share unequally the available excess energy (i.e. when the speed of one electron is significantly larger than that of the other one), then the double ionization is predominantly the result of a SO process when the incident energy is high (~ 5.5 keV in the experiments discussed here). That is, the fast electron is first ejected in a “single-ionization (e,2e)-like” process, and is located at approximately $\pm 80^\circ$ from the incident direction. Hence, its angular distribution for fixed angular position θ_{slow} of the other

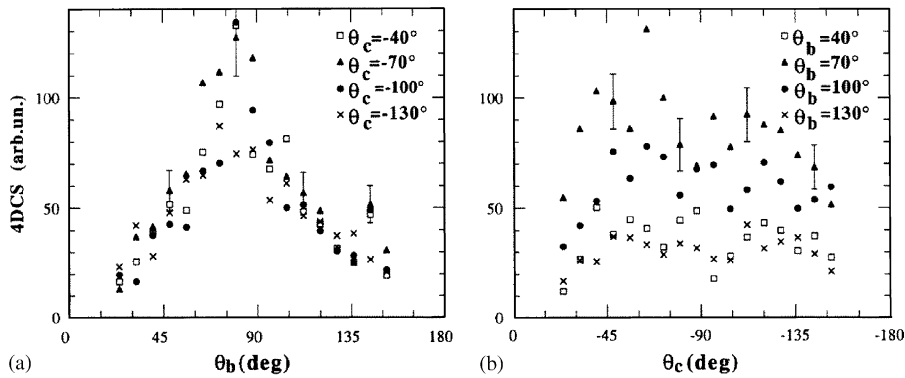


Fig. 7.2. The relative four-fold differential cross section for double ejection from Ar at $E_0 = 5500$ eV. (a) The slow electron with energy $E_c = 17.5$ eV is detected at fixed θ_c angle, and the fast one with $E_b = 96$ eV is mapped versus θ_b in the opposite half-plane. (b) Same, with the fast electron angle, θ_b , fixed, and the slow one, θ_c , variable.

very slow electron must be peaked and independent (both in shape and in intensity) of the fixed angle θ_{slow} . As discussed earlier the slow electron emitted in a SO process should have an isotropic angular distribution independently of the emission angle of the second (fast) electron θ_{fast} . This is what is observed in the 4DCS distributions measured by El Marji et al. [103], shown in Fig. 7.2. The fast ejected electron is detected at an energy $E_b = 96$ eV in the angular range $20^\circ \leq \theta_b \leq 160^\circ$, whereas the slow one is detected at $E_c = 17.5$ eV in the range $-160^\circ \leq \theta_c \leq -20^\circ$. The data are displayed as a function of θ_b for fixed θ_c , in Fig. 7.2(a), and as a function of θ_c for fixed θ_b in Fig. 7.2(b). The absolute scale was not determined for these experiments, however the data are all given on the same relative scale. Clearly, the fast electron distribution in Fig. 7.2(a) is peaked at $\theta_b \sim 80^\circ$ and is independent of the observation angle θ_c of the slow electron, both in shape and in magnitude. Whereas the slow electron distribution in Fig. 7.2(b) is perhaps not fully isotropic but at least much flatter at all θ_b angles, with an intensity which depends on the observation angle θ_b . Both observations support the conclusion that under the kinematical conditions of these experiments, the dominant DI mechanism is the SO mechanism.

As discussed below in details, a similar conclusion was also reached theoretically [134,130] when investigating the mechanisms of double ionization in $(e,3-1e)$ processes using a helium target. Similar $(e,3-1e)$ experiments were also performed in Maryland by Coplan et al. [15] on magnesium.

7.3. Angular correlation studies on He

In the $(e,3-1e)$ process two electrons are detected simultaneously in the final state [according to Eq. (7.1)]. The relation of $(e,3-1e)$ to other reactions where as well two electrons are detected in coincidence ([e.g. $(\gamma,2e)$]) depends however on how the $(e,3-1e)$ is performed. E.g., the integration over the scattered electron angle in Eq. (7.1) can be essentially transferred into an integration over the momentum transfer vector \mathbf{K} which runs in a some limited interval. To compare this kind of $(e,3-1e)$ measurements with the $(\gamma,2e)$ process, using the optical limit [compare Eq. (2.52)], one should thus conduct the $(\gamma,2e)$ experiments using linear polarized light and then performs an integration over the direction of the polarization vectors in some specified region. On the other hand

one can perform the (e,3-1e) experiment such that the momentum transfer vector \mathbf{K} is fixed and fully determined experimentally. This facilitates then a direct comparison of (e,3-1e) experiments with available $(\gamma, 2e)$ data using the relation [compare Eq. (2.52)]. This kind of experiments is discussed in detailed following a brief survey of the theoretical and experimental studies of (e,3-1e) performed according to Eq. (7.1)].

For a theoretical analysis of the $\sigma_{c,b}$ we employ the FBA and use the 3C model, as discussed in Sections 2.3 and 3.2.1. In addition, we use the orthogonalized form (2.51) of the wave function $\psi_{\mathbf{k}_b, \mathbf{k}_c}^-(\mathbf{r}_b, \mathbf{r}_c)$ for the description of the two slow escaping electrons in the field of He^{2+} . The singlet ground state of helium is described by a Hylleraas-type wave function (5.6) which we introduced in the preceding section. To be specific we concentrate on the experiments conducted in Ref. [130] where the incident energy is fixed to be $E_0 = 5525$ eV and one electron, say electron c , is detected at a fixed angle perpendicular to the incident direction. The energy transferred to the target is fixed to $E_c + E_b = 35$ eV. Furthermore, co-planar geometry is chosen. The angular distribution of electron b has three limiting cases, namely $E_b \gg E_c$, $E_b = E_c$ or $E_c \gg E_b$. Basically, in all cases a maximum in the cross section $\sigma_{c,b}$ is expected whenever the Bethe sphere [35] is approached, i.e. when the energy and momentum transferred to the target are directly absorbed by the ionized electrons. As we integrate (in a limited region) over \mathbf{K} to obtain $\sigma_{c,b}$ (Eq. (7.1)) the Bethe sphere conditions are not directly applicable as introduced in Ref. [35]. However, the integrated quantity

$$k_{\text{av}}(\Omega_c, \Omega_b, E_c, E_b) = \int k_{\text{ion}}(\Omega_a, \Omega_c, \Omega_b, E_c, E_b) d\Omega_a, \quad (7.2)$$

is well defined and indicates the average momentum transferred to the nucleus at a certain geometry. Thus, a minimum in $k_{\text{av}}(\Omega_b)$ corresponds to a maximum in the angular distribution $\sigma_{c,b}(\Omega_b)$. This is demonstrated in Fig. 7.3(a) where $E_b = 34.8$ eV $\gg E_c = 0.2$ eV. The minimum of k_{av} as function of $\theta_b := \cos^{-1}(\hat{\mathbf{k}}_0 \cdot \mathbf{k}_b)$ is located at $\theta_b \approx 64^\circ$. Correspondingly, the direct scattering off electron b which provides the main contribution to $\sigma_{c,b}(\theta_b)$ peaks at $\theta_b \approx 70^\circ$ (cf. Fig. 7.3(b)). This means, predominantly, the projectile electron scatters directly from electron b which escapes carrying away almost the whole momentum transferred to the target. Electron c is then emitted upon the sudden change in the effective field of target. Hence, the direct projectile scattering off electron c is almost structureless and yields a minor contribution to the binary peak (in the angular distribution of electron b) located at $\theta_b \approx 70^\circ$ (compare Fig. 7.3(b)). Clearly, this mechanism depends strongly on the description of the initial-state which decides the amount of shake-off [120,62,131]. The final-state electronic correlations are of minor relevance in this case [35].

The shape of $\sigma_{c,b}(\theta_b)$ is determined by the coherent sum of the amplitudes T_c and T_b as given by Eq. (2.48) and (2.49). The interference of these amplitudes is appreciable due to the relatively small energy separation $E_b - E_c$. The case $E_c \gg E_b$ yields similar results with the interpretation as above but the roles of electron c and electron b being interchanged. The quantity k_{av} does not vanish even on the Bethe sphere. This is because the momentum conservation law (Eq. (2.1)) is the result of a translational invariance of the system and does not account for internal degrees of freedom of the target initially at rest. The momentum distribution of the nucleus in the initially bound-state is exactly cancelled to a zero linear momentum by the presence of the bound electrons. When the electrons are directly ionized and no momentum is transferred to the nucleus during the collision the nucleus recoils with a momentum equal to the initial binding momenta of the electrons before the collision.

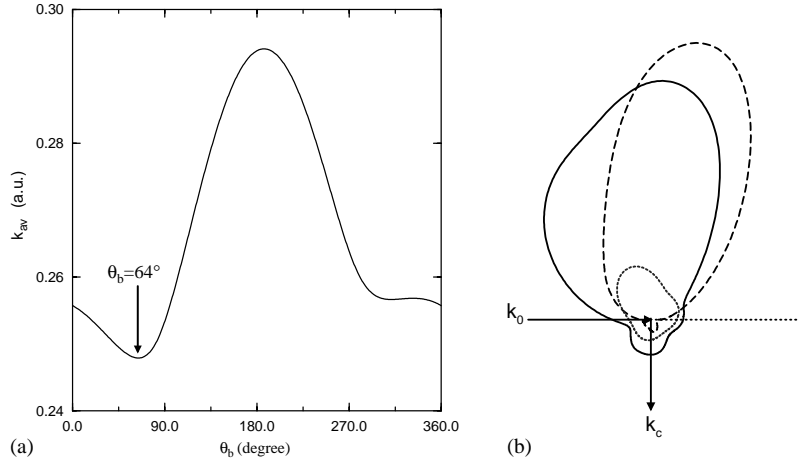


Fig. 7.3. The average momentum transferred to the nucleus k_{av} as function of $\theta_b = \cos^{-1}(\hat{\mathbf{k}}_0 \cdot \hat{\mathbf{k}}_b)$. The collision geometry is chosen as $E_0 = 5525$ eV, $E_c + E_b = 35$ eV, $E_c = 0.2$ eV, $\mathbf{k}_0 \cdot \mathbf{k}_c = 0$ and $(\mathbf{k}_0 \times \mathbf{k}_c) \cdot \mathbf{k}_b = 0$. The inset (b) show the angular distribution $\sigma_{c,b}(\theta_b)$ as function of θ_b , determined with respect to $\hat{\mathbf{k}}_0$. An orthogonal 3C wave function is employed for the final state. The incoherent contributions of T_b , i.e. $T_{fi} \equiv T_b$, (dashed curve) and of T_c , i.e. $T_{fi} \equiv T_c$, (dotted) are shown along with their coherent sum (solid curve) (cf. Eqs. (2.48) and (2.49)).

Now we consider the case of equal-energy secondary electrons $E_c = E_b$. In this case, the scattering amplitudes T_c, T_b corresponding to the electrons c and b are of the same order and coincide at $\theta_b = 90^\circ$ due to symmetry (Fig. 7.4(a)). That means, in this case the projectile ionizes the two target electrons simultaneously. The FBA leads to only single-particle perturbation operators for the (e,3e) process, i.e. the projectile does not directly interact with the center-of-mass of the two electrons. Therefore, the double ionization of the two electrons at the same time must proceed via a coherent superposition of the amplitudes T_c and T_b (Fig. 7.4(a)). The cross section $\sigma_{c,b}(\theta_b)$ (Fig. 7.4(a)) exhibits a minimum at $\theta_b \approx 72^\circ$. This minimum is due to interference of T_c and T_b and incidentally coincides with the minimum of the average momentum transferred to the nucleus k_{av} at $\theta_b \approx 72^\circ$ (Fig. 7.3(b)). This could be inferred from the structure of the incoherent contributions of T_c and T_b which reveal broad maxima around $\theta_b = 94^\circ$ and 84° , respectively. At $\theta_b = 0$ the cross section vanishes due the electron–electron repulsion in the final state. Obviously, in the case of Fig. 7.4(a)–(c) the cross section is very sensitive to the weighting of the coherent amplitudes T_c and T_b which is determined by the wave functions $\psi_{\mathbf{k}_a, \mathbf{k}_b}^-(\mathbf{r}_a, \mathbf{r}_b)$ and $\varphi(\mathbf{r}_a, \mathbf{r}_b)$. Therefore, the scattering amplitude from the nucleus T_T , which is mainly due to a poor description of the three-body state, strongly affects the cross section because it considerably alters the interference behavior (Fig. 7.3(c)). Therefore, orthogonalized and non-orthogonalized final-state wave functions yield in this case quite different results. The experimental finding is qualitatively reproduced by the orthogonalized form which seems to better fit the experimental data.

The intermediate situation between the cases displayed in Figs. 7.3(a) and 7.4(c) is shown in Fig. 7.4(d). The agreement with the data is satisfactory. From the above arguments it is comprehensible that the term T_T does not severely affect the cross section as in Fig. 7.4(c). The ionization amplitude T_b provides the major contribution to T_{fi} in the vicinity of the maximum. This leads

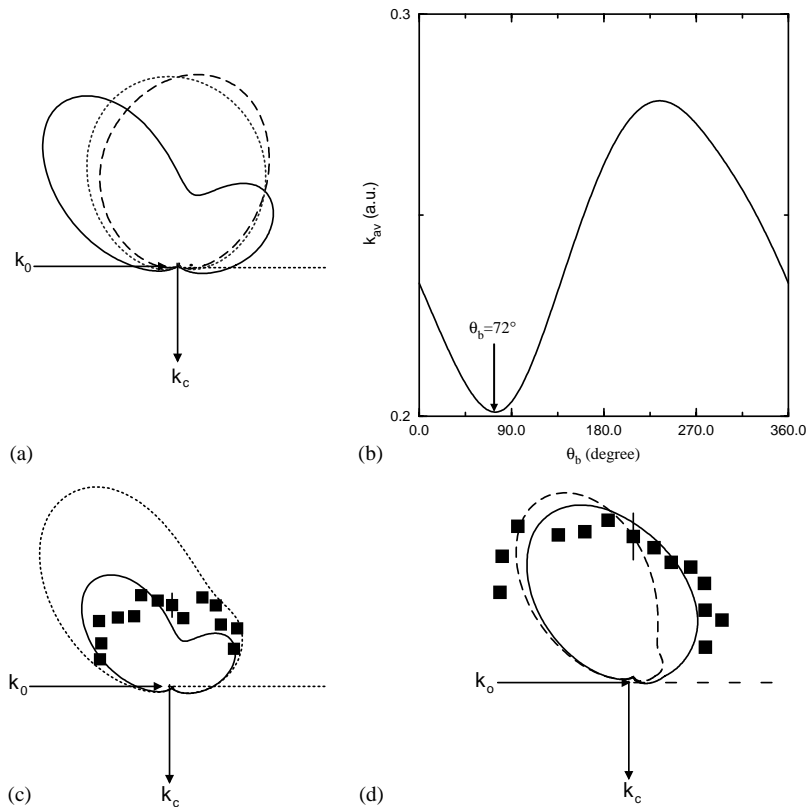


Fig. 7.4. The same collision geometry as in Figs. 7.3, however $E_c = E_b$. Wave functions and curves are also the same as in Fig. 7.3(b). Panel (b) shows the angular distribution of the average momentum k_{av} whereas in (c) the results are displayed of the orthogonalized (solid curve) and non-orthogonalized (dotted curve) 3C wave functions. Experimental data (squares) are due to Ref. [130]. In (d) the angular distribution $\sigma_{c,b}(\theta_b)$ is shown for the case $E_c = 7$ eV. Calculations using orthogonalized (solid curve) and non-orthogonalized (dotted curve) wave functions are depicted along with experimental data (squares) Ref. [130].

to the interpretation as in Fig. 7.3(a) and (b). The scattering term T_c , although smaller than T_b (i.e. $|T_b| > |T_c|$), still interferes considerably with T_b .

7.4. Asymmetry parameters for (e,3-1e) reactions

In this part of the article we explore the link of (e,3-1e) to (γ ,2e) reactions through the optical limit Eq. (2.52). To this end and to analyse the partial waves contributing to the (e,3-1e) cross sections we consider situations where \mathbf{K} is fixed and the angular distribution of one secondary electron is measured, i.e.

$$\sigma_{\mathbf{K},c} := \frac{d^6\sigma}{d\Omega_c d\Omega_a dE_c dE_a} = \int \frac{d^8\sigma}{d\Omega_c d\Omega_b d\Omega_a dE_c dE_a} d\Omega_b. \quad (7.3)$$

Hereafter all angles are measured with respect to $\hat{\mathbf{K}}$ which defines the z -axis. The cross section $\sigma_{\mathbf{K},c}$ is proportional to the cross sections $d^6\sigma/(d\Omega_c d\Omega_a dE_c dE_b)$ and $d^6\sigma/(d^3\mathbf{K} d\Omega_c dE_c)$. The latter one reveals the connection to $(\gamma, 2e)$ measurements with linear polarized light where only one photo electron is resolved in energy and angle $d^3\sigma^{\text{DPI}}/(d\Omega_c dE_c)$, the so-called asymmetry-parameter experiments [127,135,136].

Due to the cylindrical symmetry of $\sigma_{\mathbf{K},c}(\Omega_c)$ with respect to \mathbf{K} the angular dependence of the cross section $\sigma_{\mathbf{K},c}$ (Eq. (7.3)) occurs though $\hat{\mathbf{K}} \cdot \hat{\mathbf{k}}_c$ only and therefore this cross section can be parameterized in the form [134]

$$\frac{d^6\sigma}{d\Omega_c d\Omega_a dE_c dE_a} = 4\pi \sum_{\ell=0}^{\infty} B_{\ell} P_{\ell}(\hat{\mathbf{K}} \cdot \hat{\mathbf{k}}_c) , \quad (7.4)$$

where $B_{\ell}(\mathbf{K}, E_c)$ are angle-independent coefficients and $P_{\ell}(\hat{\mathbf{K}} \cdot \hat{\mathbf{k}}_c)$ are Legendre polynomials describing the angular dependence.

From the relations

$$\begin{aligned} \frac{d^4\sigma}{d\Omega_a dE_c dE_a} &= 4\pi \sum_{\ell=0}^{\infty} B_{\ell} \frac{4\pi}{2\ell + 1} \sum_{m=-\ell}^{\ell} \int d\Omega_c Y_{\ell m}(\hat{\mathbf{k}}_c) Y_{\ell m}^*(\hat{\mathbf{K}}) \\ &= 16\pi^2 \sum_{\ell=0}^{\infty} B_{\ell} \sum_{m=-\ell}^{\ell} \frac{1}{2\ell + 1} \delta_{\ell 0} \delta_{m 0} , \end{aligned} \quad (7.5)$$

we conclude that the coefficient $B_0(\mathbf{K}, E_c)$ is related to integrated cross sections, i.e.

$$B_0(\mathbf{K}, E_c) = \frac{1}{16\pi^2} \frac{d^4\sigma}{d\Omega_a dE_c dE_a} . \quad (7.6)$$

Since B_0 is a constant with the dimension of a cross section we can renormalize all the expansion coefficients B_{ℓ} to B_0 and obtain thus dimensionless generalized asymmetry parameters $B_{\ell}^s = B_{\ell}/B_0$ which yields

$$\sigma_{\mathbf{K},c} = \frac{1}{4\pi} \frac{d^4\sigma}{d\Omega_a dE_c dE_a} \sum_{\ell=1}^{\infty} [1 + B_{\ell}^s P_{\ell}(\cos \theta_c)] . \quad (7.7)$$

As well known we can do the same analysis in the case of $(\gamma, 2e)$ for the integrated cross section $d^3\sigma^{\text{DPI}}/(d\Omega_c dE_c)$. In this case the parametrization of $d^3\sigma^{\text{DPI}}/(d\Omega_c dE_c)$ has only two terms. This is a result of the definite angular momentum imparted to the system by the photon and because polarization vector enter bi-linearly in the cross section. The expansion for $d^3\sigma^{\text{DPI}}/(d\Omega_c dE_c)$ reads

$$\frac{d^3\sigma^{\text{DPI}}}{d\Omega_c dE_c} = 4\pi \sum_{\ell=0}^{\infty} B_{\ell}^{\text{DPI}} P_{\ell}(\cos \theta_c) = \frac{1}{4\pi} \frac{d\sigma}{dE_c} [1 + \beta P_2(\cos \theta_c)] , \quad (7.8)$$

here θ_c refers to the emission angle of the photoelectron with respect to the polarization vector which can be chosen to coincide with $\hat{\mathbf{K}}$. Hence, one single parameter, the *asymmetry parameter* $\beta \in [-1, 2]$, is sufficient to characterize the whole angular distributions of the photoelectrons. Thus, instead of comparing the angular distributions for $(e, 3-1e)$ and $(\gamma, 2e)$ reaction to explore the regime of the optical limit one needs only compare the asymmetry parameters B_{ℓ}^s and β .

A relation between B_ℓ and B_ℓ^{DPI} can be established by considering a situation where $(e, 3-1e)$ and $(\gamma, 2e)$ yield continuum electrons with the same vector momenta, i.e. $\mathbf{k}_c^{\text{DPI}} = \mathbf{k}_c$ and $\mathbf{k}_b^{\text{DPI}} = \mathbf{k}_b$ where $\mathbf{k}_c^{\text{DPI}}, \mathbf{k}_b^{\text{DPI}}$ are the vector momenta of electrons emitted upon $(\gamma, 2e)$. Assuming length formulation for the $(\gamma, 2e)$ reaction, the cross section, given by Eq. (7.8), reads

$$\frac{d^3\sigma^{\text{DPI}}}{d\Omega_c dE_c} = 4\pi^2 \alpha \omega k_c k_b \int |\langle \psi_{\mathbf{k}_c, \mathbf{k}_b}^-(\mathbf{r}_c, \mathbf{r}_b) | \hat{\mathbf{K}} \cdot (\mathbf{r}_c + \mathbf{r}_b) | \varphi(\mathbf{r}_a, \mathbf{r}_b) \rangle|^2 d\Omega_b, \quad (7.9)$$

where ω is the light frequency and α is the fine-structure constant. From Eqs. (2.52) and (7.9) we deduce that in the optical limit the parameters B_ℓ tends to scaled $(\gamma, 2e)$ coefficients $\bar{B}_\ell^{\text{DPI}}$, where

$$\bar{B}_\ell^{\text{DPI}} = (2\pi)^4 \frac{4k_c}{k_0 K^2 \alpha \omega} B_\ell^{\text{DPI}}. \quad (7.10)$$

Fig. 7.5(a) illustrates the above formulations. We choose the situation where $(e, 3-1e)$ and $(\gamma, 2e)$ can be compared (small momentum transfer, high incident energy). We also recall that due to parity arguments the use of orthogonalized (2.51) and non-orthogonalized final-state wave functions must lead to the same predictions when the optical limit applies. In Fig. 7.5(a) all angular distributions are symmetric with respect to $\theta_c = \pi$. Furthermore for $(\gamma, 2e)$ the cross sections $d^3\sigma^{\text{DPI}}/(d\Omega_c dE_c)$ are symmetric to the plane perpendicular to the linear polarization vector. This symmetry is absent for the $(e, 3-1e)$ reaction since, in contrast to $(\gamma, 2e)$ where the polarization vector defines an axis leading to the reflection symmetry at $\theta_c = 90^\circ$ and 270° , the momentum transfer vector \mathbf{K} is a polar vector.

This fact is immediately reflected in the behavior of the asymmetry parameters: For $(\gamma, 2e)$ the asymmetry parameter B_1^{DPI} is identically zero, whereas for $(e, 3-1e)$ the parameter B_1 (Eq. (7.3)) is finite [Fig. 7.5(b)]. Therefore, we identify the physical meaning of the asymmetry parameter $B_1^s = B_1/B_0$ as an indicator for the “memory” of the ionized electrons to the initial direction of the incident beam.

As we indicated above, the parameter B_2^s in $(e, 3-1e)$ reaction is the counterpart of the asymmetry parameter β in $(\gamma, 2e)$ which describes the angular distribution of the photoelectron.

Its physical meaning becomes apparent when we assume $K \ll 1$, $B_1^s \ll 1$. A vanishing $\beta = 0$ ($B_2^s = 0$) means that the electron c has an isotropic angular distribution that reflects the symmetry of the initial state of the target, i.e. this electron c is emitted in a shake-off process whereas the other electron is ejected upon a direct encounter with the projectile. This case occurs when $E_b/E_c \ll 1$ (see Figs. 7.5(a) and (b)). Reversal of the roles of the two secondary electrons, i.e. $E_c/E_b \ll 1$ leads to $\beta = 2$ ($B_2^s = 2$) which means that electron c is directly ionized by a binary collision with the projectile and is emitted along the momentum transfer direction which in our case is chosen to be the quantization axis. Clearly, in both case $\beta = 0, \beta = 2$ the two continuum electrons are well separated in momentum space and therefore are weakly correlated.

In contrast to the case $\beta = 2$ ($B_2^s = 2$) a negative value of β (B_2^s) means that the electron c appears under a direction considerably different from \mathbf{K} [perpendicular to \mathbf{K} for $\beta = -1$, ($B_2^s = -1$)]. It is in this situation where the electronic correlation plays the key role. This statement is endorsed by comparing Fig. 7.5(a) and Fig. 7.5(c) and (d). In the latter case the two electrons emerge with equal energies which means evidently that they are strongly correlated leading thus to a negative value of B_2^s , as apposed to the case of Fig. 7.5(a) where electronic correlation is weak. We note however that since the excess energy is relatively high $E_c + E_b = 120$ eV the electronic correlation

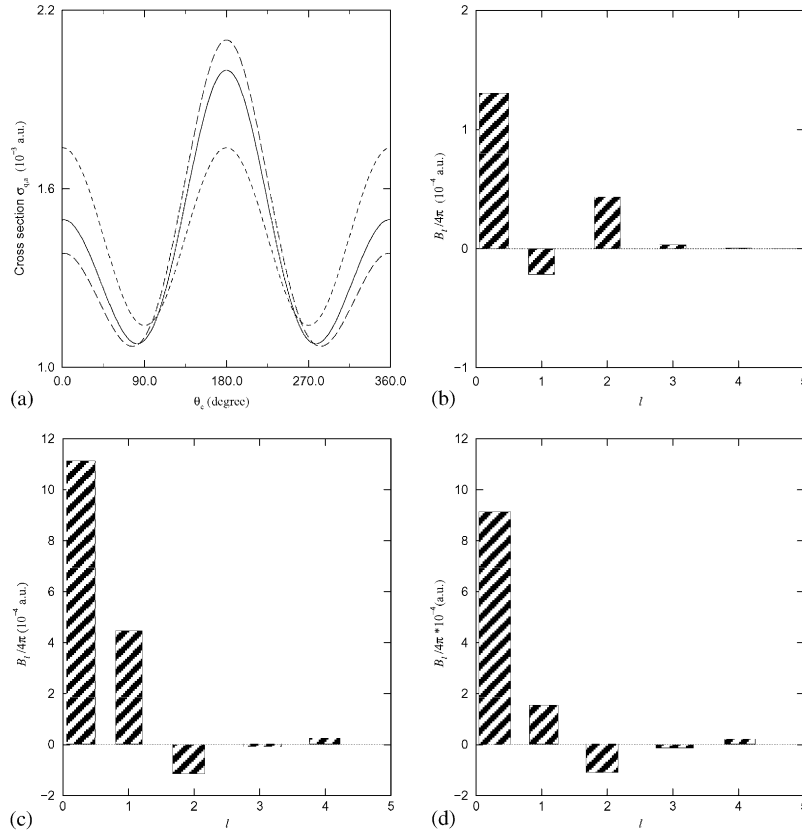


Fig. 7.5. The cross section $\sigma_{\mathbf{k},c}(\theta_c)$, as defined by Eq. (7.3), as function of $\theta_c = \cos^{-1}(\hat{\mathbf{K}} \cdot \hat{k}_c)$. The incident energy is $E_0=8$ keV. The scattered projectile is detected under 1° with respect to \mathbf{k}_0 and has an energy $E_a=7.8$ keV. The momentum transfer is $K=0.509$ a.u. and $E_c=0.01$ eV. Results of orthogonalized (dashed curve) and non-orthogonalized (solid curve) wave functions are shown. The dotted curve is the corresponding DPI-cross sections, as given by Eq. (7.8), but with coefficients $\bar{B}_\ell^{\text{DPI}}$ (see Eq. (7.10)). The DPI-asymmetry parameter is $\beta=0.29728$. (b) Shows for the same arrangement as in (a) the asymmetry coefficient B_ℓ as function of ℓ (cf. Eq. (7.4)). For DPI we obtain $B_0^{\text{DPI}}/4\pi=1.34 \times 10^{-3}$, $B_2^{\text{DPI}}/4\pi=0.3984 \times 10^{-3}$, (note $\beta = B_2^{\text{DPI}}/B_0^{\text{DPI}} = 0.297$). Panel (c) shows B_ℓ as function of ℓ for the same collision arrangement as in (a), but in this case $E_c = E_b$. An orthogonalized wave function is used to describe the final state. (d) Shows same quantity as (c), however the final-state wave function is not orthogonal to the initial bound state of $\text{He}(^1S^e)$.

is less prominent when the two electrons are separated in angles. This situation changes drastically for lower excess energies and B_2^s tends to -1 .

Obviously the parameters $B_\ell, \ell > 2$ exist only for the (e,3-1e) case. Their symmetry properties are readily deduced from the respective ℓ .

From Eq. (7.7) it is evident that the coefficient B_0 determines the absolute value of the cross section and offers a convenient way to compare (or to calibrate) the magnitude of the (e,3-1e) cross sections to the $(\gamma, 2e)$ data [by comparing the numbers B_0 and \bar{B}_0^{DPI} , as defined by Eq. (7.10)].

With an increasing divergence from the optical limit an increasing number of partial waves is required to fit the (e,3-1e) cross sections. If the deviations from the optical limit is moderate the

significant contributions to the series (7.7) is due to the first three terms. Therefore, we assume in this regime that $B_\ell^s = 0$, $\forall \ell > 2$ and write the series Eq. (7.7) in the form

$$\sigma_{\mathbf{K},c} = \frac{1}{4\pi} \frac{d^4\sigma}{d\Omega_a dE_c dE_a} [1 + \alpha^{e3e} P_1(\cos \theta_c) + \beta^{e3e} P_2(\cos \theta_c)] . \quad (7.11)$$

To connect closely the (e,3-1e) reaction with the ($\gamma, 2e$) process we introduced in Eq. (7.11) $\alpha^{e3e} \equiv B_1^s$, $\beta^{e3e} \equiv B_2^s$. From Eq. (7.7) it is clear that, under the assumption $B_\ell^s = 0$, $\forall \ell > 2$, only three measurements are necessary to determine the parameters α^{e3e} , β^{e3e} and $d^4\sigma/d\Omega_a dE_c dE_a$. These quantities on their part parametrize completely the whole angular distribution $\sigma_{\mathbf{K},c}(\Omega_c)$. Appropriate geometries to conduct the measurements are: When the secondary electron c is detected under a direction perpendicular to \mathbf{K} ($\sigma_\perp := \sigma_{\mathbf{K},c}(\cos \theta = 0)$), parallel to \mathbf{K} ($\sigma_{\uparrow\uparrow} := \sigma_{\mathbf{K},c}(\cos \theta = 1)$) and antiparallel to \mathbf{K} ($\sigma_{\uparrow\downarrow} := \sigma_{\mathbf{K},c}(\cos \theta = -1)$). From algebraic relations we deduce then for the asymmetry parameters

$$\beta^{e3e} = \frac{2 - 2x}{1 + 2x} , \quad (7.12)$$

$$\alpha^{e3e} = \frac{3}{2} \frac{\sigma_{\uparrow\uparrow} - \sigma_{\uparrow\downarrow}}{\sigma_{\uparrow\uparrow} + \sigma_{\uparrow\downarrow} + 2\sigma_\perp} , \quad (7.13)$$

$$\frac{d^4\sigma}{d\Omega_a dE_c dE_a} = \frac{4\pi}{3} \sigma_{\uparrow\uparrow} + \sigma_{\uparrow\downarrow} + 2\sigma_\perp , \quad (7.14)$$

where $x := 2\sigma_\perp/(\sigma_{\uparrow\uparrow} + \sigma_{\uparrow\downarrow})$. We note that Eqs. (7.12)–(7.14) are also applicable to ($\gamma, 2e$) processes. From Eq. (7.13) it is obvious that α^{e3e} stands for the “memory” of the ejected electron to the incident direction and thus vanishes identically for a ($\gamma, 2e$) reaction ($\sigma_{\uparrow\downarrow} \equiv \sigma_{\uparrow\uparrow}$). Eq. (7.12) indicates that the asymmetry parameter β^{e3e} varies within the interval $\beta^{e3e} \in [-1, 2]$. When the secondary electron is predominantly ejected along \mathbf{K} ($x \rightarrow 0$) we obtain $\beta^{e3e} = 2$ (double ionization by single-binary collision of the projectile with electron b and a shake-off of electron c). If electron c is shaken off from an S -state its angular distribution is isotropic and hence $\beta^{e3e} = 0$, which is readily deduced from Eq. (7.12). In both cases ($\beta^{e3e} = 2, \beta^{e3e} = 0$) emitted secondary electrons are weakly correlated. In contrast, if $x \gg 1$ (i.e. for $\sigma_\perp \gg [\sigma_{\uparrow\downarrow} + \sigma_{\uparrow\uparrow}]$), electron b is ejected mainly perpendicular to \mathbf{K} indicating strong correlation between secondary electrons and leading to $\beta^{e3e} = -1$ [cf. Eq. (7.12)].

The usefulness of the asymmetry parameters introduced above is demonstrated by Fig. 7.5(a) and Fig. 7.5(b): On the one hand Fig. 7.5(a) indicates significant differences between the ($\gamma, 2e$) and (e,3-1e) cross sections, i.e. the optical limit is not fully approached. On the other hand Fig. 7.5(b) offers a detailed information on what is preventing the optical limit from being approached: According to Fig. 7.5(b) the major difference between ($\gamma, 2e$) and (e,3-1e) in the present case is the existence of the direction $\hat{\mathbf{K}}$ associate with the polar momentum-transfer vector. This is signified by a non-vanishing value of B_1 (or α^{e3e}) (cf. Eq. (7.13)). The similarities of the other asymmetry parameters mean that apart from this difference, the magnitude of the cross sections and the strength of electronic correlations (described respectively by B_0 and B_2) are similar both for ($\gamma, 2e$) and (e,3-1e) reactions.

Concluding this part we stress that the asymmetry parameters sketched above offer an excellent tool to illuminate the various respects of the relation between photon and electron-impact double ionization.

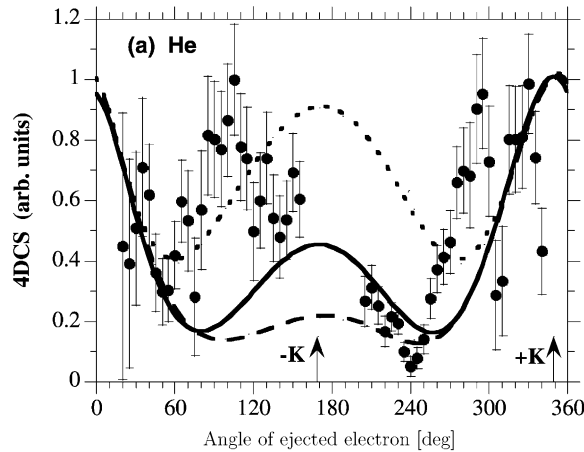


Fig. 7.6. The $(e, 3-1e)$ cross sections measured in the ab mode, i.e. the slow electron c is not detected. The scattering angle is $\theta_a = +15^\circ$, $E_a = 500$ eV and $E_b = 51$ eV (which implies that $E_c = 10$ eV). The target is a helium atom in the ground state and $E_0 = 640$ eV. The experimental 4DCSs are compared with the predictions of the 3C model (within the FBA) (full curve) and with the results of the C4FS theory (dotted) and its orthogonalized version (dashed curves). The \mathbf{K} direction is indicated.

7.5. Double ionization at low energies

As we have seen above, within the range of validity of the FBA, an appropriate parameterization of the cross section leads to a precise quantification of the individual contributions of the multipoles. However, such a procedure and in fact the FBA as such break down at lower energies and new methods are required to deal with the low-energy physics. Experimentally, the low energy regime has recently been explored [10] in the ab -mode using a He target. The incident energy is 600 eV. The data are shown in Fig. 7.6 in comparison with the results of some of the first-order (FBA) theories we discussed above. The most remarkable observation is that the calculated angular distributions show the well-known binary and recoil lobe structures, characterized by their symmetry about the momentum transfer direction $\pm\mathbf{K}$ as expected from first-order models. In the measured distributions two lobes are also present, however with two differences: (i) the symmetry about $\pm\mathbf{K}$ is broken, and (ii) one observes a large shift in the angular position of the lobes ($\sim 40\text{--}60^\circ$). The effect of this shift is to rotate the experimental recoil lobe forward, while the binary lobe is rotated backward, i.e. towards the incident (or the scattered) electron direction and away from it, respectively. This means that such shift cannot be attributed to a final state electron–electron repulsion between the scattered and the fast ejected electrons, which would rotate both lobes backward. Also, from the large disparity in the energies of these two electrons, 500 and 51 eV, one would not expect such a large angular deviation. Moreover, it is reasonable to assume that the slow, unobserved electron with energy 10 eV is emitted quasi-isotropically. Hence, the effect of a possible final-state interaction between the two ejected electrons on the 4DCS distribution of the fast ejected electron should be very small on average. Therefore, the observed shifts in Fig. 7.6 must be due to a dynamical effect which implies the participation of the unobserved slow ejected electron and/or of the residual doubly charged ion. Moreover, the symmetry break clearly indicates that this effect is a non-first-order effect

in the projectile–target interaction (not included in the FBA calculations shown in Fig. 7.6). In terms of the double-ionization mechanisms, the shake-off and the TS1 mechanisms are first-order processes that involve one single interaction of the projectile with the target, hence they are expected to yield distributions with the typical axial symmetry with respect to \mathbf{K} . Whereas the TS2 mechanism involves two successive projectile–target interactions, resulting in a breaking of the symmetry about $\pm\mathbf{K}$. It can thus be concluded from these observations that at the impact energy of 600 eV, the processes beyond the first order such as the TS2 play a crucial role in the dynamics of the double ionization.

8. Conclusions and future directions

In this article we gave an overview on the particle-impact double ionization of atoms as utilized to study the dynamics of four interacting charged particles in the continuum. The foundations of the theories that are currently applied to describe this process have been outlined and their results have been analysed and compared with experiments. The experimental techniques have been sketched and the merits of available approaches have been exposed and compared. A detailed analysis of the theoretical and the experimental results have been employed to uncover the four-body scattering dynamics. Furthermore, the significance of the various integrated cross sections has been addressed. It has been demonstrated that in the regime of small perturbations the pathways of double ionization are fairly well understood and documented by various experiments and theories. In contrast, the regime of low energies and/or for large perturbations is still to be explored. Currently, a number of experimental and theoretical groups are aiming at the study of the double ionization with low-velocity, charged projectiles where the treatment of the “true” four-body correlated system becomes unavoidable.

On the other hand the recent experimental developments on double ionization with highly charged ions revealed a behavior of the cross sections which is at variance with the predictions of a first-order perturbation treatment, and call thus for further theoretical efforts to understand the four-body scattering mechanisms in the non-perturbative regime. Future investigations include the double ionization dynamics with (spin and/or orbital) polarized collision partners, as well as the study of the four-body Coulomb continuum problem in the presence of external fields, such as the double ionization in a strong laser field.

Acknowledgements

We are grateful to many colleagues and friends for numerous discussions, collaborations and suggestions concerning the topic of this article. In particular we would like to mention L. Avaldi, I. Bray, J.S. Briggs, H. Klar, R. Dörner, A. Dorn, A. Malcherek, R. Moshhammer, A. Kheifets, H. Schmidt-Böcking, and J. Ullrich.

One of us (JB) would like to thank the National Science Foundation for partial financial support though a grant for the Institute for Theoretical Atomic and Molecular Physics at Harvard University and the Smithsonian Astrophysical Observatory where parts of this work were completed.

References

- [1] I. Taouil, A. Lahmam-Bennani, A. Duguet, L. Avaldi, Phys. Rev. Lett. 81 (1998) 4600.
- [2] Lahmam-Bennani, A. Duguet, A.M. Grisogono, M. Lecas, J. Phys. B 25 (1992) 2873.
- [3] Lahmam-Bennani, I. Taouil, A. Duguet, M. Lecas, L. Avaldi, J. Berakdar, Phys. Rev. A 59 (1999) 3548.
- [4] A. Lahmam-Bennani, A. Duguet, in: W.R. MacGillivray et al. (Eds.), Proceedings of the 17th International Conference on Phys. of Electron. Atom. Collisions (Brisbane), Adam Hilger, Bristol, 1992, p. 209.
- [5] B. El Marji, C. Schröter, A. Duguet, A. Lahmam-Bennani, M. Lecas, L. Spielberger, J. Phys. B 30 (1997) 3677.
- [6] C. Schröter, B. El Marji, A. Lahmam-Bennani, A. Duguet, M. Lecas, L. Spielberger, J. Phys. B 31 (1998) 131.
- [7] A. Lahmam-Bennani, C.C. Jia, A. Duguet, L. Avaldi, J. Phys. B 35 (2002) L215.
- [8] A. Lahmam-Bennani, A. Duguet, M.N. Gaboriaud, I. Taouil, M. Lecas, A. Kheifets, J. Berakdar, C. Dal Cappello, J. Phys. B 34 (2001) 3073.
- [9] A. Lahmam-Bennani, A. Duguet, L. Avaldi, M. Lecas, C. Dal Cappello, J. Phys. B 35 (2002) 1103.
- [10] A. Lahmam-Bennani, A. Duguet, S. Roussin, J. Phys. B 35 (2002) L59;
A. Lahmam-Bennani, A. Duguet, Correlations, polarization, and ionization in atomic systems, in: D.H. Madison, M. Schulz (Eds.), Proceedings of the International Symposium on (e,2e), Double Photoionized and Related Topics, Rolla, MO, AIP Conference Proceedings, AIP, New York, 2002, p. 96.
- [11] B. El-Marji, J.P. Doering, J.H. Moore, M.A. Coplan, Phys. Rev. Lett. 83 (1999) 1574.
- [12] R.W. van Boeyen, J.P. Doering, J.H. Moore, M.A. Coplan, J.W. Cooper, J. Phys. B 35 (2002) L97.
- [13] J.H. Moore, M.A. Coplan, J.W. Cooper, J.P. Doering, B. El Marji, AIP Conf. Proc. 475 (1999) 96.
- [14] M.J. Ford, B. El-Marji, J.P. Doering, J.H. Moore, M.A. Coplan, J.W. Cooper, Phys. Rev. A 57 (1998) 325.
- [15] M.J. Ford, J.H. Moore, M.A. Coplan, J.W. Cooper, J.P. Doering, Phys. Rev. Lett. 77 (1996) 2650.
- [16] M.J. Ford, J.P. Doering, J.H. Moore, M.A. Coplan, Rev. Sci. Instrum. 66 (1995) 3137.
- [17] Robert S. Freund, Robert C. Wetzel, Randy J. Shul, Todd R. Hayes, Phys. Rev. A 41 (1990) 3575.
- [18] A. Dorn, R. Moshhammer, C. Schröter, T.J.M. Zouros, W. Schmitt, H. Kollmus, R. Mann, J. Ullrich, Phys. Rev. Lett. 82 (1999) 2496.
- [19] A. Dorn, A. Kheifets, C.D. Schröter, B. Najjari, C. Höhr, R. Moshhammer, J. Ullrich, Phys. Rev. A 65 (2002) 032709.
- [20] A. Dorn, A. Kheifets, C.D. Schröter, B. Najjari, C. Höhr, R. Moshhammer, Phys. Rev. Lett. 86 (2001) 3755.
- [21] R. Wehlitz, M.-T. Huang, B.D. DePaola, J.C. Levin, I.A. Sellin, T. Nagata, J.W. Cooper, Y. Azuma, Phys. Rev. Lett. 81 (1998) 1813.
- [22] L.H. Andersen, P. Hvelplund, H. Knudsen, S.P. Møller, J.O.P. Pedersen, S. Tang-Petersen, E. Uggerhøj, K. Elsener, E. Morenzoni, Phys. Rev. A 40 (1989) 7366.
- [23] M. Unverzagt, R. Moshhammer, W. Schmitt, R.E. Olson, P. Jardin, V. Mergel, J. Ullrich, H. Schmidt-Böcking, Phys. Rev. Lett. 76 (1996) 1043.
- [24] S. Keller, B. Bapat, R. Moshhammer, J. Ullrich, R.M. Dreizler, J. Phys. B 33 (2000) 1447.
- [25] B. Bapat, S. Keller, R. Moshhammer, R. Mann, J. Ullrich, J. Phys. B 33 (2000) 1437.
- [26] M. Schulz, R. Moshhammer, W. Schmitt, H. Kollmus, R. Mann, S. Hagmann, R.E. Olson, J. Ullrich, J. Phys. B 32 (1999) L557.
- [27] R. Moshhammer, J. Ullrich, H. Kollmus, W. Schmitt, M. Unverzagt, O. Jagutzki, V. Mergel, H. Schmidt-Böcking, R. Mann, C.J. Woods, R.E. Olson, Phys. Rev. Lett. 77 (1996) 1242.
- [28] J. Moxom, D.M. Schrader, G. Laricchia, Jun Xu, L.D. Hulett, Phys. Rev. A 60 (1999) 2940.
- [29] C.J. Wood, R.E. Olson, Phys. Rev. A 59 (1999) 1317.
- [30] T. Kirchner, L. Gulys, R. Moshhammer, M. Schulz, J. Ullrich, Phys. Rev. A 65 (2002) 042727.
- [31] F. Melchert, E. Salzborn, D.B. Uskov, L.P. Presnyakov, Catalina Gonzalez, J.H. McGuire, Phys. Rev. A 59 (1999) 4379.
- [32] M.R. Fiori, Ginette Jalbert, C.E. Bielschowsky, W. Cravero, Phys. Rev. A 64 (2001) 012705.
- [33] R. Dörner, et al., AIP Conf. Proc. 443 (1998) 334.
- [34] C. Dal Cappello, H. Le Rouzo, Phys. Rev. A 43 (1991) 1395.
- [35] J. Berakdar, H. Klar, J. Phys. B 26 (1993) 4219.
- [36] A. Kheifets, I. Bray, A. Lahmam-Bennani, A. Duguet, I. Taouil, J. Phys. B 32 (1999) 5047.
- [37] J. Berakdar, Phys. Rev. A 63 (2001) 012706.

- [38] B. Nath, R. Biswas, C. Sinha, *Phys. Rev. A* 59 (1999) 455.
- [39] M.S. Pindzola, D. Mitnik, F. Robicheaux, *Phys. Rev. A* 59 (1999) 4390.
- [40] C. Dal Cappello, R. El Mkhater, P.A. Hervieux, *Phys. Rev. A* 57 (1998) R693;
C. Dal Cappello, H. Hda, A.C. Roy, *Phys. Rev. A* 51 (1995) 3735.
- [41] Seema Gupta, M.K. Srivastava, *Phys. Rev. A* 52 (1995) 2083.
- [42] Yu.V. Popov, C. Dal Cappello, B. Joulakian, I.V. Farnakeev, *JETP* 80 (1995) 179.
- [43] B. Joulakian, C. Dal Cappello, *Phys. Rev. A* 47 (1993) 3788.
- [44] D. Belkic, I. Mancev, V. Mergel, *Phys. Rev. A* 55 (1997) 378.
- [45] R. El Mkhater, C. Dal Cappello, *J. Phys. B* 31 (1998) 301.
- [46] A.W. Malcherek, J.S. Briggs, *J. Phys. B* 30 (1997) 4419;
A.W. Malcherek, J.-M. Rost, J.S. Briggs, *Phys. Rev. A* 55 (1997) R3979.
- [47] T. Ishihara, J.H. McGuire, *Phys. Rev. A* 38 (1988) 3310;
J.H. McGuire, et al., *Phys. Rev. Lett.* 62 (1989) 2933.
- [48] L.H. Thomas, *Proc. Roy. Soc. A* 114 (1927) 561.
- [49] K. Dettmann, G. Leibfried, *Z. Phys. D* 218 (1969) 1.
- [50] R. Shakeshaft, J.M. Wadehra, *Phys. Rev. A* 22 (1980) 968.
- [51] R. Shakeshaft, L. Spruch, *Phys. Rev. Lett.* 41 (1978) 1037.
- [52] E. Hordsal-Pedersen, L.C. Cocke, M. Stöckli, *Phys. Rev. Lett.* 50 (1983) 1910.
- [53] R. Shakeshaft, L. Spruch, *J. Phys. B* 11 (1978) L457.
- [54] J.S. Briggs, *J. Phys. B* 19 (1986) 703.
- [55] J.S. Briggs, *Comments At. Mol. Phys.* 23 (1989) 155.
- [56] M. Brauner, J.S. Briggs, *J. Phys. B* 24 (1991) 2227.
- [57] J. Berakdar, H. Klar, *J. Phys. B* 26 (1993) 3891.
- [58] V. Mergel, R. Dörner, M. Achler, Kh. Khayyat, S. Lencinas, J. Euler, O. Jagutzki, S. Nuttgens, M. Unverzagt, L. Spielberger, W. Wu, R. Ali, J. Ullrich, H. Cederquists, A. Salin, C.J. Wood, R.E. Olson, D. Belkic, C.L. Cocke, H. Schmidt-Böcking, *Phys. Rev. Lett.* 79 (1997) 387.
- [59] J. Palinkas, et al., *Phys. Rev. Lett.* 62 (1989) 2464.
- [60] E. Hordsal, B. Jensen, K.O. Nielsen, *Phys. Rev. Lett.* 57 (1986) 1414.
- [61] J.C. Joachain, *The Quantum Collision Theory*, North-Holland Publishing Company, Amsterdam, 1983.
- [62] T.A. Carlson, M.O. Krause, *Phys. Rev. A* 140 (1965) 1057.
- [63] R.J. Tweed, *Z. Phys. D* 23 (1992) 309.
- [64] J.H. McGuire, *Phys. Rev. Lett.* 49 (1982) 1153.
- [65] H. Ehrhardt, K. Jung, G. Knoth, P. Schlemmer, *Z. Phys. D* 1 (1986) 3.
- [66] M. Inokuti, *Rev. Mod. Phys.* 43 (1971) 297.
- [67] J. Berakdar, *J. de Physique IV C6* 3 (1993) 135.
- [68] L. Rosenberg, *Phys. Rev. D* 8 (1973) 1833.
- [69] M. Abramowitz, I.A. Stegun (Eds.), *Pocketbook of Mathematical Functions*, Verlag Harri Deutsch, Frankfurt a.M., 1984.
- [70] A.L. Fetter, J.D. Walecka, *Quantum Theory of Many-Particle Systems*, McGraw-Hill, New York, 1971.
- [71] M. Brauner, J.S. Briggs, H. Klar, *J. Phys. B* 22 (1989) 2265.
- [72] J.S. Briggs, *Phys. Rev. A* 41 (1990) 539.
- [73] H. Klar, *Z. Phys. D* 16 (1990) 231.
- [74] E.O. Alt, A.M. Mukhamedzhanov, *Phys. Rev. A* 47 (1993) 2004;
E.O. Alt, M. Lieber, *ibid* 54 (1996) 3078.
- [75] J. Berakdar, J.S. Briggs, *Phys. Rev. Lett.* 72 (1994) 3799.
- [76] J. Berakdar, J.S. Briggs, *J. Phys. B* 27 (1994) 4271.
- [77] J. Berakdar, *Phys. Rev. A* 53 (1996) 2314.
- [78] Sh.D. Kunikeev, V.S. Senashenko, *Zh. E'ksp. Teo. Fiz.* 109 (1996) 1561; [*Sov. Phys. JETP* 82 (1996) 839];
Nucl. Instrum. Methods B 154 (1999) 252.
- [79] D.S. Crothers, *J. Phys. B* 24 (1991) L39.
- [80] G. Gasaneo, F.D. Colavecchia, C.R. Garibotti, J.E. Miraglia, P. Macri, *Phys. Rev. A* 55 (1997) 2809;
G. Gasaneo, F.D. Colavecchia, C.R. Garibotti, *Nucl. Instrum. Methods B* 154 (1999) 32.

- [81] J. Berakdar, *Phys. Lett. A* 220 (1996) 237; *ibid* 277 (2000) 35; *Phys. Rev. A* 55 (1997) 1994.
- [82] J.E. Miraglia, M.G. Bustamante, P.A. Macri, *Phys. Rev. A* 60 (1999) 4532.
- [83] J. Berakdar, Recent advances in the theory of finite correlated systems: from few-body scatterings to phase transitions in the series *Recent Research Development in Physics*, Vol. 2, Transworld Research Network, Trivandrum, 2002, ISBN 81-7895-024-3.
- [84] F.W. Byron Jr., C.J., Joachain, B. Piraux, *Phys. Rev. Lett.* 9 (1983) 427.
- [85] J. Berakdar, *Phys. Rev. A* 55 (1997) 1994.
- [86] J. Berakdar, *Phys. Rev. Lett.* 85 (2000) 4036.
- [87] L.D. Faddeev, *Soviet Phys. JETP* 12 (1961) 1014.
- [88] L.D. Faddeev, *Mathematical Aspects of the Three-Body Problem*, Davey, New York, 1965.
- [89] M.J. van der Wiel, G. Wiebes, *Physica* 53 (1971) 225.
- [90] R. Hippler, K. Saeed, A.J. Duncanand, H. Kleinpoppen, *Phys. Rev. A* 30 (1984) 3328.
- [91] M.A. Chaundry, A.J. Duncan, R. Hippler, H. Kleinpoppen, *Phys. Rev. A* 39 (1989) 530.
- [92] E.C. Sewell, A. Crowe, *J. Phys. B* 15 (1982) L357.
- [93] E.C. Sewell, A. Crowe, *J. Phys. B* 17 (1984) 2913.
- [94] A. Lahmam-Bennani, G. Stefani, A. Duguet, in: F.A. Gianturco, G. Stefani (Eds.), *Lectures Notes in Chemistry* vol. 35: *Wavefunctions and Mechanisms from Electron Scattering Processes*, Springer, Berlin, 1984, p. 191.
- [95] W. Sandner, M. Völkel, *J. Phys. B* 17 (1984) L597.
- [96] G. Stefani, L. Avaldi, A. Lahmam-Bennani, A. Duguet, *J. Phys. B* 19 (1986) 3787.
- [97] J.P. Doering, R.S. Berry, J.H. Moore, M.A. Coplan, 16th International Conference on Physics of Electronic and Atomic Collisions, New York, 1989, p. 230.
- [98] J.P. Doering, M.A. Coplan, J.W. Cooper, J.H. Moore, *Proceedings of the (e,2e) Workshop*, University of Maryland, USA, 1989 (unpublished).
- [99] L. Avaldi, P. Belotti, P. Bolognesi, R. Camilloni, G. Stefani, *Phys. Rev. Lett.* 75 (1995) 1915.
- [100] A. Duguet, M. Cherid, A. Lahmam-Bennani, A. Franz, H. Klar, *J. Phys. B* 20 (1987) 6145.
- [101] J.S. Briggs, V. Schmidt, *J. Phys. B* 33 (2000) R1.
- [102] A. Lahmam-Bennani, C. Dupré, A. Duguet, *Phys. Rev. Lett.* 63 (1989) 1582.
- [103] B. El Marji, A. Lahmam-Bennani, A. Duguet, T.J. Reddish, *J. Phys. B* 29 (1996) L157.
- [104] Y.K. Kim, *Radiat. Res.* 61 (1975) 21.
- [105] Y.K. Kim, *Phys. Rev. A* 28 (1983) 656.
- [106] R.A. Bonham, M. Fink, *High Energy Electron Scattering*, Van Nostrand Reinhold Comp., New York, 1974, p. 80.
- [108] Yu.F. Smirnov, V.G. Neudatchin, *Sov. Phys. JETP Lett.* 3 (1966) 192.
- [109] V.G. Neudatchin, G.A. Novoskol'tseva, Yu.F. Smirnov, *Sov. Phys. JETP* 28 (1969) 540.
- [110] V.G. Neudatchin, Yu.F. Smirnov, A.V. Pavlitchenkov, V.G. Levin, *Phys. Lett. A* 64 (1977) 31.
- [111] Yu.F. Smirnov, A.V. Pavlitchenkov, V.G. Levin, V.G. Neudatchin, *J. Phys. B* 11 (1978) 3587.
- [112] V.G. Levin, V.G. Neudatchin, A.V. Pavlitchenkov, Yu.F. Smirnov, *J. Phys. B* 17 (1984) 1525.
- [113] N.P. Yudin, A.V. Pavlitchenkov, V.G. Neudatchin, *Z. Phys. At. Nucl. A* 320 (1985) 565.
- [114] V.G. Neudatchin, Yu.V. Popov, Yu.F. Smirnov, *Physics-Uspekhi* 42 (1999) 1017.
- [115] H. Le Rouzo, C. Dal Cappello, *Phys. Rev. A* 43 (1991) 318.
- [116] A. Duguet, A. Lahmam-Bennani, M. Lecas, B. El Marji, *Rev. Sci. Instrum.* 69 (1998) 3524.
- [117] E. Weigold, S.T. Hood, I.E. McCarthy, *Phys. Rev. A* 11 (1975) 566.
- [118] A. Lahmam-Bennani, H.F. Wellenstein, A. Duguet, M. Lecas, *Rev. Sci. Instrum.* 56 (1985) 43.
- [119] M.A. Coplan, J.H. Moore, J.P. Doering, *Rev. Mod. Phys.* 66 (1994) 985.
- [120] A. Lahmam-Bennani, *J. Phys. B* 24 (1991) 2401.
- [121] R. Moshhammer, et al., *Nucl. Instrum. Meth. Phys. B* 108 (1996) 425;
H. Kollmus, et al., *Nucl. Instrum. Meth. Phys. B* 124 (1997) 377.
- [122] C. Dupré, A. Lahmam-Bennani, A. Duguet, *Meas. Sci. Technol.* 2 (1991) 327.
- [123] K. Codling, L.J. Frasinski, *J. Phys. B* 26 (1993) 783.
- [124] F. Biggs, L.B. Mendelsohnand, J.B. Mann, *At. Data Nucl. Data Tables* 16 (1975) 202.
- [125] I. Bray, D.V. Fursa, *Phys. Rev. A* 57 (1996) 2991.
- [126] F. Maulbetsch, J.S. Briggs, *J. Phys. B* 26 (1993) 1679.
- [127] A. Huetz, P. Selles, D. Waymel, J. Mazeau, *J. Phys. B* 24 (1991) 1917.

- [128] Z. Teng, R. Shakeshaft, *Phys. Rev. A* 47 (1993) R3487.
- [129] A. Duguet, C. Dupré, A. Lahmam-Bennani, *J. Phys. B* 24 (1991) 675.
- [130] B. El Marji, A. Duguet, A. Lahmam-Bennani, M. Lecas, H.F. Wellenstein, *J. Phys. B* 28 (1995) L733.
- [131] T.A. Carlson, *Phys. Rev.* 156 (1967) 142.
- [132] A. Lahmam-Bennani, H. Ehrhardt, C. Dupré, A. Duguet, *J. Phys. B* 24 (1991) 3645.
- [133] A. Duguet, A. Lahmam-Bennani, *Z. Phys. D* 23 (1992) 383.
- [134] J. Berakdar, *Phys. Rev. A* 53 (1996) 2281.
- [135] U. Becker, R. Wehlitz, O. Hemmers, B. Langer, A. Menzel, *Phys. Rev. Lett.* 63 (1989) 1054.
- [136] R. Wehlitz, F. Heiser, O. Hemmers, B. Langer, A. Menzel, U. Becker, *Phys. Rev. Lett.* 67 (1991) 3764.
- [137] M.K. Srivastava, S. Gupta, C. Dal Cappello, *Phys. Rev. A* 53 (1997) 4104.
- [138] Yu.V. Popov, C. Dal Cappello, K. Kouzakov, *J. Phys. B* 29 (1996) 5901.
- [139] A.N. Perumal, R.M. Moshhammer, M. Schulz, J. Ullrich, *J. Phys. B* 35 (2002) 2133.
- [140] R.J. Tweed, *J. Phys. B* 6 (1973) 270.
- [141] M. Schulz, *J. Phys. B* 6 (1973) 2580.
- [142] M. Rudge, *Rev. Mod. Phys.* 40 (1968) 564.
- [143] C.T. Whelan, H.R.J. Walters, J. Hanssen, R.M. Dreizler, *Z. Phys. D* 14 (1989) 85.
- [144] O. Schwartzkopf, B. Krassig, J. Elmiger, V.L. Schmidt, *Phys. Rev. Lett.* 70 (1993) 3008.
- [145] A.S. Kheifets, I. Bray, *Phys. Rev. Lett.* 81 (1998) 4588.
- [146] C. Dal Cappello, B. Joulakian, in: C.T. Whelan (Ed.), *Proceedings of the NATO Advanced Research Workshop on (e,2e) and Related Processes*, Cambridge, 1992, Kluwer, Dordrecht, 1993.
- [147] C. Dal Cappello, B. Joulakian, J. Langlois, *J. Phys.* 3 (1993) 125.
- [148] H. Hda, C. Dal Cappello, J. Langlois, *Z. Phys. D* 29 (1994) 25.
- [150] C.C. Jia, A. Lahmam-Bennani, A. Duguet, L. Avaldi, M. Lecas, C. Dal Cappello, *J. Phys. B* 35 (2002) 1103.
- [151] C. Dal Cappello, J. Langlois, M.C. Dal Cappello, B. Joulakian, A. Lahmam-Bennani, A. Duguet, R. Tweed, *Z. Phys. D* 23 (1992) 389.
- [152] M. Grin, C. Dal Cappello, R. El Mkhater, J. Rasch, *J. Phys. B* 33 (2000) 131.
- [154] P.J. Marchalant, J. Rasch, C.T. Whelan, D.H. Madison, H.R.J. Walters, *J. Phys. B* 32 (1999) 705.
- [155] R. Hall, G. Dawber, A.G. Mc Conkey, M.A. MacDonald, G.C. King, *Z. Phys. D* 23 (1992) 377.